Numerical modeling of post current-zero dielectric breakdown in a low voltage circuit breaker

A DISSERTATION
SUBMITTED TO THE FACULTY OF THE GRADUATE SCHOOL
OF THE UNIVERSITY OF MINNESOTA
BY

Venkat raman Thenkarai Narayanan

IN PARTIAL FULFILLMENT OF THE REQUIREMENTS
FOR THE DEGREE OF
Doctor of Philosophy

Prof. Uwe Kortshagen

March, 2014

Acknowledgements

- Prof. Joachim Heberlein - My heartfelt gratitude for: your guidance, having my back during difficult phases and being a wonderful human being.
- Mrs. Yuko Heberlein - Without your help, my weekly meetings with Prof. Heberlein over the last two years would have been impossible. Sincere thanks to you.
- Prof. Kortshagen - I thank you immensely for guiding and advising me during Prof. Heberlein's absence.
- Profs. Girshick, Ernie, Simon and Pfender - Thanks very much indeed for being part of my thesis committee and for your valuable suggestions/discussions.
- EATON - This project work was funded by EATON's Global Research and Technology division in Pittsburgh, with Dr. Xin Zhou being the contract monitor.
- Dr. Xin Zhou and Dr. Christian Rümpler - Without your support and constructive feedback from EATON, this project wouldn't be where it is right now. Thanks a lot!
- Minnesota Supercomputing Institute (MSI) - I am extremely grateful for the computational resources allocated by MSI for this project.
- Osmo Vänskä and MN Orchestra - Your weekend concerts were the best medicines during painful and tough weeks. Bravo!
- David, Adam, Pingyan, Kheira, Romain and Vijay at ME 107 - Thank you guys for being such terrific office-mates and for the lively coffee sessions.

- Maddy, Praggy, Coma, Ranga, Savio, Meenakshi, Rohini and Durbha - Can't thank you all enough for tolerating me.
- HTPL, Howitzers cricket club, Bharat Diwali singers, ISSS discussion "Thurs3-5ers" group, ME/AEM biking gang, GSA-GSWU/UAW anti-union, UMN table-tennis club and Warriors cricket club - Being part of you and getting to know your members during my stay was sheer pleasure.
- My father and grandmother - Without your selfless sacrifices and emotional support over several years, my journey towards Ph.D. would have ground to a halt midway. As a small token of gratitude, I dedicate this thesis to you.

Dedication

To my Appa, my Paatti and the memory of Prof. Joachim Heberlein

Abstract

The gas mixture in the contact gap of a low-voltage circuit breaker post current-zero is characterized by a high degree of non-equilibrium. This partially-ionized mixture, which includes air, metal vapor and plastic vapor, is subjected to a transient recovery voltage post current-zero. This gas mixture, however, does not retain its dielectric capability instantaneously and as a consequence, is susceptible to dielectric breakdown post current-zero. Dielectric breakdown strength is characterized by a positive value of net ionization coefficient, which is the difference between ionization and attachment coefficients. A significant effort is directed in this work towards addressing effects of kinetic and chemical non-equilibrium on net ionization coefficient including the effects of a non-Maxwellian distribution of electron energies. The generalized distribution function is obtained from a Boltzmann equation solver. The effects of metallic and plastic vapors on dielectric breakdown strength at atmospheric pressure after current-zero for low-voltage circuit breaker applications have been investigated in this work. The effects of vibrationally-excited diatomic species and electronically-excited monatomic species on breakdown strength are also presented. The excited species are observed to lower the breakdown strength. The overall objective of this proposed research is analyzing the important factors contributing to the dielectric breakdown in a low-voltage circuit breaker post current-zero, which is a complex electro-hydrodynamic problem. Working towards this objective, a simplified and generalized framework is developed to predict the possibility of dielectric breakdown in a realistic low-voltage circuit breaker. It is expected that the current approach will provide quantitative comparisons between different metallic and plastic vapor combinations observed in realistic circuit breakers. The numerical results have been observed to predict reasonably the possibility of breakdown with available experimental data, particularly for air and metal vapor mixtures. This approach is the first step towards addressing realistic non-equilibrium conditions prevailing in an LVCB after current-zero and the results will be a valuable tool for suggesting improvements in dielectric interruption ability of LVCBs.

Contents

List of Tables

List of Figures

Chapter 1

Introduction

1.1 Background

Industrial installations and household appliances utilize electrical energy for their functioning. A stable operation of these devices requires effective protection against possible fault (or short-circuit) currents originating from the electrical current source. For this purpose, incorporating switching elements becomes imperative. The peak currents flowing through these devices range from a few amperes in a household appliance to several kilo-amperes in an industrial installation and the short-circuit currents have been observed to reach even an order of magnitude higher in both cases. These short circuit currents generate intense electro-mechanical stresses and heat fluxes which could result in considerable loss of life and property in the absence of appropriate circuit interrupters. The general term "circuit breakers" [1] is designated to switching elements which interrupt short-circuit currents and prevent damages to electrical devices. The chief function of a circuit breaker is to suitably connect (or disconnect) the electrical current flow to the load and this is achieved through engaging (or disengaging) electrical contacts present within them. After detecting a short-circuit current, the electrical contacts automatically separate resulting in a high current electrical arc discharge. The observed temperatures in the core of the generated electric arc are usually in the range of 20,000-30,000 K and in order to prevent significant erosion or melting of the circuit breaker components, a suitable mechanism is devised to instantaneously (upon separation of contacts) drive the arc away from the contacts region and eventually extinguish

the arc.

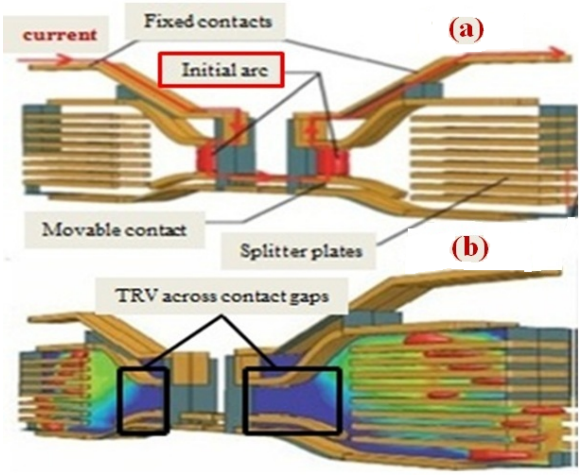

Figure 1.1: A sample low-voltage circuit breaker used in a CFD simulation [2].

In this research project, we focus our attention on alternating-current low voltage circuit breaker (LVCB) and will now briefly explain the mechanism of extinguishing the arc in a typical LVCB shown in figure 1.1. In the normal operating mode, the sinusoidal input current flows through the engaged contacts in the direction indicated using red arrows. Detection of a fault current, which could occur anytime within a cycle, results in separation of the movable contact from the fixed contact and creation of an electric arc. The current in the conducting parts of the breaker induces a magnetic field $\boldsymbol{B}$ (pointed outward to plane of the figure) perpendicular to the electric current density $\boldsymbol{j}$ in the arc, which in turn creates a convective cross-flow generated by a pressure gradient (∇p) equivalent to the electro-magnetic Lorentz force ($\boldsymbol{j} \times \boldsymbol{B}$). This cross-flow is necessary for moving the arc away from the contacts into the splitter plates. Furthermore, the larger arc is broken down into smaller arcs in the rack of steel splitter plates, within which the smaller arcs get elongated, cooled and extinguished owing to the ferromagnetic properties of iron. Most importantly, the arc extinction is aided by the AC current dropping to zero twice within a cycle. This state, when the arc has been completely extinguished and the AC current reaches zero, is commonly referred to in literature as current zero (CZ). It is worth mentioning here that in all the circuit breakers, there is a small time delay of a few nanoseconds (ns) between arc generation and cross flow

initiation. As a result, a substantial erosion of the metallic contacts, copper, iron and tungsten for example, has been observed under experimental conditions. Electronegative gases, air and SF_6 for example, are highly favored as the gaseous medium in a circuit breaker owing to their ability to form anions by quenching excess electrons from the highly ionized state. Even though the highly electronegative SF_6 gas could be employed as the medium for transporting the high current arc away from the contacts, atmospheric pressure air is preferable since SF_6 gas has an extremely high global-warming coefficient.

1.1.1 Thermal and dielectric breakdown

The contact gap after CZ is filled with a high temperature (on the order of 1,000 K) and weakly-ionized plasma, meaning that a residual electrical conductivity is present after CZ. In addition to the metallic contact erosion mentioned earlier, erosion of plastic side walls has also been reported in an LVCB. Owing to the inductance and capacitance of the circuit, which is characteristic of the circuit designed for a specific application, a rapidly rising transient recovery voltage (TRV) of several Volts per microsecond appears across the contacts a few microseconds (μs) after CZ. The time between the occurrence of CZ and appearance of TRV is known as the delay time and controlled experiments can

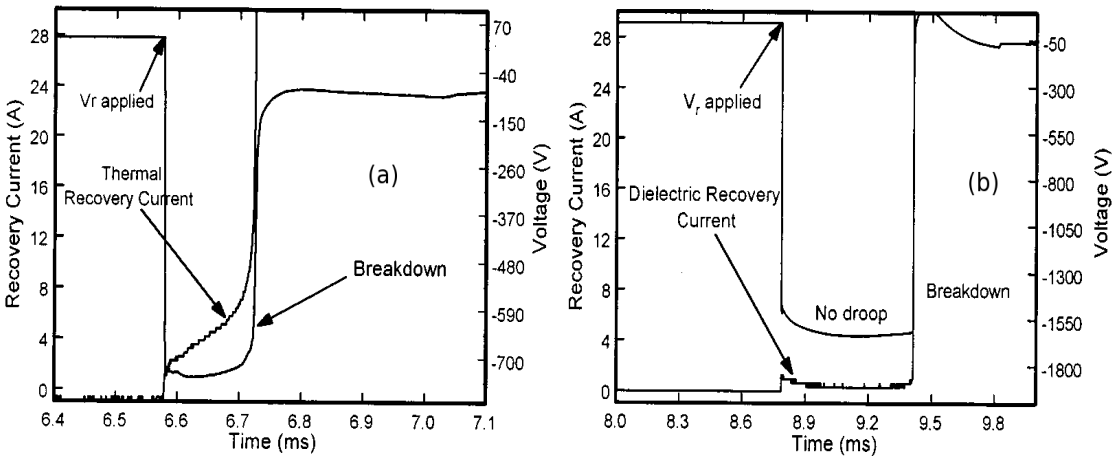

Figure 1.2: Characteristics of: (a) Thermal breakdown. (b) Dielectric breakdown. [3]

be performed for different stipulated delay times. Even though delay times of several μs have been considered in controlled experimental set-ups [3], the delay times are on the

order of ns in reality. This means that the TRV appears almost instantaneously post-CZ compared to other fluid dynamic time scales. In general, the greater the delay time the greater is the temperature drop of the plasma and the recovery of dielectric properties owing to the cooling during the delay time has been termed in the literature as "free recovery". In order to improve the interruption capability of the LVCB, the hot gaseous mixture needs to be cooled rapidly to eliminate residual currents which might grow rapidly and thereby retain its dielectric capabilities. In literature, the terms breakdown and arc re-ignition have occasionally been used interchangeably. Based on experimental investigations [3], the gaseous mixture could be subjected to two types of breakdown - (a) Thermal breakdown or (b) Dielectric breakdown. Although a strict distinction between these breakdowns is somewhat arbitrary, the characteristics of these two types shown in figure 1.2 are observed to be different. The thermal breakdown, in figure 1.2(a), has been characterized by an increase in gas temperature within the contact gap due to Joule heating effect of the recovery current flow. The increasing temperature further increases the electrical conductivity and hence, the recovery current increases steadily till the point of voltage collapse. The recovery voltage drops slowly before the voltage collapse. On the other hand, the dielectric breakdown shown in figure 1.2(b) is associated with a sudden collapse in the voltage across the gap associated with flow of negligible recovery current. The recovery voltage is not observed to droop and remains constant unlike for thermal breakdown. Also, the recovery times corresponding to dielectric breakdown are higher compared to those of thermal breakdown. In this research project, we focus our attention particularly towards dielectric breakdown of a hot gaseous mixture in the time zone between (i) a few μs before attainment of CZ and (ii) several milliseconds (ms) after attainment of CZ.

1.1.2 Streamer/spark breakdown

The quenching medium in a typical low-voltage circuit breaker is mostly air at around atmospheric pressure, which behaves like a good electrical insulator at low temperatures. When an electric field E is applied across a dielectric gap of length d containing air at pressure p, the gap begins to conduct a small electrical current whose magnitude depends on the operating parameters (E, p and d). An electrical breakdown of a dielectric gap can be defined as a transition from an insulating to a conducting state.

Electrical breakdown occurs when: (1) the applied voltage exceeds the static breakdown voltage (V_s) and (2) free electrons exist in the gap. Two mechanisms of electrical breakdown have been subject to extensive research (1) Townsend mechanism and (2) streamer mechanism. Llewellyn-Jones [4] quantified the importance of the parameter "*pd*", the product of pressure and gap distance, towards classifying the breakdown as either belonging to Townsend or Streamer type. Depending on whether "*pd*" is less or greater than 1000 Torr-cm, Townsend mechanism or streamer mechanism quantify the breakdown behavior accurately. Hence, for the high pressure (greater than atmospheric pressure) gas mixture observed in circuit breakers under our consideration, the breakdown behavior is expected to have characteristics closer to the streamer mechanism. The streamer breakdown is an electrode independent, highly transient and complicated nanosecond scale mechanism suitable for high pressure discharges. An electron emitted from the cathode is accelerated by the applied electric field and generates several electron-ion pairs in collisions with neutral molecules during its flight towards anode. These electrons multiply in number in subsequent collisions resulting in the formation of a primary electron avalanche which is a pre-requisite for any breakdown mechanism. Owing to their higher mobilities, the electrons in the avalanche travel significantly faster towards the anode while the positive ions remain more or less stationary. When the electron number density within the avalanche attains a significant amplification ($10^{12} cm^{-3}$), the generated space charge electric fields due to the charge separation can be of the order of the applied electric field leading to breakdown. Streamers are weakly ionized filaments or channels formed from the primary avalanche in a strong electric field and grow towards either or both the electrodes. There are two types of streamers observed in experiments. In the first case, called the cathode-directed or positive streamer, the streamer is initiated from the anode surface after the avalanche reaches the anode and it propagates towards the cathode. In the second case, called the anode-directed or negative streamer, the space charge fields in the primary avalanche, which has not even travelled far from the cathode, become so high that the avalanche gets transformed into a streamer and grows towards the anode. Although experimental verification at high temperatures has not yet been conclusive, it is currently hypothesized that the growth of streamers is due to secondary electron avalanches created through photo-ionization process, by photons emitted from excited atoms in the primary avalanche. The streamer

mechanism neglects the effects of secondary electrons created at the cathode, which is central to the Townsend mechanism.

1.2 Motivation

Dielectric breakdown or re-ignition has been observed to drastically reduce the performance and lifetime of an LVCB [5]. Based on our literature study, both experimental [6, 7] and numerical works [8, 9] on analyzing dielectric breakdown in high-voltage circuit breakers (HVCB) utilizing SF_6 have appeared earlier compared to breakdown studies of compressed air in LVCBs. This is primarily because the trend towards utilizing alternatives to SF_6 in an LVCB began in the last decade. Furthermore, in the recent years, there is an increasing trend towards miniaturization of residential circuit breakers. Apart from the complex geometry of the LVCB which requires complicated and time-consuming set-ups for detailed experimental investigations, set-ups aimed at reproducing or repeating the experimental results are not only difficult [3] but also expensive. The lack of repeatability of experimental results can also be attributed to the stochastic nature [10] of dielectric breakdown. Additionally, the time duration between the high-current arc initiation to the eventual dielectric breakdown is on the order of several ms, while that between arc extinction to breakdown is on the order of several μs. To summarize, dielectric breakdown is a multi-timescale process, which within complex LVCB geometries is difficult to be captured and the experimental results are difficult to be repeated. Hence, it becomes imperative to model numerically the underlying phenomena in a breakdown in order to improve the performance and lifetime of an LVCB.

Several numerical works have addressed the time period between contact separation and extinction [11, 12] in an LVCB. On the other hand, the numerical models which have proposed to predict breakdown in an LVCB [13] usually address thermal rather than dielectric breakdown. Much of the previous research published regarding dielectric recovery characteristics of air mixtures around CZ were found to: (i) be either purely experimental resulting in fitting simple empirical correlations for the obtained experimental data, or (ii) have significant simplifying assumptions like Local Thermodynamic Equilibrium (LTE), or (iii) neglected important effects pertaining to metallic or plastic

vapors, or (iv) a combination of the afore-mentioned factors. This research is motivated by the need to develop numerical models capable of describing dielectric breakdown, including realistic non-equilibrium effects and involving air, metal vapor and plastic vapor mixtures, within complex LVCB geometries.

1.3 Scope of the thesis

Dielectric breakdown post-CZ in realistic 3D circuit breaker geometries is a multi-time scale, non-equilibrium electro-hydrodynamic problem. The arc plasma fluid dynamics within complex geometries including electro-magnetic effects, in the time interval between arc formation to extinction, was analyzed by Rümpler [14] for air-metal vapor mixtures. The important assumptions in his work include: (i) "one-fluid" formulation in which air and metal vapor are considered to be individual components, (ii) LTE which implies chemical and kinetic equilibrium, (iii) Laminar flow, and (iv) negligible transient electro-magnetic effects. Rümpler's flow solver, which was recently extended to include plastic vapor effects, will be utilized in the current work to capture fluid flow beyond arc extinction to a few milliseconds (ms) post-CZ. His solver has been demonstrated to capture thermal breakdown but it is incapable of capturing dielectric breakdown owing to the LTE assumption. The current work squarely aims to address this drawback by relaxing the LTE assumption while obtaining requisite fluid-dynamic variable inputs from the flow solver. This thesis describes the development of a generalized framework for evaluating dielectric breakdown post-CZ within an LVCB, considering air-metal-plastic vapor mixtures and incorporating realistic non-equilibrium processes. This work also explains the implementation of this framework in simplified 2D geometries and it is expected that extensions to 3D geometries will be straight-forward, albeit computationally expensive.

One of the most important non-equilibrium effects considered in this work is the generalized non-Maxwellian electron-energy probability function (EEPF), observed experimentally post-CZ. This is primarily owing to the appearance of the TRV, resulting in significant deviations from a Maxwellian EEPF. We have ascertained that assuming

a Maxwellian rather than a non-Maxwellian EEPF for electron-impact collision processes, like excitation and ionization, would yield erroneous results for the highly non-equilibrium state observed post-CZ. An important consequence of a non-Maxwellian EEPF is kinetic non-equilibrium, in which the electron temperature (T_e) is different from the heavy-species temperature (T_h). Additionally, chemical non-equilibrium stemming from finite-rate chemical kinetics prevails post-CZ. Henceforth, an efficient and stable reaction kinetics solver (CHEMKIN [15], DVODE [16], CHEMEQ2 [17]) is required in which the reaction rates for electron-impact collision processes are obtained as inputs from a Boltzmann-equation solver (ELENDIF [18], BOLSIG+ [19]). Even though significant initial effort was dedicated towards integrating the solvers CHEMKIN and ELENDIF, it was determined from our subsequent investigations that the software ZDPlasKin [20] already provides the integrated capabilities of BOLSIG+ and DVODE. Moreover, we have also developed an in-house kinetics solver upon integrating CHEMEQ2 and BOLSIG+, programmed using FORTRAN-90. Finally, the kinetic effects of higher-energy excited species, which have been observed to play an important role in electron-impact ionization and attachment processes, have also been included in this work.

In the following paragraphs, a few other important effects, which are beyond the scope of current thesis but will be considered in future, are briefly addressed for the sake of completeness. Firstly, the flow solver has not been updated to consider kinetic non-equilibrium which would entail an additional energy conservation equation corresponding to the electrons. This is referred as non-LTE model in literature and has been observed to provide closer agreement with experimental results for thermal plasmas, compared to an LTE model [21]. For plasmas in kinetic non-equilibrium, thermodynamic and transport properties need to be calculated considering this temperature dissimilarity. Accurate transport properties for general two-temperature thermal plasmas have been calculated by Rat *et al.* [22]. Their calculation results for two-temperature argon plasmas assume chemical equilibrium [23]. The general framework developed in current work can be easily extended to calculate two-temperature properties in future. The additional complexity introduced by the current work is that of chemical non-equilibrium. Calculation of thermodynamic and transport properties considering chemical non-equilibrium with three simple reactions for oxygen plasma has

been demonstrated by Ghorui *et al.* [24], in which chemical non-equilibrium is characterized by a parameter "r". This parameter is defined as the ratio of a modified rate constant accounting for chemical non-equilibrium to the equilibrium rate constant and is expected to be in the range between 0.7 and 1.5 for the oxygen cutting torch under their investigation. However, as to date, the number of reactions in the current study for the simple case of air-metal vapor mixture is around 168 and hence, following a similar procedure would result in significant computational cost. Depending on the determined numerical complexity, the effects of chemical non-equilibrium on these properties would either need to be addressed or certain simplifying assumptions be made to reduce computational effort and cost. As to date, the equilibrium flow solver utilizes look-up tables and an interpolation mechanism to obtain properties corresponding to the following input parameters: (a) heavy particle temperature, (b) pressure and (c) mass-fractions of air, metal vapor and plastic vapor.

After the arc is extinguished and the weakly-ionized gas cools to near ambient temperatures, the metal and plastic vapor within the circuit breaker post-CZ are observed experimentally to nucleate, condense and agglomerate to form particulate matter. Because of high collisionality observed in atmospheric pressure gases, agglomeration results in particle sizes on the order of a few microns (μm). Particle formation and their eventual tracking with flow solver is computationally expensive and hence, will be assigned a lower priority in future work. It has also been observed that metal droplets formed in the time interval between arc formation and extinction cool down and attach themselves to the circuit breaker surfaces in the form of protrusions. The contribution of these protrusions towards dielectric breakdown in HVCBs utilizing SF_6 gas has been analyzed by Seeger's group [25]. Similar simplifications can be considered for gas mixtures in present work, leading to a refined and accurate breakdown field model in future. Since the contact material is assumed to be copper in this work, the simplest improvement that can be introduced at the electrode boundaries is a local "field-enhancement factor" (β) [26] corresponding to an idealized micro-protrusion (of several possible different shapes) on the electrode surface. In realistic circuit breakers, alloys of materials with different thermionic properties like Ag-W (silver-tungsten) and Ag-C (silver-graphite) in suitable proportions have been employed. The current work is capable of quantifying the dielectric performance of different metal vapors once electron impact processes data

for these different electrode materials are obtained.

Experimental work on circuit breakers post-CZ provide evidence on the existence of turbulent recirculation regions which are responsible for uneven cooling within the contact gap, thereby bolstering non-equilibrium effects [27]. Owing to the inherent modeling complexities of thermal plasma and extremely small time-scales to capture small-eddy effects requiring significant computational resources, performing direct numerical simulation (DNS) is simply out of the scope. Researchers have addressed turbulence effects in thermal plasma using either a k-ϵ model [28] or Large-eddy simulation (LES) [21]. Trelles developed an in-house code to address LES turbulence effects for thermal plasma in a spraying torch using a finite element method. Rümpler's flow solver, written designed using FLUENT [29], assumes a laminar flow and a possible improvement towards fluid-dynamic modeling would be to upgrade to a compressible LES model within FLUENT or to consider complete migration to the open-source software Open-FOAM [30]. This effort is of lower priority because of the inherent numerical complexities in transition to turbulent LES model.

The thesis is organized into the following chapters:

- Chapter 2 briefly covers the literature survey corresponding to the subjects presented in this thesis.

- In Chapter 3 the overall methodology or approach, including the assumptions, of this thesis is explained in detail. The theory and numerical procedures required to obtain properties of general gas mixtures are also described.

- Chapter 4 describes the dielectric, thermodynamic and transport properties of the dielectric fluid in an LVCB - compressed air.

- Chapter 5 presents the effects of metal vapor inclusion on the properties of compressed air.

- Chapter 6 addresses the impact of plastic vapor on specifically the dielectric properties of compressed air-metal vapor mixtures.

- Chapter 7 provides a comparison of dielectric breakdown prediction results based on current work with those from available experimental data, for air-copper mixtures alone.

- Chapter 8 summarizes the conclusions from current work and provides directions for future work.

- For the sake of clarity, elaborate information on calculation of transport and dielectric properties in Chapters 4-6 have been relocated to the Appendices. In particular, the Appendices provide additional details on the dielectric breakdown field calculations for air-metal-plastic vapor mixtures of interest in the current thesis.

Chapter 2

Literature review

In this chapter, we provide an overview on the literature study which helped formulate our approach to analyzing dielectric breakdown in LVCBs. Some of the earliest experimental and numerical works on dielectric breakdown post-CZ pertain to gas-blast HVCBs employing SF_6 gas. Hence, we first begin by summarizing the work on arc reignition in gas-blast HVCBs. In a gas-blast circuit breaker, a relatively colder quenching gas (SF_6) is accelerated through a nozzle and directed across the arc at high velocities near current-zero. However, the gas mixtures in the current work employ compressed air, which upon arc extinction get contaminated with metal and plastic vapors. Hence, studies analyzing dielectric breakdown in compressed: (i) air, (ii) air-metal vapor and (iii) air-metal-plastic vapor will be presented subsequently.

The first analytical theory concerning arc interruption, named "race theory", was formulated by Slepian [31]. The race theory can be considered the most simplified statement regarding dielectric breakdown and postulated that for a successful arc interruption, the rate of dielectric strength increase must be faster than the rate of recovery voltage increase. In other words, the dielectric strength of the cathode sheath formed after CZ needs to be greater than the critical breakdown field of the gaseous medium. When the rate of electron loss mechanisms, electron attachment and ion recombination for example, is greater than the rate of rise of TRV, a successful interruption results.

Qualitatively speaking, dielectric breakdown can be viewed on the basis of two competing processes (a) ionization (and detachment) and (b) attachment (and recombination). The multiplication of electrons due to creation of new electron-ion pairs is

quantified using the ionization coefficient (α), while the loss of electrons stemming from the formation of anions in an electronegative gas is quantified using the attachment coefficient (η). The difference between the ionization and attachment coefficients ($\alpha - \eta$) is termed the effective or net ionization coefficient ($\bar{\alpha}$), and breakdown is said to occur when $\bar{\alpha}$ has a positive value. Our approach towards analyzing dielectric breakdown in the proposed research work primarily involves: (a) quantifying the effective ionization coefficient and (b) determining the factors which lead to its positive value. In this research work, dielectric breakdown in a complex geometry is characterized by the formation of a conductive channel between the metallic contacts, across which the TRV appears. An important topic of interest with regard to dielectric breakdown of compressed gases is the streamer tracking in a quiescent gas. Depending upon whether a transition to streamer to leader is possible, the streamer is expected to result in a spark breakdown. Pertaining to channel formation in a circuit breaker, two important terms used in this chapter need to be defined: (a) Streamer, and (b) Leader. A streamer is defined as an ionization wave which develops in the quiescent gas, carries a large space-charge generated electric field at its leading edge and possesses a low electrical conductivity. A leader is a moderately conducting channel in a gas discharge, possessing an electric field much smaller than that of a streamer channel. Most importantly, leaders form when the channel temperature exceeds the gas dissociation temperature, meaning that a leader channel is hotter than the streamer channel.

2.1 Dielectric breakdown in HVCBs

The research work on dielectric breakdown in HVCBs post-CZ have focused mostly on the interruption capability of SF_6 gas. Pedersen [32] considered the possibility of SF_6 spark breakdown in non-uniform fields for simplified geometries, through both Townsend and streamer mechanisms. He derived the breakdown criterion for streamer mechanism, with the inclusion of electron attachment and photo-ionization effects. The high-energy photons required for photo-ionization were a by-product of radiative recombination of electrons and positive ions. Upon application of the streamer criterion to spherical electrodes with gap lengths (d) 0.5 and 1.0 cm in the pressure (p) range 1-4 atm, the calculated breakdown voltages were observed to be in excellent agreement with the

measured voltages for all possible combinations except $d = 1.0\ cm$ and $p = 4\ atm$. Additionally, Pedersen extended his streamer criterion to include the effects of surface roughness [33] and observed a large reduction in breakdown fields for SF_6 compared to those for a clean geometry. This implies that electrode roughness enhances dielectric breakdown.

Detailed experimental and theoretical investigations of dielectric recovery in a gas-blast circuit breaker were performed by Ragaller and his co-workers. Using their experimental set-up, Schade and Ragaller [6] obtained the temperature decay profile post-CZ upto the time of complete dielectric recovery within the gap. The dielectric recovery was measured in different geometries by applying several voltage profiles across the contact gap, at different time instants post-CZ. The measured dielectric recovery were observed to be dependent upon the voltage profile and the breaker geometry. The theoretical and experimental results revealed the dependence of the recovery curve on (i) the turbulence in the region close to the stagnation point, (ii) deviations from LTE and (iii) nozzle geometry. The effects of deviations from LTE towards dielectric breakdown will be addressed in this work.

More recently, Seeger and his colleagues extended their investigations on dielectric recovery in compressed air [34] to SF_6 gas. Firstly, using a theoretical model for the protrusion on an electrode surface, they explained in detail a stochastic mechanism of leader formation and the eventual leader to spark transition [25, 35] in a HVCB. Subsequently, using an estimated critical electric field strength (E_{crit}) for the streamer channel and their theoretical framework for spark breakdown [36], they compared and observed satisfactory agreement between the measured and predicted leader inception voltages. The most important parameters determining the gap breakdown were: (i) streamer length, (ii) streamer corona charge and (iii) channel temperature at leader inception. The streamer length and corona charge were observed to be directly proportional to the average temperature in the streamer region. Also, the channel temperatures necessary for streamer to leader transition for SF_6 were observed to be higher than its dissociation temperature. The primary and valid assumptions in the theoretical analysis are that E_{crit} is directly proportional to pressure and inversely proportional to the temperature. However, instead of calculating E_{crit} explicitly, Seeger *et al.* [36] propose a simple scaling law for E_{crit} with respect to the critical electric field strength at 300 K ($E_{cr,0}$).

Determining E_{crit} accurately for general gas discharges is one of the primary objectives of current work.

2.2 Dielectric breakdown in LVCBs

The dielectric breakdown mechanism for a strongly electro-negative SF_6 gas used in a HVCB is different from that for a weakly electro-negative air used in an LVCB. It will be observed later that the inclusion of a plastic vapor containing nitrogen atoms, PA-66 for example, increases the electro-negative nature of the overall gas mixture. In this section, we briefly describe previous research works on dielectric breakdown in LVCBs.

2.2.1 Critical processes in dielectric breakdown of compressed air

Irrespective of the breakdown mechanism, there are various important processes that result in dielectric breakdown of air which have been studied by researchers. Contribution of multi-species reaction mechanisms towards breakdown have been explored in earlier works. Several studies describe streamer propagation in compressed air by providing detailed kinetic mechanisms contributing to the propagation. The effects of vibrationally-excited and electronically-excited metastable species of nitrogen and oxygen on breakdown have been documented by several researchers [37, 38, 39, 40, 41]. Mnatsakanyan and Naidis [42] provide a literature review on charged particle formation processes including (a) direct ionization, (b) stepwise ionization, (c) associative ionization, (d) photo-ionization, (e) Penning ionization and loss processes including (a) electron-ion recombination, (b) production of negative ions in nitrogen-oxygen mixtures. Naidis [43] simulated the streamer-to-spark transition in non-uniform air gaps occurring in nanosecond timescales and mentioned that the "time delay" between the first streamer propagation and spark formation depends on the mean reduced electric field in the gap. Towards explaining this time delay, he emphasized the importance of a kinetic mechanism which is related to the accumulation of active particles (radicals and excited molecules) changing the balance between the rates of generation and loss of electrons due to detachment, recombination, stepwise and associative ionization. A comprehensive set of reaction rates for the afore-mentioned processes in high temperature N_2-O_2 plasmas has also been presented [44,45]. In this work, some of these important reactions

contributing to the dielectric breakdown have been included.

Owing to the "one-fluid" formulation of the CFD solver, tracking a streamer is unfeasible and hence, a simplified methodology is preferred to characterize dielectric breakdown. The most important parameter with regard to breakdown is the critical reduced electric field strength (E_{crit}/N), which is defined as the reduced field strength (E/N) for which the effective ionization coefficient ($\bar{\alpha}$) equals zero. Tanaka [46] analyzed the variation of E_{crit}/N with heavy- particle temperature, considering uniform electric field and a uniform hot gas between temperatures of 300-3500 K. The chief conclusion was that the critical electric field strength decreases with increasing heavy particle temperature between 1500-3500 K and that this decrease results mainly from NO molecule formation over 1500 K and O_2 dissociation over 3000 K. In several of the afore-mentioned research works, relevant parameters like the reaction rates for electron-impact collision processes were obtained using the numerical solution of Boltzmann equation for electron energy probability function (EEPF). However, calculation of the reaction rates assuming a Maxwellian EEPF or empirical correlations based on the reduced electric field (E/N) was also observed. A two-term Boltzmann equation solver is utilized in current work to obtain a generalized EEPF.

2.2.2 Processes characteristic to dielectric breakdown in an LVCB

Apart from the contributing processes in breakdown of atmospheric air, there are a few additional processes peculiar to a low voltage circuit breaker. Lindmayer and his co-workers [11] focused particularly on the numerical analysis of arc motion and splitting within the splitter plates for a simplified 3D geometry. Rong *et al.* [12] devised an experimental set-up for which good agreement was obtained with arc motion profiles compared to numerical solutions from a set of 3D magneto-hydrodynamic equations. However, studies focusing on post current zero dielectric recovery have been restricted to medium- and high-voltage circuit breakers. Seeger *et al.* [34] reported experimental investigations pertaining to dielectric recovery post-CZ using air instead of SF_6 as the fluid for a high-voltage circuit breaker geometry. They focused on the highest temperature region (extinct arc) and plotted the experimental results of breakdown voltage variation with time for different values of pressures. Employing a streamer breakdown criterion, they observed good agreement with numerical results for the effective reduced

ionization coefficient ($\bar{\alpha}$) from a Boltzmann equation EEPF solver. Shea [47, 48, 49] experimentally analyzed the effects of exhaust vent size, chamber wall material (plastic) and contact material (metal) on dielectric recovery for a realistic medium-voltage circuit breaker configuration along with different TRV delay times. The cooling of the plasma within the contact gap was observed to increase with increase in delay time. Based on his observations, Shea concluded that: (a) increasing the vent areas coupled with greater air flow rates and, (b) use of PA-66 (Nylon) compared with other plastic materials like POM, resulted in longer breakdown delays and hence better dielectric recoveries. Tanaka [50] extended his earlier calculations of critical reduced electric field strength in atmospheric pressure air by including metallic copper contamination. The chief conclusion drawn from his calculations was that the presence of even a small percentage of copper was detrimental to the dielectric recovery of the hot gas mixture, since copper vapor has a small ionization potential (7.7 eV) compared to other gaseous species. To our current knowledge, the CFD and kinetic analysis of Teulet *et al.* [13, 51] can be considered to be the first effort towards including low to moderately-high temperature ($< 6000\ K$) effects of copper and PA-66 vapors in a low-voltage circuit breaker. In their 1D model of a decaying arc, Teulet *et al.*concluded that the presence of PA-66 results in an increased rate of cooling of an extinguishing arc. They also mentioned that the accumulation of soot within the circuit breaker would induce leakage currents leading to a dielectric breakdown. However, citing a lack of molecular collision cross section data, they neglected the effects of larger hydrocarbon and condensed species and reported that their results might be erroneous owing to the presence of condensed species below 3000 K. Nonetheless, their analysis is highly simplified in the sense that rather than quantifying the dielectric breakdown, they associated the interruption capability with electrical conductivity values at different locations in the breaker geometry and attributed poorer interruption capability to regions with higher conductivity values (and vice-versa). As mentioned in the previous subsection, estimation of breakdown fields including plastic vapor is an important outcome from the current work. Even though, condensed species number densities are captured in the composition calculations, their contributions to EEPF and soot formation are out of scope of current research work. We also attempt to make a quantitative comparison of the breakdown fields obtained from our finite-rate kinetics composition with those from equilibrium composition.

Rümpler [14] extended Lindmayer's [11] work to address arc motion and extinction in a complex, realistic circuit breaker geometry using a hybrid, parallelized finite-element electro-magnetic (ANSYS) and finite-volume fluid flow (FLUENT) solver. This solver employs a "one-fluid formulation" in which the ionizing gas comprising of a mixture of air and copper is treated as a single fluid. Assumption of Local Thermodynamic Equilibrium (LTE) in the solver implies the electron and heavy particle temperatures are equal. Moreover, for calculating the thermodynamic and transport properties of the ionized gas mixture which depend upon the species mole fractions, the mole fraction values are obtained from the assumption of chemical equilibrium obtained at that particular temperature. Rümpler's model includes the effects of metallic vapor which enters the gap volume through erosion of the metallic contacts and considers a simplified P1 non-gray radiation model. He highlighted the simulation results for (a) arc voltage variation with time, (b) arc positions along the splitter plates for different arc current values (1 kA, 2 kA) and erosion rates and observed excellent agreement with experimental results. His CFD simulation's duration is extended beyond arc extinction to a few milliseconds (ms) post-CZ, which would provide the required input datasets for the current research work. As of date, the CFD solver also includes the effects of plastic vapor (PA-66) emanating from ablation of side walls.

2.3 Overview of possible approaches

Based on our literature survey, one of the possible approaches would be to track the streamer breakdown [43, 52] for a general circuit breaker geometry using the following species continuity equations for each species "p":

$$\frac{\partial n_p}{\partial t} + \nabla \cdot \mathbf{\Gamma}_p = S_p, \tag{2.1}$$

where, the flux $\vec{\Gamma_p}$ is given by:

$$\mathbf{\Gamma}_p = \pm \mu_p \boldsymbol{E} n_p - D \nabla n_p, \tag{2.2}$$

where, n_p represents number density of the species under consideration (electron, positive ion, negative ion or metastable), $\mu_p \boldsymbol{E}$ is the species drift velocity and D is the

diffusion coefficient. The mobility μ_p can be calculated from the EEPF. The term S_p represents the source term related to the generation and loss of species through reactions like ionization, recombination, attachment and photo-ionization. The reaction rate coefficients can be obtained from the EEPF or experimental data. The equations for species conservation are coupled and result in space-charge generation which can be calculated from Gauss' equation:

$$\nabla \cdot \boldsymbol{E} = \frac{e\,(n_+ - n_e - n_-)}{\epsilon_0}, \tag{2.3}$$

where, n_+, n_e and n_- are the number densities of positive ions, electrons and negative ions respectively. With appropriate boundary conditions, the equations (2.1)-(2.3) can be solved numerically to obtain the number densities of the important species considered. There are several disadvantages with this approach. Firstly, we consider approximately 150 species including several metastable and hydrocarbon species in this research work which makes the task of solving the afore-mentioned equations highly cumbersome. Secondly, this approach has been considered for simpler geometries, while the circuit breakers under consideration have complex 3D geometries. Finally, there exists a necessity of adaptive mesh refinement in the vicinity of an avalanche to obtain accurate values of the electric field distortion, arising from the charge density distribution in the right-hand side of equation (2.3). Adaptive mesh algorithms are computationally expensive, especially for complex geometries. Hence, this approach is avoided and is superseded by a simpler and general approach. The approach followed in current thesis is explained in detail in the next chapter.

Chapter 3

Computation methodology

3.1 Brief overview

Rümpler [14] has devised a Computational Fluid Dynamics solver, referred to as "CFD solver" for convenience, for modeling arc motion and extinction in realistic three-dimensional (3D) LVCB geometries. The CFD solver, written using the framework of ANSYS/FLUENT software modules, solves fluid flow and electro-magnetic conservation equations simultaneously. The highlight of the CFD solver is the assumption of a "one-fluid" formulation, in which the constituent *components* are taken to be air, metal and plastic vapor. In this formulation, the species conservation equations are solved for just the metal and plastic vapors instead of the individual *species* constituting the gas mixture and hence, it results in a considerable reduction of the computational time. The thermodynamic and transport properties required for the relevant conservation equations are obtained by calculating the species composition assuming chemical equilibrium. The CFD solver in its current form, which is capable of predicting thermal breakdown, is insufficient for predicting dielectric breakdown owing to its inability to capture non-equilibrium effects contributing towards dielectric breakdown. The solver resulting from this thesis work, referred to as "Kinetics solver" for convenience, obtains relevant inputs from the CFD solver and predicts the probability of dielectric breakdown along different paths within the LVCB geometry. The probability of dielectric breakdown is quantified using dielectric breakdown fields, which are calculated with the inclusion of important non-equilibrium effects observed experimentally.

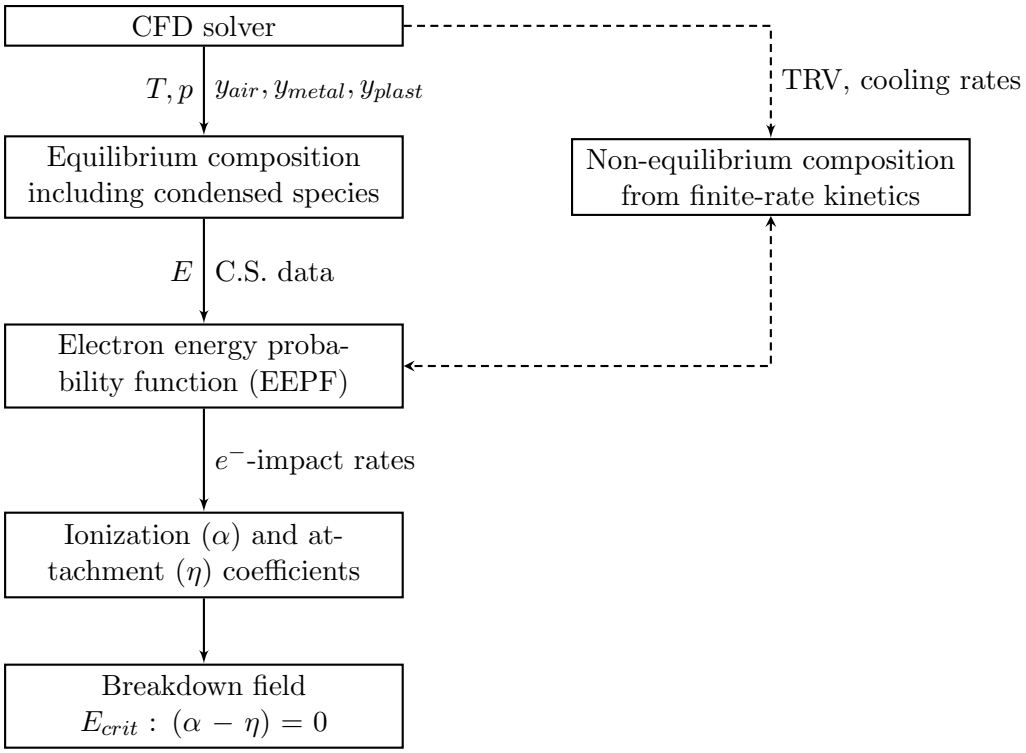

Figure 3.1: Flowchart for the computation methodology

Calculation of dielectric breakdown field requires the following inputs : (a) pressure, (b) temperature and (c) species composition. The species composition depends upon the mass fractions of constituent components in the mixture and could correspond to either: (i) chemical equilibrium approximation or (ii) chemical non-equilibrium. In the few microseconds (μs) before CZ, the gas within the contact gap has temperatures above 10,000 K and hence, is highly ionized. At these high temperatures, the chemical reactions between the constituent species occur at extremely high reaction rates. The chemical reactions time scales are on the order of nanoseconds (ns) and compared to the fluid dynamic time scales on the order of μs, occur almost instantaneously. However, when the gas temperature decays rapidly after arc extinction and the TRV appears after a delay time of few nanoseconds post-CZ, significant deviations from chemical equilibrium have been observed experimentally. These deviations are primarily due to non-Maxwellian electron-energy probability function (EEPF) owing to

higher electric fields and finite-rate chemical kinetic effects owing to lower reaction rates at temperatures below 8,000 K. One of the key objectives of this thesis is to quantify the deviation from chemical equilibrium for different possible temperature decay and TRV profiles post-CZ. In this chapter, we first describe the methodology for calculating the dielectric breakdown fields with the species composition obtained from chemical equilibrium assumption. Subsequently, following the high-voltage circuit breaker literature, we describe the methodology for solving chemical kinetics rate equations to obtain non-equilibrium species composition. The non-equilibrium species composition, which includes the effects of convective cooling and non-Maxwellian EEPF based reaction rates, will be utilized to calculate the dielectric breakdown fields for different temperature decay and TRV profiles. Finally, the deviation between the non-equilibrium and equilibrium breakdown fields will be tabulated at different time instants.

The overall methodology is presented as a flow chart in figure 3.1. We first consider the case of chemical equilibrium. Given the pressure(p), temperature (T) and mass fractions of air, metal and plastic vapor (y_{air}, y_{metal} and y_{plast}) from the CFD solver, the chemical equilibrium based species composition is obtained using the free-energy minimization technique. Subsequently, for a given electric field (E) and the equilibrium composition, the EEPF is calculated using a Boltzmann equation solver. The Boltzmann solver requires electron-impact collision cross sections (C.S.) as input, which are gathered from standard databases. The electron-impact reaction rates are then computed using the EEPF and cross sections. Finally, the net ionization coefficient ($\bar{\alpha}$), which is the difference between the electron-impact ionization (α) and attachment (η) reaction rate coefficients, $\alpha - \eta$, is calculated. The afore-mentioned steps are repeated for different values of E until the value of $\bar{\alpha}$ equals zero and this electric field is termed the critical electric field or the dielectric breakdown field (E_{crit}). In the case of chemical non-equilibrium, the temperature decay and TRV (or, E) profiles over a stipulated time interval are taken as input from the CFD solver. The convective cooling rate can be calculated from the temperature decay profile. The pressure is assumed to be constant over the time interval which is a valid assumption for post-CZ conditions. Starting from an initial temperature T_{init} and a corresponding equilibrium composition, the finite-rate kinetics solver calculates the variation of species composition with time by solving the

reaction rate equations. For the reactions involving electrons, the reaction rates are obtained from the Boltzmann EEPF solver. The species composition, and hence the E_{crit} value, at each time instant are expected to be different from those obtained with the equilibrium assumption. The magnitude of deviation of the non-equilibrium based E_{crit} value from the corresponding equilibrium value provides an estimate for the validity of the chemical equilibrium assumption.

3.2 Chemical equilibrium composition

3.2.1 Definition of free energies

The assumption of local thermodynamic equilibrium (LTE) implies thermal, kinetic and chemical equilibrium. Kinetic equilibrium is particularly relevant for a plasma where ionized species are present and is observed when the electron and heavy-particle temperatures are equal. According to the second law of thermodynamics, when a closed system undergoes a process transforming it from one equilibrium state to the other, the final state corresponds to a minimum total energy and maximum entropy. The combined effect of minimized total energy and maximized entropy can be captured with the concept of "free energy" and for a general process, the change in free energy during the process between two equilibrium states is less than or equal to zero. In this section, the two free energies used in chemical equilibrium computations are the: (i) Gibbs free energy (G) and (ii) Helmholtz free energy (F). For a general process with the aforementioned inequality, the differentials of G and F for a multi-species system are defined as [53]:

$$\begin{aligned} dG &= Vdp - SdT + \sum_i \mu_i dx_i \leq 0 \text{ and} \\ dF &= -pdV - SdT + \sum_i \mu_i dx_i \leq 0, \end{aligned} \tag{3.1}$$

respectively. The equality (inequality) in the above equation corresponds to a reversible (irreversible) process. The variables p, V, T, S, μ and x denote pressure, volume, temperature, entropy, chemical potential and number of moles respectively. The summation in the last term indicates the summation over contribution from individual species in

the multi-species system. It can be observed that G is the preferred state function for processes involving constant pressure and temperature while F is preferred for processes involving constant temperature and volume. From (3.1), the chemical potential μ_i for a species "i" can be defined as:

$$\mu_i = \left(\frac{\partial G}{\partial x_i}\right)_{p,T,x_{j\neq i}} = \left(\frac{\partial F}{\partial x_i}\right)_{T,V,x_{j\neq i}} \tag{3.2}$$

In the case of an ideal gas mixture, μ_i can be derived in terms of the partial pressure p_i (in atm) as:

$$\mu_i = \mu_i^0 + RT \ln\left(\frac{p_i}{p_i^0}\right) = \mu_i^0 + RT \ln p + RT \ln\left(\frac{x_i}{X}\right) \tag{3.3}$$

where, μ^0 is the standard chemical potential at the reference pressure of $p_i^0 = 1\ atm$ and is related to the total partition function $Z_{i,tot}$ through:

$$\mu_i^0 = -\hat{R}T \ln\left(Z_{i,tot}\right) + h_i^0, \tag{3.4}$$

where, $\hat{R}$ is the universal gas constant and h_i^0 is the enthalpy of formation at p_i^0 and T_0. Also, $X{=}\sum_i x_i$ is the total number of moles and $p{=}\sum_i p_i$ is the total pressure. The total Gibbs free energy G for a multi-species system is given by:

$$G = \sum_i x_i \mu_i, \tag{3.5}$$

and the condition for equilibrium a process at constant pressure and temperature can be obtained from (3.1) as:

$$dG = \sum_i \mu_i dx_i = 0. \tag{3.6}$$

Similar definitions can be deduced for the total Helmholtz free energy F.

3.2.2 Calculation of total partition functions

From (3.4), it can be observed that the calculation of μ_i^0 for species "i" requires the knowledge of the total partition function $Z_{tot,i}$ of that species. $Z_{tot,i}$ is the product of

the translational partition function $Z_{trans,i}$ and internal partition function $Z_{int,i}$:

$$Z_{tot,i} = Z_{trans,i} Z_{int,i} \tag{3.7}$$

Using statistical theory, $Z_{trans,i}$ can be derived as [53]:

$$Z_{trans,i} = \left(\frac{2\pi m_i k T_i}{h^2} \right)^{\frac{3}{2}}, \tag{3.8}$$

where, m_i and T_i refer to the mass and temperature of species "i". In the case of plasmas under kinetic non-equilibrium, the electron temperature T_e is not equal to the heavy-particle temperature T_h for plasmas under kinetic non-equilibrium. On the other hand, $T_i = T_e = T_h = T$ for LTE plasmas. $Z_{int,i}$ corresponds to the different internal modes of energy, with the electronic mode available for all types of heavy species. Diatomic and polyatomic species introduce complications since they possess additional modes, namely rotational and vibrational, compared to the monatomic species. It will be shown in later subsections that the thermodynamic properties enthalpy (h) and specific heat (C_p) require the knowledge of $Z_{int,i}$ in addition to the species composition.

Internal partition functions of diatomic species

$Z_{int,i}$ is calculated using the elaborate procedure of Drellishak *et al.* [54], a brief summary of which is presented here. Drellishak's procedure is highly accurate because it takes into account the coupling between rotational and vibrational energy levels:

$$Z_{int,i} = \frac{1}{\sigma} \sum_{e} g_e e^{-E_e/kT} \sum_{r,v} g_r g_v e^{-E_{r,v}(e)/kT} \tag{3.9}$$

For each electronic energy level "e", there are several vibrational energy levels "v" coupled with multiple rotational energy levels "r" and the summation needs to be performed over all permissible v and r levels for a given e level. The final summation is over all the allowable e levels. In (3.9), g and E denote the degeneracy and energy of the suitable energy mode respectively. In particular, the rotational degeneracy is calculated from the rotational quantum number J using: $g_r = 2J + 1$. σ is the symmetry factor which is equal to 1 (2) for a diatomic molecule with two different (similar) atoms.

The coupled vibrational-rotational energy term $E_{r,v}(e)$ can be expressed as a sum of a vibrational energy term $E_v(e)$ and a rotational energy term $E_r(e,v)$:

$$E_{r,v}(e) = E_v(e) + E_r(e,v) \tag{3.10}$$

Substituting (3.10) into (3.9) results in an expanded expression for $Z_{int,i}$:

$$Z_{int,i} = \frac{1}{\sigma}\sum_{e} g_e e^{-E_e/kT_{ex}} \sum_{v=0}^{v_{max}} g_v e^{-E_v(e)/kT_{vib}} \sum_{J=0}^{J_{max}} g_r e^{-E_r(e,v)/kT_{rot}} \tag{3.11}$$

where, the rotational temperature T_{rot}, vibrational temperature T_{vib} and excitation temperature T_{ex} need not be equal in general. For LTE plasmas, $T_{rot} = T_{vib} = T_{ex} = T$ while for two-temperature plasmas, $T_{rot} = T_{vib} = T_h$ and $T_{ex} = T_e$. In (3.11), the vibrational term $E_v(e)$ depends upon the zero-point vibrational energy $E_0(e)$, vibrational quantum number v and spectroscopic constants ω_e, $\omega_e x_e$, $\omega_e y_e$ and $\omega_e z_e$ through [55]:

$$\begin{aligned}
E_v(e) &= E_0(e) + hc(\omega_0 v - \omega_0 x_0 v^2 + \omega_0 y_0 v^3 + \omega_0 z_0 v^4), \text{ with,} \\
E_0(e) &= 0.5\omega_e - 0.25\omega_e x_e + 0.125\omega_e y_e + 0.0625\omega_e z_e, \\
\omega_0 &= \omega_e - \omega_e x_e + 0.75\omega_e y_e + 0.125\omega_e z_e, \\
\omega_0 x_0 &= \omega_e x_e - 1.5\omega_e y_e - 1.5\omega_e z_e, \\
\omega_0 y_0 &= \omega_e y_e + 2\omega_e z_e, \\
\omega_0 z_0 &= \omega_e z_e
\end{aligned} \tag{3.12}$$

and the rotational term $E_r(e,v)$ depends upon J, reduced molecular mass μ and spectroscopic constants B_e, D_e, α_e, β_e, r_e and ω_e through [55]:

$$\begin{aligned}
E_r(e,v) &= B_v J(J+1) - D_v J^2(J+1)^2, \text{ with,} \\
B_v &= B_e - \alpha_e(v+0.5), \\
D_v &= D_e - \beta_e(v+0.5), \\
B_e &= \frac{h}{8\pi\mu c r_e^2}, \\
D_e &= \frac{4B_e^3}{\omega_e^2}
\end{aligned} \tag{3.13}$$

It is worth noting that $E_r(e, v)$ depends on the vibrational quantum number v. The list of electronic levels for diatomic species considered in this work, which are required for the first summation in (3.11), and their corresponding spectroscopic constants are taken from Herzberg [56].

For numerically determining the second and third summations in (3.11), the upper limits for J (J_{max}), v (v_{max}) are required. v_{max} can be determined by assuming that the dissociation energy D_0 (cm^{-1}) is the maximum possible energy level attainable for a vibrating molecule and using this assumption in (3.12) for each rotationless (J=0) state:

$$D_0 = \omega_0 v_{max} - \omega_0 x_0 v_{max}^2 + \omega_0 y_0 v_{max}^3 + \omega_0 z_0 v_{max}^4 \tag{3.14}$$

The Jenkins-Traub algorithm [57] to find zeros of a general complex polynomial is used to solve (3.14) and obtain the pair: (v=v_{max}, J=0). Similar v-J pairs need to be obtained for each v in the range $0 \leq v \leq v_{max}$. The J value is determined by comparing the minimum "effective" potential of a rotating-vibrating molecule [54]:

$$U_m(r_m) = D_e' \left[1 - e^{-2\beta\xi_m}\right] + \frac{h}{8\pi\mu c r_m^2} J(J+1) \tag{3.15}$$

with the minimum from the coupled rotational-vibrational energy sum of (3.12) and (3.13) for a given v' [54]:

$$U_m = \frac{E_0}{hc} + \omega_0 v' - \omega_0 x_0 v'^2 + \omega_0 y_0 v'^3 + \omega_0 z_0 v'^4 + B_v J(J+1) - D_v J^2 (J+1)^2 \tag{3.16}$$

In (3.15), D_e' (cm^{-1}) is the dissociation energy of the given state measured from the minimum of the potential curve, r_m is the internuclear separation at the potential minimum, ξ and β are defined as:

$$\begin{aligned} \xi &= \frac{r - r_e}{r_e} \\ \beta &= \frac{\omega_e}{4(B_e D_e')^{0.5}} \end{aligned} \tag{3.17}$$

respectively. Equations (3.15) and (3.16) are simultaneously solved using a bisection root-finding algorithm to compute J for a given v'. Henceforth, the desired v-J pairs are obtained and $Z_{int,i}$ in (3.11) is evaluated.

Internal partition functions of polyatomic species

$Z_{int,i}$ for polyatomic molecules can be calculated using an extension of the procedure for diatomic molecules. However, the lack of experimental data for higher vibrational-rotational energy levels including the ground electronic state precludes an elaborate calculation of $Z_{int,i}$ for polyatomic molecules. A simplifying approximation termed the "rigid rotator-harmonic oscillator" model is used, in which $Z_{int,i}$ is expressed as a product of partition functions for a rigid rotator Z_{r-r} and harmonic oscillator Z_{h-o} at the electronic ground state of the polyatomic molecule [55]:

$$
\begin{aligned}
Z_{int,i} &= g_e Z_{r-r} Z_{h-o}, \text{ where,} \\
Z_{h-o} &= \prod_{p=1}^{n} \left[1 - e^{\left(-\frac{hc}{kT}\nu_p\right)}\right]^{-d_p}, \\
Z_{r-r} &= \frac{1}{\sigma}\frac{kT}{hcB_0} \text{ for linear molecules, and,} \\
Z_{r-r} &= \sqrt{\frac{\pi}{A_0 B_0 C_0}\left(\frac{kT}{hc}\right)^3} \text{ for non-linear molecules.}
\end{aligned}
\tag{3.18}
$$

In (3.18), the ground state degeneracy g_e, the vibrational frequency ν_p, vibrational state's degeneracy d_p and the rotational constants A_0, B_0, C_0 for polyatomic species in this work are obtained from the NIST-JANAF thermochemical tables [58]. A_0, B_0, C_0 are the rotational constants in the ground vibrational state related to the principal moments of inertia I_A, I_B, I_C as:

$$
A_0 = \frac{h}{8\pi^2 c I_A}, B_0 = \frac{h}{8\pi^2 c I_B}, C_0 = \frac{h}{8\pi^2 c I_C} \tag{3.19}
$$

Internal partition functions of monatomic species

$Z_{int,i}$ for monatomic species, owing to the lack of vibrational and rotational energy modes, is simply the first summation in (3.9) [55]:

$$
Z_{int,i} = \sum_{e} g_e e^{-E_e/kT} \tag{3.20}
$$

Theoretically, there are infinite number of states below the ionization limit and this would result in a divergent summation. However, an upper limit for electronic energy E_{max} needs to be specified to numerically obtain a convergent sum [59]. E_{max} is the cut-off energy resulting from lowering the ionization potential E_i of the species by a suitable value ΔE_i using Griem's criterion [54]:

$$\Delta E_i = (Q_i + 1)\frac{e^2}{4\pi\epsilon_0\lambda_D}, \tag{3.21}$$

and the summation in (3.20) is performed over all energy levels lower than $E_{max} = E_i - \Delta E_i$. In (3.21), Q_i is the species charge, λ_D is the Debye length based on species number densities n_i given by:

$$\lambda_D = \left(\frac{\epsilon_0 k/e^2}{\sum\limits_{j, j\neq e^-} Q_j^2 n_j/T_h + n_e^2/T_e} \right)^{\frac{1}{2}} \tag{3.22}$$

The first term in the denominator of (3.22) indicates summation over the heavy species only.

Having obtained the total partition functions $Z_{tot,i}$ and hence, the chemical potentials μ_i for the species considered in this work, we now proceed to the implementation of free-energy minimization technique. In this thesis work, the gas mixtures under consideration include the presence of condensed species at temperatures lower than 4000 K. For the purpose of validating equilibrium composition results at temperatures greater than 4000 K, the minimization of free energy (3.6) was solved using two different approaches - (i) White's method, by solution of a set of linear equations and (ii) Godin's method, by solution of a set of non-linear equations using Newton's algorithm. The characteristic features, inherent advantages and drawbacks of each method will be briefly discussed in the following subsections.

3.2.3 White's method - including condensed species

White's method [60] belongs to the category of gradient-descent based optimization algorithms and is termed as "Method of steepest descent with a quadratic fit". This

method has been extended to include multi-phase condensed species by Eriksson [61]. In order to deal with smaller magnitude scalars, the total Gibbs free energy G in (3.5) is scaled by the product $\hat{R}T$ and this results in the dimensionless quantity $\left(\mu_i/\hat{R}T\right)$ from (3.3). The scaled total Gibbs free energy $\left(G/\hat{R}T\right)$ (in mol), including the presence of condensed species, is written as:

$$\frac{G}{\hat{R}T} = \sum_{i=1}^{N_g} x_i^g \left[\left(\frac{\mu^0}{\hat{R}T}\right)_i^g + \ln p + \ln\left(\frac{x_i^g}{X}\right)\right] + \sum_{i=1}^{N_c} x_i^c \left(\frac{\mu^0}{\hat{R}T}\right)_i^c \tag{3.23}$$

where, the superscripts "g" and "c" denote the gaseous and condensed species respectively, while N_g and N_c denote the number of gaseous and condensed species respectively. In this work, White's method is used to calculate equilibrium composition in the temperature range 300-6000 K owing to greater computational speeds. The source of greater computational speed pertains to the evaluation of μ_i^0. From the previous subsection, it can be clearly observed that one of the most computationally intensive portions involve the calculation of $Z_{tot,i}$, and hence μ_i^0, for each temperature and pressure input. Fortunately, $\left(\mu^0/\hat{R}T\right)$ in (3.23) can be calculated straight-forwardly from the standard quantities $\left(G^0 - H^0\right)/T$ and $\Delta_f H^0$ in the NIST-JANAF thermochemical tables [58] using the formula:

$$\left(\frac{\mu^0}{\hat{R}T}\right) = \frac{1}{\hat{R}}\left[\frac{\left(G^0 - H^0_{T_r}\right)}{T}\right] + \left(\frac{\Delta_f H^0_{T_r}}{\hat{R}T}\right) \tag{3.24}$$

where, H^0 and $\Delta_f H^0$ are computed at standard pressure $p^0 = 1\ atm$ and reference temperature $T_r = 298\ K$.

Lagrange's method of undetermined multipliers is then applied to determine a minimum value of $\left(G/\hat{R}T\right)$ in (3.23), subject to the elemental mass-balance relations as auxiliary conditions:

$$\sum_{i=1}^{N_g} a_{ij}^g x_i^g + \sum_{i=1}^{N_c} a_{ij}^c x_i^c = b_j,\ (j = 1, 2, ..., N_{el}) \tag{3.25}$$

where, a_{ij} represents the number of atoms of the j^{th} element in a molecule i, b_j is the total number of moles of the j^{th} element and N_{el} is the total number of elements.

The b_j $(j = 1, 2, ..., N_{el} - 1)$ values are determined from the input mass fractions of air, metal and plastic vapors : y_{air}, y_{metal} and y_{plast}. In the presence of electrons and ionic species, electrons are taken to be the final element N_{el}. The final constraint that needs to be added to the mass-balance relations is the condition of charge conservation or electro-neutrality. Electro-neutrality is imposed by setting $a_{i,N_{el}} = Q_i$, where Q_i is the electric charge of the i^{th} species, and $b_{N_{el}} = 0$. Using the Lagrange multipliers π_j $(j = 1, 2, ..., N_{el})$, the following equations can be obtained for gaseous and condensed species:

$$\left(\frac{\mu^0}{\hat{R}T}\right)_i^g + \ln p + \ln\left(\frac{x_i^g}{X}\right) - \sum_{j=1}^{N_{el}} \pi_j a_{ij}^g = 0, \ (i = 1, 2, ..., N_g), \tag{3.26}$$

$$\left(\frac{\mu^0}{\hat{R}T}\right)_i^c - \sum_{j=1}^{N_{el}} \pi_j a_{ij}^c = 0, \ (i = 1, 2, ..., N_c) \tag{3.27}$$

Expanding the mass-balance constraints (3.25) and gaseous species equation (3.26) in a Taylor's series about an arbitrary initial guess of mole numbers (y_i^g $(i = 1, ..., N_g)$, y_i^c $(i = 1, ..., N_c)$) and neglecting second or higher order derivatives, we obtain [61]:

$$\sum_{i=1}^{N_g} a_{ij}^g y_i^g + \sum_{i=1}^{N_c} a_{ij}^c y_i^c - b_j + \sum_{i=1}^{N_g} a_{ij}^g \left(x_i^g - y_i^g\right) + \sum_{i=1}^{N_c} a_{ij}^c \left(x_i^c - y_i^c\right) = 0, \ (j = 1, 2, ..., N_{el}) \tag{3.28}$$

and:

$$\left(\frac{\mu^0}{\hat{R}T}\right)_i^g + \ln p + \ln\left(\frac{y_i^g}{Y}\right) - \sum_{j=1}^{N_{el}} \pi_j a_{ij}^g + \left(\frac{x_i^g}{y_i^g}\right) - \left(\frac{X}{Y}\right) = 0, \ (i = 1, 2, ..., N_g) \tag{3.29}$$

respectively where, $Y = \sum_{i=1}^{N_g} y_i^g$. Rearranging (3.29), we can calculate x_i^g:

$$x_i^g = -f_i + y_i^g \left[\left(\frac{X}{Y}\right) + \sum_{j=1}^{N_{el}} \pi_j a_{ij}^g\right], \ (i = 1, 2, ..., N_g) \text{ where,} \tag{3.30}$$

$$f_i = y_i^g \left[\left(\frac{\mu^0}{\hat{R}T}\right)_i^g + \ln p + \ln\left(\frac{y_i^g}{Y}\right)\right]$$

Additionally, a correction term C_j is defined as the deviation of the mass-balance constraint from zero, based on gaseous species' initial guess alone:

$$C_j = \sum_{i=1}^{N_g} a_{ij}^g y_i^g - b_j, \ (j = 1, 2, ..., N_{el}) \tag{3.31}$$

Substituting (3.30) and (3.31) into (3.28) and rearranging gives:

$$\sum_{k=1}^{N_{el}} \pi_k r_{jk} + \left[\frac{X}{Y} - 1\right] \sum_{i=1}^{N_g} a_{ij}^g y_i^g + \sum_{i=1}^{N_c} a_{ij}^c x_i^c = \sum_{i=1}^{N_g} a_{ij}^g f_i - C_j, \ (j = 1, 2, ..., N_{el}) \tag{3.32}$$

where, r_{jk} are elements of a symmetric matrix given as:

$$r_{jk} = r_{kj} = \sum_{i=1}^{N_g} \left(a_{ij}^g a_{ik}^g\right) y_i^g, \ (j, k = 1, 2, ..., N_{el}) \tag{3.33}$$

Finally, summing (3.30) over N_g and rearranging, we obtain:

$$\sum_{j=1}^{N_{el}} \pi_j \left(\sum_{i=1}^{N_g} y_i^g a_{ij}^g\right) = \sum_{i=1}^{N_g} f_i \tag{3.34}$$

Thus, (3.27), (3.32) and (3.34) form a system of $(N_c + N_{el} + 1)$ linear equations corresponding to the $(N_c + N_{el} + 1)$ unknown variables: x_i^c $(i = 1, 2, ..., N_c)$, π_j $(j = 1, 2, ..., N_{el})$ and $[X/Y - 1]$. Once π_j $(j = 1, 2, ..., N_{el})$ and X/Y are obtained from the solution of these equations, x_i^g can be calculated from (3.30).

Iteration steps for a converged solution

Step 1: Given a suitable initial guess y_i $(i = 1, 2, ..., N_c + N_g)$, the mole numbers x_i $(i = 1, 2, ..., N_c + N_g)$ are determined by simultaneously solving the set of linear equations.

Step 2: The x_i need to be non-negative. If $x_i \geq 0$, they are used as the initial guess y_i' for the next iteration. In other words, the value of λ $(0 \leq \lambda \leq 1)$ in:

$$y_i' = y_i + \lambda \delta_i$$

is set equal to 1. Here, δ_i is the deviation of x_i from y_i: $\delta_i = (x_i - y_i)$.

Step 3: In general, however, *Step* 1 yields negative mole numbers for several species. In such cases, the goal is to obtain a λ_{min} which results in positive mole numbers y_i'. Using y_i' as the mole number values in (3.23) and taking the derivative with respect to λ, we get:

$$\frac{d\left(\frac{G(\lambda)}{\hat{R}T}\right)}{d\lambda} = \sum_{i=1}^{N_g} \delta_i^g \left[\left(\frac{\mu^0}{\hat{R}T}\right)_i^g + \ln p + \ln \left(\frac{y_i^g + \lambda\delta_i^g}{\sum_{i=1}^{N_g}(y_i^g + \lambda\delta_i^g)} \right) \right] + \sum_{i=1}^{N_c} \delta_i^c \left(\frac{\mu^0}{\hat{R}T}\right)_i^c$$

λ_{min} is the greatest number for which the derivative is negative.

Step 4: For faster convergence towards the solution, the species with mole fractions:

$$\frac{y_i'}{\sum_i y_i'} \leq 10^{-5}$$

are removed for the next iteration.

Step 5: Repeat steps 1-4 until the following convergence criterion is satisfied:

$$\sum_{i=1}^{N_g+N_c} \left(\frac{y_i' - y_i}{y_i} \right) \leq 10^{-5}$$

3.2.4 Godin's method - excluding condensed species

In this thesis work, Godin's method [62] has been used primarily to obtain the equilibrium composition at high temperatures ($> 4000\ K$) where condensed species are absent. Some of the advantages of this method include: (i) significant reduction in the number of unknowns to be calculated for multi-species systems and (ii) easy extension to calculate the chemical composition of two-temperature plasmas for temperatures upto 50,000 K. This method minimizes the total Helmholtz free energy F formulated using particle numbers N or number densities $n = N/V$, instead of mole numbers x:

$$dF = \sum_i \mu_i dN_i = 0. \tag{3.35}$$

where, F for an ideal gas mixture is determined using statistical theory as [62]:

$$F = -kT \sum_i N_i \left[\ln \left(\frac{Z_{tot,i}}{n_i} \right) + 1 \right] \tag{3.36}$$

and the chemical potential μ_i is defined in slightly different terms compared to the last equality in (3.2):

$$\mu_i = \left(\frac{\partial F}{\partial N_i} \right)_{T,V,N_{j \neq i}} = -kT \ln \left(\frac{Z_{tot,i}}{n_i} \right) \tag{3.37}$$

In this subsection, the subscripts in Z_{tot} will be dropped for convenience and the total partition function will be symbolized by Z. We assume that there are N_{sp} species and N_{el} chemical elements constituting the species with $N_{sp} \geq N_{el}$. The most important feature of this method is the formation of a chemical basis by identifying suitable "basis species". The chemical basis is defined as the subset of N_{el} species ($\boldsymbol{b}$) from which all the other $N_{reac} = N_{sp} - N_{el}$ species, termed "non-basis species" ($\boldsymbol{b}^*$), can be created through chemical reactions. The overall composition matrix for the gas mixture $\boldsymbol{C}$ has elements $C_{i,j}$ indicating the number of atoms of element j in species i. The composition subset matrices corresponding to the basis and non-basis species are denoted by $\boldsymbol{B}$ and $\boldsymbol{B}^*$ respectively. The species making up the basis vector must be independent of each other and mathematically, the necessary and sufficient condition for a valid $\boldsymbol{b}$ is a non-singular basis matrix: $|\boldsymbol{B}| \neq 0$. Also, N_{reac} independent chemical reactions connect $\boldsymbol{b}^*$ ($\boldsymbol{B}^*$) and $\boldsymbol{b}$ ($\boldsymbol{B}$), through the coefficient matrix $\boldsymbol{\Upsilon}$:

$$B^*_{j,i} = \sum_{k=1}^{N_{el}} \upsilon_{j,k} B_{k,i} \Leftrightarrow \boldsymbol{B}^* = \boldsymbol{\Upsilon B} \tag{3.38}$$

From (3.38), $\boldsymbol{\Upsilon}$ of dimensions $N_{reac} \times N_{el}$ can be calculated [62]:

$$\boldsymbol{\Upsilon} = \boldsymbol{B}^* \boldsymbol{B}^{-1} \tag{3.39}$$

Having appropriately set up the chemical reactions, the final expression of the mass-action law for each of these reactions can be derived as:

$$n_{b^*_j} = Z_{b^*_j} \prod_{i=1}^{N_{el}} \left(\frac{n_{b_i}}{Z_{b_i}} \right)^{\upsilon_{j,i}}, (j = 1, 2, ...N_{reac}) \tag{3.40}$$

Additionally, N_{el} closure equations are needed to determine the solution and are obtained from three conservation conditions: (i) $N_{el}-2$ atomic nuclei conservation (ii) total charge conservation or electro-neutrality and (iii) total number density conservation based on the ideal gas law. For condition (i), the mass fractions (y_{air}, y_{metal} and y_{plast}) are required to form the $N_{el}-2$ ratios of nuclei numbers between constituent elements. Instead of mass fractions, it is sometimes preferable to work with mole fractions (x_{air}, x_{metal} and x_{plast}) while dealing with metallic and plastic vapors with high molecular weights. Denoting the molecular weights of air, metal and plastic vapor to be MW_{air}, MW_{metal} and MW_{plast} respectively, the mole fractions are expressed as:

$$\begin{aligned} x_{air} &= \left(\frac{y_{air}}{MW_{air}}\right)/x_{denom}, \\ x_{metal} &= \left(\frac{y_{metal}}{MW_{metal}}\right)/x_{denom}, \\ x_{plast} &= 1 - x_{air} - x_{metal}, \text{ where,} \\ x_{denom} &= \left(\frac{y_{air}}{MW_{air}} + \frac{y_{metal}}{MW_{metal}} + \frac{y_{plast}}{MW_{plast}}\right) \end{aligned} \tag{3.41}$$

The N_{el} conservation conditions can be expressed using the conservation matrix $\boldsymbol{A}$ and right hand side vector $\boldsymbol{A}^0$ as [62]:

$$\sum_{i=1}^{N_{sp}} A_{l,i} n_i = A_l^0, (l = 1, 2, ...N_{el}) \tag{3.42}$$

Separating the conservation conditions in (3.42) into basis and non-basis terms:

$$-A_l^0 + \sum_{i=1}^{N_{el}} A_{l,b_i} n_{b_i} + \sum_{j=1}^{N_{reac}} A_{l,b_j^*} n_{b_j^*} = 0, (l = 1, 2, ...N_{el}) \tag{3.43}$$

and substituting the mass-action laws in (3.40) into the last term of (3.43), we get:

$$-A_l^0 + \sum_{i=1}^{N_{el}} A_{l,b_i} n_{b_i} + \sum_{j=1}^{N_{reac}} A_{l,b_j^*} \left[Z_{b_j^*} \prod_{i=1}^{N_{el}} \left(\frac{n_{b_i}}{Z_{b_i}}\right)^{\upsilon_{j,i}} \right] = 0, (l = 1, 2, ...N_{el}) \tag{3.44}$$

The system of N_{el} non-linear equations in (3.44) is solved using Newton's method to

obtain the number densities of basis species. In the Newton's algorithm, starting from an initial guess n_{b_i} of basis number densities, corrections δn_{b_i} are added subsequently at the end of each iteration:

$$\sum_{i=1}^{N_{el}} J_{l,i}\delta n_{b_i} = R_l, (l = 1, 2, ...N_{el}) \tag{3.45}$$

where, the residual vector $\boldsymbol{R}$ and the Jacobian matrix $\boldsymbol{J}$ are determined using:

$$J_{l,i} = \frac{\partial R_l}{\partial n_{b_i}} = A_{l,b_i} - \frac{1}{n_{b_i}} \sum_{j=1}^{N_{reac}} A_{l,b_j^*} n_{b_j^*} \upsilon_{j,i}, \tag{3.46}$$

$$R_l = -A_l^0 + \sum_{i=1}^{N_{el}} A_{l,b_i} n_{b_i} + \sum_{j=1}^{N_{reac}} A_{l,b_j^*} n_{b_j^*}$$

Once the basis number densities n_{b_i} are obtained, the non-basis number densities $n_{b_j^*}$ are computed using the mass-action laws (3.40). It is worth noting that this method is computationally fast because it obviates the need to calculate (a) the total partition functions Z and (b) Jacobian derivatives $J_{l,i}$ at every iteration. However, Z are required for calculating the $n_{b_j^*}$ and the thermodynamic properties. Unlike the White's method, tabulated values for obtaining μ_i^0 are unavailable for temperatures greater than 6,000 K and hence it is not possible to sidestep the laborious calculations of $Z_{int,i}$ outlined in an earlier subsection. Nonetheless, Newton's algorithm has quadratic convergence provided that a good estimate is provided as the initial guess.

Iteration steps for a converged solution

Step 1: The species forming the chemical basis are determined using a flexible basis optimization algorithm, which ensures the independence of selected species by satisfying $|\boldsymbol{B}| \neq 0$. A proper choice of chemical basis prevents the occurrence of unphysical negative number densities. Most importantly, at temperatures close to 4000 K, the electron and ionic species mole fractions are observed to fall below 10^{-12}, resulting in a singular $\boldsymbol{B}$. At these low mole fraction levels, the basis optimization algorithm reduces N_{el} by 1 by eliminating electrons as the final basis element and neglecting the superfluous solution of electro-neutrality.

Step 2: The initial guess for a given temperature, pressure and mass fraction combination is taken from the solution for a higher temperature value at the same pressure and mass fraction values. For obtaining high degree of accuracy, keeping the pressure and mass fraction values constant, the solver obtains composition results starting from 100,000 K and ending at 4,000 K in decrements of 100 K. The initial guess for 10,000 K, for example, is the equilibrium solution at 10,100 K.

Step 3: With the initial guesses for the basis species number densities $n_{b_i}^k$, solve (3.45) iteratively to obtain the corrections $\delta n_{b_i}^{k+1}$. Here, $k+1$ and k denote the current and previous iterations respectively. The basis number densities at the current iteration are calculated using: $n_{b_i}^{k+1} = n_{b_i}^k + \delta n_{b_i}^{k+1}$. The following stringent convergence criterion based on n_{b_i} is utilized for stopping the iterations:

$$\sum_{i=1}^{N_{sp}} \left(\frac{n_{b_i}^{k+1} - n_{b_i}^k}{n_{b_i}^k} \right) \leq 10^{-10}$$

Step 4: With the availability of n_{b_i}, the mass-action laws (3.40) are used to compute the non-basis number densities $n_{b_j^*}$.

Step 5: Repeat steps 1-4 for the next temperature value ($\geq$ 4,000 K) with the pressure and mass fractions kept constant.

3.3 Electron energy probability function (EEPF)

Once the species composition has been computed, the next step is the calculation of the generalized non-Maxwellian EEPF. The appearance of TRV post-CZ across the contact gap results in an electric field acting on the gas mixture in the gap. Since there are a finite number of electrons present in the gap at temperatures in the range 2000-6000 K post-CZ, a Lorentz force $\boldsymbol{F}_{el}$ owing to the electric field $\boldsymbol{E}$ is imposed on these electrons:

$$\boldsymbol{F}_{el} = -e\boldsymbol{E} \tag{3.47}$$

The electron number densities n_e post-CZ are much smaller compared to the total gas density N, with the electron mole fractions being in the range $10^{-5} - 10^{-2}$. Under such conditions, the electrons undergo collisions with mostly neutral molecules rather than

with each other and this group of electrons is termed an "electron swarm". Some of the important physical properties of an electron swarm include drift velocity v_d, transverse diffusion coefficient D_T, electron attachment coefficient η and electron ionization coefficient α. In the absence of magnetic fields, the generalized distribution function $f(v)$ for electron velocities (EVDF) in an electron swarm is obtained from the solution of the Boltzmann equation [63]:

$$\frac{\partial f}{\partial t} + \boldsymbol{v} \cdot \nabla_{\mathbf{x}} f - e\frac{\boldsymbol{E}}{m} \cdot \nabla_{\mathbf{v}} f = \left(\frac{\partial f}{\partial t}\right)_{coll} \tag{3.48}$$

where, $\nabla_{\mathbf{x}}$ is the gradient operator in the configuration space $\mathbf{x}$, $\boldsymbol{v}$ is the velocity, v is the velocity magnitude, $\nabla_{\mathbf{v}}$ is the gradient operator in the velocity space and $\left(\frac{\partial f}{\partial t}\right)_{coll}$ is the rate of change of f due to collisions. Only two-particle or binary collisions are considered for the right-hand side term, with three-particle collisions being considered as step-wise binary collisions for example. In the absence of external forces due to electric or magnetic fields, it can be derived that an electron swarm follows a Maxwellian velocity distribution:

$$f_0^{Maxwell}(v) = n\left(\frac{m}{2\pi kT}\right)^{\frac{3}{2}} e^{-\left(\frac{mv_i v_i}{2kT}\right)} \tag{3.49}$$

where, the repeating indices in $v_i v_i$ indicate summation over the square of velocity magnitudes in each direction. It can be clearly seen that the Maxwellian EVDF is independent of $\boldsymbol{x}$. Equivalently, $f_0^{Maxwell}$ can be written in terms of the electron energy, $\epsilon = \frac{1}{2}mv^2$, as the dependent variable as:

$$F_0^{Maxwell}(\epsilon) = \frac{2}{\sqrt{\pi}}\left(\frac{1}{kT}\right)^{\frac{3}{2}} e^{-\left(\frac{\epsilon}{kT}\right)} \tag{3.50}$$

where, $F_0^{Maxwell}(\epsilon)$ is the Maxwellian electron energy probability function (EEPF). In the case of a general isotropic distribution, $f_0(v)$ and $F_0(\epsilon)$ satisfy the following normalization conditions respectively:

$$4\pi \int_0^\infty f_0(v) v^2 \, dv = n \tag{3.51}$$

$$\int_0^\infty \epsilon^{\frac{1}{2}} F_0(\epsilon) \, d\epsilon = 1 \tag{3.52}$$

Another commonly used form for the energy distribution is the electron energy distribution function (EEDF), $f_0(\epsilon)$, which is related to the EEPF as:

$$f_0(\epsilon) = \epsilon^{\frac{1}{2}} F_0(\epsilon) \tag{3.53}$$

An exact analytical solution of (3.48) is not available and certain simplifying assumptions need to be made. The first assumption is that the electric field and collision probabilities are spatially uniform within the scale of the mean free path. The former is valid within a control volume and the latter is easily satisfied since the pressures involved within an LVCB are greater than atmospheric and the mean free paths are on the order of few microns (μm). As a consequence of this assumption, f becomes symmetric in the velocity space along the electric field direction. Additionally, f is assumed to vary only along the electric field direction in the coordinate space. Expanding (3.48) in spherical coordinates, with θ being the angle between velocity and field (z) directions, we get [63]:

$$\frac{\partial f}{\partial t} + v\cos\theta\frac{\partial f}{\partial z} - \frac{eE}{m}\left(\cos\theta\frac{\partial f}{\partial v} + \frac{\sin^2\theta}{v}\frac{\partial f}{\partial \cos\theta}\right) = \left(\frac{\partial f}{\partial t}\right)_{coll} \tag{3.54}$$

Within a control volume, the collision frequency is on the order of picoseconds (ps) which implies that the EVDF quickly relaxes to a steady state compared to the kinetic or fluid dynamic time scales. For the important electron-generating ionization and electron-draining attachment processes, an additional exponential dependence of f on t or z is introduced as an approximation. The dependence of f on θ can be simplified using a two-term spherical harmonic approximation.

Two-term spherical harmonic approximation

Spherical harmonic approximation involves the expansion of f using Legendre polynomials $P_n(\cos\theta)$ of the form [63]:

$$f(z, v, \theta, t) = \sum_{n=0} f_n(z, v, t) P_n(\cos\theta) \tag{3.55}$$

The two-term approximation assumes that only the first two terms of the expansion in (3.55) are important, with $P_0 = 1$ and $P_1 = \cos\theta$, while the contribution of terms second order and higher can be neglected:

$$f(z, v, \theta, t) = f_0(z, v, t) + f_1(z, v, t)\cos\theta \tag{3.56}$$

where, f_0 and f_1 denote the isotropic portion and anisotropic corrections of f respectively. The second term in (3.56) can be viewed as a small perturbation ($f_1 \cos\theta \ll f_0$) and f_0 need not be a Maxwellian distribution in general. The two-term approximation fails when the momentum transfer cross section $\sigma_{k,mom}$ of a species k is considerably lower than the inelastic and/or ionization cross sections in the energy range of interest. For the species considered in this thesis work, we have verified that $\sigma_{k,mom}$ of each species exceeds the inelastic/ionization cross sections in the average electron energy range of 1-50 eV. Substitution of (3.56) into (3.54), integrating over $\cos\theta$ and using the orthogonality conditions, we get two different equations for the evolution of $f_0(\epsilon)$ and $f_1(\epsilon)$ [19]:

$$\frac{\partial f_0}{\partial t} + \frac{\gamma}{3}\epsilon^{\frac{1}{2}}\frac{\partial f_1}{\partial z} - \frac{\gamma}{3}\epsilon^{-\frac{1}{2}}\frac{\partial}{\partial \epsilon}(\epsilon E f_1) = C_0, \tag{3.57}$$

$$\frac{\partial f_1}{\partial t} + \gamma\epsilon^{\frac{1}{2}}\frac{\partial f_0}{\partial z} - E\gamma\epsilon^{\frac{1}{2}}\frac{\partial f_0}{\partial \epsilon} = -N\sigma_m\gamma\epsilon^{\frac{1}{2}} f_1, \tag{3.58}$$

where, the constant $\gamma = (2e/m)^{1/2}$, N is the total number density and the electron energy ϵ is measured in eV. It can be clearly observed that the evolution equations for f_0 and f_1 are inter-dependent. The total momentum transfer cross section σ_m (m^2) sums up all the contributions from different species using the species mole fraction x_k:

$$\sigma_m = \sum_k x_k \sigma_{k,mom} \tag{3.59}$$

Subsequent simplifications and numerical solution of (3.57) and (3.58) are explained in detail by Hagelaar and Pitchford [19]. The following collision processes are taken into account for the solution of f: (i) elastic scattering between electrons and neutrals, (ii) electron-impact vibrational excitation of neutrals, (iii) electron-impact electronic excitation of neutrals, (iv) super-elastic collision of electrons with excited energy levels

leading to increase in electron energy and de-excitation of the excited level, (v) electron-electron collisions responsible for Maxwellization of EEPF, (vi) gain of electrons due to electron-impact ionization of neutrals and (vii) loss of electrons due to electron-impact attachment of neutrals. The numerical values of f_0 and f_1 are obtained at certain non-uniformly distributed electron energy values, whose values are determined by the EEPF solver.

3.4 Dielectric Breakdown field

Once the discretized numerical solution of f_0, and hence F_0, are obtained, several electron swarm parameters can be easily calculated. The drift velocity $\boldsymbol{v}_d$ is defined as the velocity acquired by the center of mass of the electron swarm in an electric field and is directed opposite to the electric field $\boldsymbol{E}$. The magnitude of $\boldsymbol{v}_d$ can be calculated from F_0 using [19]:

$$v_d = \mu_e E = -\frac{\gamma}{3}\frac{E}{N}\int_0^\infty \frac{\epsilon}{\sigma_m}\frac{\partial F_0}{\partial \epsilon}\, d\epsilon \tag{3.60}$$

where, μ_e is the electron mobility. The electron swarm tends to spread as a result of its random motion which is characterized by its diffusion coefficient D. However, this diffusion is, in general, anisotropic in the presence of an electric field. Hence, diffusion is characterized by two different components: (i) longitudinal diffusion coefficient D_L parallel to the field and (ii) transverse diffusion coefficient D_T perpendicular to the field. D_T can be obtained from F_0 as:

$$D_T = \frac{\gamma}{3N}\int_0^\infty \frac{\epsilon}{\sigma_m} F_0\, d\epsilon \tag{3.61}$$

For electric fields on the order of a few V/cm, the ratio D_T/μ_e is observed to be equal to the mean energy of electrons and hence is a measure of the electron temperature T_e. The mean energy of electron swarm, $\bar{\epsilon}$, is related to F_0 by:

$$\bar{\epsilon} = \int_0^\infty \epsilon^{\frac{3}{2}} F_0\, d\epsilon \tag{3.62}$$

and for a Maxwellian distribution pertaining to negligible electric fields, t is given by:

$$\bar{\epsilon}_{Maxwell} = \frac{3}{2} kT_e \tag{3.63}$$

On the other hand, a definition of temperature is not possible for electric fields on the order of several kV/cm owing to thermal non-equilibrium in the electron swarm. Nonetheless, the ratio D_T/μ_e serves as a measure of the swarm's energy content and for this reason, is conveniently referred to as the characteristic energy:

$$e\frac{D_T}{\mu_e} = F_d \bar{\epsilon}_{Maxwell} \tag{3.64}$$

where, F_d is a factor based on the electron energy distribution and equals 2/3 for Maxwellian distribution.

Calculation of E_{crit} requires the knowledge of the ionization (α) and attachment (η) coefficients. In the literature, it is a common practice to scale the coefficients α and η by the total number density N and label the value E_{crit}/N as the critical reduced electric field for which the net reduced ionization coefficient $\bar{\alpha}/N = (\alpha/N - \eta/N)$ equals zero. Possible electron-impact ionization and attachment reactions involving different neutral species are considered, for which the ionization and attachment cross sections are attainable from literature. The reaction rates R_k for the k^{th} reaction involving a neutral species and an electron can be written as:

$$R_k = k_k n_k n_e \tag{3.65}$$

where, n_k is the number density of the neutral species involved in the k^{th} reaction, n_e is the electron number density and the rate coefficients for the k^{th} reaction k_k can be easily calculated from F_0 and σ_k:

$$k_{k,ioniz} = \gamma \int_0^\infty \epsilon \sigma_{k,ioniz} F_0 \, d\epsilon \tag{3.66}$$

$$k_{k,attac} = \gamma \int_0^\infty \epsilon \sigma_{k,attac} F_0 \, d\epsilon \tag{3.67}$$

where, the subscripts "ioniz" and "attac" refer to the ionization and attachment reactions respectively. If there are N_{ioniz} ionization and N_{attac} attachment reactions respectively, $\bar{\alpha}/N$ is then calculated using:

$$\frac{\bar{\alpha}}{N} = \left(\frac{\alpha}{N} - \frac{\eta}{N}\right) = \frac{1}{N}\left(\sum_{k=1}^{N_{ioniz}} x_k k_{k,ioniz} - \sum_{k=1}^{N_{attac}} x_k k_{k,attac}\right) \tag{3.68}$$

The tabulated values of elastic momentum (σ_{mom}), ionization (σ_{ioniz}) and attachment cross sections (σ_{attac}) (m^2) are available at discrete electron energies (eV) from standard databases. Using a bisection root-finding algorithm, the E/N for which $\bar{\alpha}/N$ in (3.68) becomes equal to zero, is computed. With (3.68) being highly non-linear, the bisection algorithm needs to be modified to take into the possibility of multiple roots. The physically acceptable root is then taken to be the reduced dielectric breakdown field, E_{crit}/N.

3.5 Thermodynamic and transport properties

Apart from the electric-field dependent electron swarm properties, basic thermodynamic and transport properties can be calculated using the chemical composition of a gas mixture. In this thesis work, results for LTE thermodynamic properties are presented for air-metal-plastic vapor mixtures while transport properties are presented for air-metal vapor mixtures alone. Extension of the transport properties' calculations to two-temperature plasma and the effects of plastic vapor will be considered in future work.

3.5.1 Thermodynamic properties

The mass density ρ (kg/m^3), specific energy e (J/kg) and specific enthalpy h (J/kg) are calculated from the species number densities n_s and their partition functions $Z_{tot,s}$ by:

$$\rho = \sum_{s=1}^{N_{sp}} m_s n_s, \tag{3.69}$$

$$e = \frac{1}{\rho}\left[\sum_{s=1}^{N_{sp}}\left\{n_s k T_s^2\left(\frac{\partial \ln Z_{tot,s}}{\partial T}\right) + n_s E_{form,s}\right\}\right] \tag{3.70}$$

$$h = e + \frac{p}{\rho} \tag{3.71}$$

where, $E_{form,s}$ (J) denotes the energy of formation required for species s and N_{sp} is the total number of species in the gas mixture. For monatomic species and their multiply-charged ions, half the dissociation energy of its symmetric parent neutral diatomic molecule must be included into $E_{form,s}$ in addition to the appropriate ionization energies. The specific heats $(J/kg/K)$ at constant volume c_v and constant pressure c_p are related to e and h respectively by:

$$c_v = \left(\frac{\partial e}{\partial T}\right)_v, \tag{3.72}$$

$$c_p = \left(\frac{\partial h}{\partial T}\right)_p = c_v + R, \tag{3.73}$$

where, $R = \hat{R}/MW_{gas}$ $(J/kg/K)$ is the specific gas constant with MW_{gas} being the molecular weight of the gas mixture.

3.5.2 Transport properties

The transport properties for partially-ionized gas mixtures in this work are obtained from an approximate solution of the Boltzmann equation (3.48) using the Chapman-Enskog method [64,65]. In the Chapman-Enskog method, the distribution function f is expanded using a zeroth-order Maxwellian distribution f^0 and a first-order perturbation $f^1 = \phi f^0$, where ϕ is on the order of the Knudsen number Kn:

$$f = f^0(1 + \phi) \tag{3.74}$$

High pressures observed in the thermal plasmas result in mean free paths of few μm and hence, low Kn. In such low-Kn regimes involving a high degree of collisions, the success of this method depends upon utilizing accurate interaction potentials $\Phi_{ij}(r)$ to describe possible collisions between particles of different molecular structures and

charges. The interaction potential Φ_{ij} between particles i and j is dependent only upon the inter-particle distance r. For example, the Lennard-Jones (L-J) potential with the parameters combination (ϵ, σ) or (ϵ, r_m) is commonly used to describe neutral-neutral and ion-neutral interactions:

$$\Phi_{ij}^{LJ}(r) = 4\epsilon\left[\left(\frac{\sigma}{r}\right)^{12} - \left(\frac{\sigma}{r}\right)^{6}\right] = \epsilon\left[\left(\frac{r_m}{r}\right)^{12} - 2\left(\frac{r_m}{r}\right)^{6}\right] \tag{3.75}$$

Here, $r_m = 2^{1/6}\sigma$ is the position of the potential's minimum. The collisional term on the right hand side of (3.48) is expanded after substitution of (3.74) and accounting for the collisional dynamics.

The eventual outcome of the Chapman-Enskog method is that the transport properties are expressed in terms of ratios of determinants. The elements of these matrices $\mathbf{q}^{mp}$ are formed through an p^{th} order of successive approximations, where each additional approximation results in higher-order matrices [64, 65]:

$$\mathbf{q}_{ij}^{mp} = \sqrt{\frac{2\pi m_i}{kT_i}}\tilde{\mathbf{Q}}_{ij}^{mp} \tag{3.76}$$

In (3.76), both the indices i and j range from 1 to N_{sp} meaning that $\mathbf{q}^{mp}$ is a square matrix of order N_{sp}. Also, $\tilde{\mathbf{Q}}_{ij}^{mp}$ can be formulated for different transport properties as:

$$\tilde{\mathbf{Q}}_{ij}^{mp} = \begin{cases} \mathbf{Q}_{ij}^{mp} & \text{for viscosity,} \\ \mathbf{Q}_{ij}^{mp} - \frac{n_j\sqrt{m_j}}{n_i\sqrt{m_i}}\mathbf{Q}_{ii}^{mp}\delta_{m0}\delta_{p0} & \text{other properties} \end{cases} \tag{3.77}$$

where, $\mathbf{Q}_{ij}^{mp}$ is the summation over all species of suitable "bracket integrals" involving the tensor $\overline{\overline{W}}$ and Sonine polynomials S_n^m [65]:

$$\mathbf{Q}_{ij}^{mp} = \sum_{l=1}^{N_{sp}} n_i n_l \left\{\delta_{ij}\left[\overline{\overline{W}}_i S_n^m(W_i^2); \overline{\overline{W}}_i S_n^p(W_i^2)\right]_{il} + \delta_{jl}\left[\overline{\overline{W}}_i S_n^m(W_i^2); \overline{\overline{W}}_l S_n^p(W_l^2)\right]_{il}\right\} \tag{3.78}$$

where, W_i^2 is the magnitude of the vector $\vec{W}_i = (m_i/2kT_i)^{1/2}\vec{V}_i$. The tensor $\overline{\overline{W}}$ equals $\vec{W}_i\vec{W}_i - 1/3W_i^2\overline{\overline{I}}$ and $\vec{W}_i$ for viscosity and other properties respectively. $\overline{\overline{I}}$ is the identity tensor. Even though $p \to \infty$ theoretically, a third or fourth order approximation results in a rapid convergence of the determinant ratios. Each of the matrix elements $\mathbf{q}^{mp}$ is a

linear combination of Chapman-Cowling collision integrals $\Omega_{ij}^{(l,s)}$ which are defined by:

$$\Omega_{ij}^{(l,s)} = \left(\frac{kT_{ij}^*}{2\pi\mu_{ij}}\right)\int_0^\infty e^{-\gamma_{ij}^2}\gamma_{ij}^{2s+3}Q_{ij}^{(l)}\,d\gamma_{ij} \tag{3.79}$$

where, the reduced mass μ_{ij}, the effective temperature of collision T_{ij}^* and the dimensionless relative speed γ_{ij} are formulated respectively as:

$$\mu_{ij} = \frac{m_i m_j}{m_i + m_j},\ T_{ij}^* = \left[\frac{1}{m_i + m_j}\left(\frac{m_i}{T_j} + \frac{m_j}{T_i}\right)\right]^{-1},\ \gamma_{ij} = \left(\frac{\mu_{ij}g^2}{2kT_{ij}^*}\right)^{\frac{1}{2}} \tag{3.80}$$

The collision integrals $\Omega^{(l,s)}$ capture the collisional dynamics between particles through their relation to the integral collision cross section $Q^{(l)}(g)$:

$$Q_{ij}^{(l)}(g) = 2\pi\int_0^\infty \sigma(g,\chi)\left(1-\cos^l\chi\right)\sin\chi\,d\chi = 2\pi\int_0^\infty\left(1-\cos^l\chi\right)b\,db \tag{3.81}$$

where, $\sigma(g,\chi)$ is the differential cross-section depending upon the initial relative speed of colliding molecules g and deflection angle χ, b is the impact parameter. The following equation highlights the dependence of χ on the interaction potential Φ:

$$\chi = \pi - 2b\int_{r_{min}}^\infty \frac{dr}{r^2\sqrt{\left(1-\frac{b^2}{r^2}-\frac{2\Phi_{ij}(r)}{\mu_{ij}g^2}\right)}} \tag{3.82}$$

where, r_{min} is the distance of closest approach obtained by setting the denominator of the integrand to zero. Hence, the collision integrals can be obtained by numerically integrating (3.82), (3.81) and (3.79) for a suitable Φ_{ij} between species i and j. These integrals are highly non-linear and are observed to have several singularities which cause the numerical solution to diverge. Hence, the numerical method used to evaluate these integrals must efficiently capture the multiple singularities in order to obtain a convergent solution. The values (l, s) required in (3.79) depend on the desired order of approximation and in turn dictate the order of Sonine polynomials. The Sonine polynomials of order m and index n are defined as [65]:

$$S_n^m(x) = \sum_j \frac{(-1)^j(m+n)!}{(n+j)!(m-j)!j!}x^j \tag{3.83}$$

The index n is chosen to be 5/2 and 3/2 for viscosity and other properties respectively. In this thesis work, in order to obtain transport properties with high order of accuracy, collision integrals $\Omega^{(l,s)}$ are required upto the maximum values of $l_{max} = 3$ and $s_{max} = 5$. With the condition that $s \geq l$, 12 collision integral values are required for each combination of i and j.

Two of the most popular approaches considered in literature to determine $\mathbf{q}^{mp}$ and the transport properties belong to: (i) Devoto [66] and (ii) Rat *et al.* [22]. The two major assumptions in Devoto's approach are: (a) there is negligible effect of electron-heavy collisions on the distribution function of heavy species and (b) the change in perturbation to heavy species distribution function during electron-heavy collisions is small compared to the change in perturbation to electron distribution function. The consequences of these assumptions are: (a) the contribution of electron-heavy collision terms towards atomic and ionic transport properties are neglected and (b) the contribution of the change in heavy species perturbation term, during electron-heavy collisions, towards electron transport properties are neglected. In essence, Devoto's simplifications results in decoupling of the calculations for heavy particle and electron transport properties because the ratio of electron to heavy species masses is extremely small. However Rat and his co-workers claim that Devoto's assumptions are strictly valid for LTE plasma, while they fail for two-temperature plasmas because the summation of diffusion driving forces does not equal zero. As a consequence, the values of diffusion coefficients in argon plasma for $\theta = 2$ calculated using Devoto's approach are observed to be different from those of Rat's approach by around 30%. In this work, since LTE plasma is considered, Devoto's simplified approach is utilized and Rat's approach will be taken up in future work for general non-equilibrium plasmas.

Collision integral computation

(i) *Neutral-neutral and ion-neutral interactions*:

It is assumed in our work that a general potential of the form:

$$\Phi(r) = \epsilon f(\frac{r}{\sigma}) \tag{3.84}$$

is available to characterize the interaction between any two particles, the most prominent example being the Lennard-Jones potential in (3.75). One of the most general and complicated potentials which is capable of capturing the physics of several potentials is the Hulburt-Hirschfelder (H-H) potential [67], with its relevant parameters obtained from spectroscopic measurements. The success of numerical methods to obtain collision integrals depends upon their ability to resolve possible singularities and provide a converged solution for any complicated potential Φ [68]. The numerical integration for collision integrals is least cumbersome for the L-J potential. Recently, a phenomenological Lennard-Jones type potential has been suggested by Pirani *et al.* [69] to represent neutral-neutral and ion-neutral interactions:

$$\Phi(r) = \epsilon \left[\frac{m}{n(x) - m} \left(\frac{1}{x} \right)^{n(x)} - \frac{n(x)}{n(x) - m} \left(\frac{1}{x} \right)^{m} \right] \tag{3.85}$$

where, $x = r/r_m$, $m = 6$ for neutral-neutral interactions, $m = 4$ for ion-neutral interactions and $n(x) = \beta + 4x^2$. The parameter β depends on the softness s, which equals cubic root of the polarizability (α), of the colliding particles:

$$\beta = 6 + \frac{5}{s_1 + s_2} \tag{3.86}$$

For neutral-neutral interactions, the binding energy ϵ and equilibrium distance r_m in (3.85) are related to the polarizabilities of colliding partners using the correlations:

$$r_m = 1.767 \frac{\alpha_1^{1/3} + \alpha_2^{1/3}}{(\alpha_1 \alpha_2)^{0.095}}, \; \epsilon = 15.7 \frac{\alpha_1 \alpha_2}{\left[\sqrt{\frac{\alpha_1}{N_{eff,1}}} + \sqrt{\frac{\alpha_2}{N_{eff,2}}} \right]} \tag{3.87}$$

where N_{eff} is the effective number of electrons contributing to the polarization of the neutral species. For ion-neutral interactions, the correlations are:

$$r_m = 1.767 \frac{\alpha_i^{1/3} + \alpha_n^{1/3}}{(\alpha_i \alpha_n \left[1 + \frac{1}{\rho_d} \right])^{0.095}}, \; \epsilon = 5.2 \frac{z^2 \alpha_n}{r_m^4} \left[1 + \rho_d \right], \text{ with,} \tag{3.88}$$

$$\rho_d = \frac{\alpha_i}{z^2 \left[1 + \left(\frac{2\alpha_i}{\alpha_n} \right)^{\frac{2}{3}} \right] \sqrt{\alpha_n}}$$

where z is the ionic charge and the subscripts "i" and "n" denote the ion and neutral species respectively. The polarizability values of different species in this work are taken from literature. The collision integrals calculated using (3.85) have been demonstrated to provide extremely good agreement with the published data [70].

It is usually convenient to perform the numerical integration of the dimensionless forms of (3.82), (3.81) and (3.79). In order to non-dimensionalize these equations, the following dimensionless (starred) quantities are utilized:

$$r^* = \frac{r}{\sigma}, b^* = \frac{b}{\sigma}, \Phi^* = \frac{\Phi}{\epsilon}, T^* = \frac{kT}{\epsilon}, E^* = g^{*2} = \frac{1}{2}\frac{\mu g^2}{\epsilon} \tag{3.89}$$

The dimensionless cross section and collision integral are obtained by first dividing $Q^{(l)}$ and $\Omega^{(l,s)}$ by their values for rigid-sphere ($r.s.$) collisions respectively:

$$Q^{(l)*} = \frac{\left[Q^{(l)}\right]}{\left[Q^{(l)}\right]_{r.s}} = \left[1 - \frac{1+(-1)^l}{2(1+l)}\right]^{-1} \frac{Q^{(l)}}{\pi\sigma^2} \tag{3.90}$$

$$\Omega^{(l,s)*} = \frac{\left[\Omega^{(l,s)}\right]}{\left[\Omega^{(l,s)}\right]_{r.s}} = \frac{2}{(s+1)!}\left[1 - \frac{1+(-1)^l}{2(1+l)}\right]^{-1} \frac{\Omega^{(l,s)}\sqrt{\frac{2\pi\mu}{kT}}}{\pi\sigma^2} \tag{3.91}$$

Using the dimensionless variables in (3.89), we get the dimensionless right hand sides of the deflection angle:

$$\chi = \pi - 2b^* \int_{r_m^*}^{\infty} \frac{dr^*}{r^{*2}\sqrt{\left(1 - \frac{b^{*2}}{r^{*2}} - \frac{\Phi_{ij}^*(r^*)}{E^*}\right)}}, \tag{3.92}$$

integral cross section:

$$Q^{(l)*}(E^*) = 2\left[1 - \frac{1+(-1)^l}{2(1+l)}\right]^{-1} \int_0^{\infty} \left(1 - \cos^l\chi\right) b^*\, db^* \tag{3.93}$$

and collision integrals:

$$\Omega^{(l,s)*}(T^*) = \frac{1}{(s+1)!T^{*s+2}} \int_0^{\infty} e^{-\frac{E^*}{T^*}} E^{s+1} Q^{(l)*}(E^*)\, dE^* \tag{3.94}$$

In this work, the numerical procedure of Barker *et al.* [71] is followed to obtain collision

integrals in (3.94) for neutral-neutral and ion-neutral collisions. Then, the dimensional collision integrals $\overline{Q}^{(l,s)}$, required for the calculation of q^{mp} in (3.76), are given by:

$$\overline{Q}_{ij}^{(l,s)} = \pi\sigma^2\Omega_{ij}^{(l,s)*} \tag{3.95}$$

(ii) *Ion-parent neutral interactions*:

In the case of ion-neutral collisions, the contribution from charge-exchange processes needs to be added to the elastic cross sections. This contribution is especially significant for odd values of l and is negligible for the even values. The charge-exchange cross section depending on the relative speed g can be approximately written as [72]:

$$Q^{c.e.} = [A - B\ln g]^2 \tag{3.96}$$

where, A and B are constants obtained from experimental measurements. Substituting (3.96) into (3.95), we obtain the following analytical expression for the dimensional collision integral depending upon A, B and molecular weight of the gas M [72]:

$$\begin{aligned}\overline{Q}_{ij}^{(l,s)} = \frac{1}{\pi}\Big[A^2 - ABx + \left(\frac{Bx}{2}\right)^2 + \frac{B\zeta}{2}(Bx - 2A) + \frac{B^2}{4}\left(\frac{\pi^2}{6} - \sum_{n=1}^{s+1}\frac{1}{n^2} + \zeta^2\right) \\ + \frac{B}{2}\left[B(x+\zeta) - 2A\right]\ln\frac{T}{M} + \left(\frac{B}{2}\ln\frac{T}{M}\right)^2\Big]\end{aligned} \tag{3.97}$$

where, $x = \ln(4\hat{R})$ with $\hat{R}$ being the universal gas constant, $\zeta = \sum_{n=1}^{s+1}(1/n) - \bar{\gamma}$ and $\bar{\gamma} = 0.5772$ is the Euler's constant.

(iii) *Charged-charged interactions*:

The cross sections for charged-charged collisions are obtained by assuming shielded-Coulomb (S-C) potential, depending on the particle charges Z and Debye length λ_D, for small-angle collisions:

$$\Phi_{ij}^{SC}(r) = Z_i Z_j \frac{e^2}{r} e^{-\frac{r}{\lambda_D}} \tag{3.98}$$

and the bare Coulomb potential for close collisions. The cross section expressions for l

= 1, 2 and 3 are derived from substituting (3.98) into (3.81) as [72]:

$$Q^{(1)} = 4\pi \left(\frac{b_0}{y}\right)^2 \left[\ln\left(\frac{2y\lambda_D}{b_0}\right) - \frac{1}{2} - \bar{\gamma}\right], \tag{3.99}$$

$$Q^{(2)} = 8\pi \left(\frac{b_0}{y}\right)^2 \left[\ln\left(\frac{2y\lambda_D}{b_0}\right) - 1 - \bar{\gamma}\right], \tag{3.100}$$

$$Q^{(3)} = 12\pi \left(\frac{b_0}{y}\right)^2 \left[\ln\left(\frac{2y\lambda_D}{b_0}\right) - \frac{7}{6} - \bar{\gamma}\right], \tag{3.101}$$

where, $y = \gamma^2$ and the average closest impact parameter $b_0 = Z_i Z_j e^2/(2kT)$. Substituting (3.99)-(3.101) into (3.95), the analytical expressions of collision integrals for the afore-mentioned l values are obtained as [72]:

$$\overline{Q}^{(1,s)} = \frac{4\pi}{s(s+1)} b_0^2 \left[\ln\Lambda - \frac{1}{2} - 2\bar{\gamma} + \psi(s)\right], \tag{3.102}$$

$$\overline{Q}^{(2,s)} = \frac{12\pi}{s(s+1)} b_0^2 \left[\ln\Lambda - 1 - 2\bar{\gamma} + \psi(s)\right], \tag{3.103}$$

$$\overline{Q}^{(3,s)} = \frac{12\pi}{s(s+1)} b_0^2 \left[\ln\Lambda - \frac{7}{6} - 2\bar{\gamma} + \psi(s)\right], \tag{3.104}$$

where, $\Lambda = 2\ \lambda_D/b_0$, $\psi(1) = 0$ and $\psi(s \neq 1) = \sum_{n=1}^{s-1}(1/n)$.

(iv) *Electron-neutral interactions*:

Unlike the previous cases, a well-defined potential for electron-neutral interactions is not available for several neutral particles. For certain monatomic and diatomic particles, diatomic nitrogen and oxygen for example, differential elastic cross sections are available which can be substituted into the first equality in (3.81) to obtain the integral cross section and the collision integrals. However, we use the polynomial fits provided by Laricchiuta *et al.* [73] to calculate collision integrals for electron-nitrogen and electron-oxygen interactions. For monatomic metallic atoms in this work, differential cross sections are not reported in the literature. For these atoms, we use the elastic momentum cross sections $Q^{(1)}$ to obtain $\overline{Q}^{(1,s)}$ from (3.95). The other collision integrals $\overline{Q}^{(2,s)}$ and $\overline{Q}^{(3,s)}$ are obtained from (3.95) by using the isotropic diffusion approximation: $Q^{(2)} = \frac{2}{3}Q^{(1)}$ and $Q^{(3)} = Q^{(1)}$ respectively.

There are some common features observable in the formulation of each transport property considered in this chapter. As mentioned earlier, the Chapman-Enskog method results in each transport property being formulated as the ratio of two determinants. The elements of the denominator matrix are composed primarily of $\hat{\mathbf{q}}_{ij}$ or $\mathbf{q}_{ij}$ depending upon the type of property. The numerator matrix is the same as the denominator matrix except for additional row and column elements, which are different for different properties. The additional elements in the final column and final row of the numerator matrix are column and row vectors of size N_{sp} respectively. Bold letters used for heavy-species related properties, $\hat{\mathbf{q}}$ or $\mathbf{q}$, indicate that each element is a matrix of size $N_{sp} \times N_{sp}$. For electron properties, plain lettered q are used to indicate a scalar. The expressions for $\hat{\mathbf{q}}$, $\mathbf{q}$ and q for different superscripts (m, p) [66, 74] are provided in Appendix B. The matrices are observed to possess numbers with widely different scales and hence, an accurate algorithm is required to calculate the determinants. In this work, the determinants are calculated using the LU-decomposition routine of Intel's MKL software [75].

Dynamic viscosity

Kinetic theory predicts that the dynamic viscosity for a simple dilute gas is inversely proportional to the collision integral $\bar{Q}^{(2,2)}$. For this reason, the integral cross section (3.81) corresponding to $l = 2$ is sometimes termed the viscosity cross section in the literature. In the case of a gas mixture, the second order approximation to dynamic viscosity $(kg/m/s)$ is given as:

$$[\eta]_2 = -\frac{5(2\pi kT)^{\frac{1}{2}}}{2|\hat{\mathbf{q}}|} \begin{vmatrix} \hat{\mathbf{q}}_{ij}^{00} & \hat{\mathbf{q}}_{ij}^{01} & n_i\sqrt{m_i} \\ \hat{\mathbf{q}}_{ij}^{10} & \hat{\mathbf{q}}_{ij}^{11} & 0 \\ n_j & 0 & 0 \end{vmatrix} \tag{3.105}$$

where, the determinant in the denominator $|\hat{\mathbf{q}}|$ is written as:

$$|\hat{\mathbf{q}}| = \begin{vmatrix} \hat{\mathbf{q}}_{ij}^{00} & \hat{\mathbf{q}}_{ij}^{01} \\ \hat{\mathbf{q}}_{ij}^{10} & \hat{\mathbf{q}}_{ij}^{11} \end{vmatrix} \tag{3.106}$$

Diffusion coefficients

In the case of a two-species mixture, the molecular flux of each species is proportional to the gradient in its number density with the binary diffusion coefficient $\mathscr{D}_{ij}$ being the proportionality constant. For a first order approximation, $\mathscr{D}_{ij}$ is derived as [66]:

$$\mathscr{D}_{ij} = \frac{3}{16N}\sqrt{\frac{2\pi kT}{\mu_{ij}}}\frac{1}{\bar{Q}_{ij}^{(1,1)}} \tag{3.107}$$

$\mathscr{D}_{ij}$ values are required for the calculation of reactive thermal conductivity κ_{reac} formulated by Butler and Brokaw [76]. From (3.107), it can be seen that the binary diffusion coefficient is inversely proportional to the collision integral $\bar{Q}^{(1,1)}$. For this reason, the integral cross section (3.81) corresponding to $l = 1$ is sometimes termed the diffusion cross section in the literature. Also, $\mathscr{D}_{ij}$ between the two species i and j is always positive. However, there are multiple species in the gas mixtures considered in this work. Hence, diffusion coefficients between any two species i and j in the presence of other species need to be determined. The diffusion of one species relative to the other, in the presence of gradients in number densities of other species, gradients in pressure and external forces, is captured by ordinary diffusion coefficients D_{ij}. For the entire gas mixture, $N_{sp} \times (N_{sp} - 1)$ independent third-order accurate diffusion coefficients D_{ij} for heavy-species were calculated using [66]:

$$[D_{ij}]_3 = -\frac{3\rho n_i}{2Nm_j|\mathbf{q}|}\left(\frac{2\pi kT}{m_i}\right)^{\frac{1}{2}}\begin{vmatrix} \mathbf{q}_{ij}^{00} & \mathbf{q}_{ij}^{01} & \mathbf{q}_{ij}^{02} & (\delta_{hj} - \delta_{hi}) \\ \mathbf{q}_{ij}^{10} & \mathbf{q}_{ij}^{11} & \mathbf{q}_{ij}^{12} & 0 \\ \mathbf{q}_{ij}^{20} & \mathbf{q}_{ij}^{21} & \mathbf{q}_{ij}^{22} & 0 \\ \delta_{ki} & 0 & 0 & 0 \end{vmatrix} \tag{3.108}$$

where the $|\mathbf{q}|$ in the denominator is the determinant of the matrix:

$$|\mathbf{q}| = \begin{vmatrix} \mathbf{q}_{ij}^{00} & \mathbf{q}_{ij}^{01} & \mathbf{q}_{ij}^{02} \\ \mathbf{q}_{ij}^{10} & \mathbf{q}_{ij}^{11} & \mathbf{q}_{ij}^{12} \\ \mathbf{q}_{ij}^{20} & \mathbf{q}_{ij}^{21} & \mathbf{q}_{ij}^{22} \end{vmatrix} \tag{3.109}$$

and δ_{ij} is the Kroenecker delta function which equals 1 when $i = j$ and equals 0 otherwise. Likewise, $N_{sp} - 1$ third-order accurate thermal diffusion coefficients D_i^T capturing diffusion in the presence of temperature gradients were calculated using:

$$\left[D_i^T\right]_3 = \frac{15 n_i}{4} \frac{(2\pi k T)^{\frac{1}{2}}}{|\mathbf{q}|} \begin{vmatrix} \mathbf{q}_{ij}^{00} & \mathbf{q}_{ij}^{01} & \mathbf{q}_{ij}^{02} & 0 \\ \mathbf{q}_{ij}^{10} & \mathbf{q}_{ij}^{11} & \mathbf{q}_{ij}^{12} & n_h \\ \mathbf{q}_{ij}^{20} & \mathbf{q}_{ij}^{21} & \mathbf{q}_{ij}^{22} & 0 \\ \delta_{ki} & 0 & 0 & 0 \end{vmatrix} \tag{3.110}$$

For electrons, simplified expressions for the diffusions coefficients are available from Devoto's work [74]. The third-order accurate ordinary diffusion coefficient is separately calculated as:

$$[D_{ee}]_3 = \frac{3\rho n_i}{2N m_e |q|} \left(\frac{2\pi k T}{m_e}\right)^{\frac{1}{2}} \begin{vmatrix} q^{22} & q^{23} \\ q^{32} & q^{33} \end{vmatrix} \tag{3.111}$$

while the third-order accurate thermal diffusion coefficient is obtained from:

$$\left[D_e^T\right]_3 = \frac{15 n_i}{4} \frac{(2\pi k T)^{\frac{1}{2}}}{|q|} \begin{vmatrix} q^{12} & q^{13} \\ q^{32} & q^{33} \end{vmatrix} \tag{3.112}$$

where the $|q|$ in the denominator is the determinant of the matrix:

$$|q| = \begin{vmatrix} q^{00} & q^{01} & q^{02} \\ q^{10} & q^{11} & q^{12} \\ q^{20} & q^{21} & q^{22} \end{vmatrix} \tag{3.113}$$

In a thermal plasma, two types of electric field need to be accounted for in the calculation of D_{ij} and D_i^T: (a) the externally applied electric field and (b) the electric field generated by charge-separation because the electrons diffuse faster than the ions. Accounting for these electric fields results in suitable ambipolar corrections being added to: D_{ij} to obtain the ambipolar diffusion coefficients D_{ij}^a [77]:

$$D_{ij}^a = D_{ij} + \frac{\alpha_i}{\beta} \sum_{l=1}^{N_{sp}} Z_l D_{lj} \tag{3.114}$$

and D_i^T to obtain the ambipolar thermal diffusion coefficients D_i^{Ta} [77]:

$$D_i^{Ta} = D_i^T + \frac{\alpha_i m_i}{\beta} \sum_{l=1}^{N_{sp}} \frac{Z_l D_l^T}{m_l} \tag{3.115}$$

where, α_i and β are related to D_{ij} through:

$$\alpha_i = \sum_{j=1}^{N_{sp}} n_j m_j Z_j D_{ij}, \ \beta = -\sum_{i,j=1}^{N_{sp}} Z_i Z_j n_j m_j D_{ij} \tag{3.116}$$

The ordinary diffusion coefficients D_{ij} are required for the calculation of electrical conductivity σ. In the case of non-equilibrium two-temperature plasma, the LTE formulation of Butler and Brokaw [76] for κ_{reac} is not applicable. The alternative formulation which depends upon the ambipolar diffusion coefficients [78, 79] will be considered in future work.

Thermal conductivity

The total thermal conductivity is the sum of four different contributions: (a) from heavy-species κ_h, (b) from electrons κ_e, (c) from reactions κ_{reac} and (d) from internal degrees of freedom κ_{int}:

$$\kappa_{tot} = \kappa_h + \kappa_e + \kappa_{reac} + \kappa_{int} \tag{3.117}$$

In this work, the contribution from the vibrational and electronic modes κ_{int} is not calculated and assumed to be negligible compared to the other contributions. The third-order accurate heavy-species thermal conductivity is given as [66]:

$$[\kappa_h]_3 = -\frac{75k}{8} \frac{(2\pi kT)^{\frac{1}{2}}}{|\mathbf{q}|} \begin{vmatrix} \mathbf{q}_{ij}^{00} & \mathbf{q}_{ij}^{01} & \mathbf{q}_{ij}^{02} & 0 \\ \mathbf{q}_{ij}^{10} & \mathbf{q}_{ij}^{11} & \mathbf{q}_{ij}^{12} & n_i \\ \mathbf{q}_{ij}^{20} & \mathbf{q}_{ij}^{21} & \mathbf{q}_{ij}^{22} & 0 \\ 0 & \frac{n_j}{\sqrt{m_j}} & 0 & 0 \end{vmatrix} \tag{3.118}$$

while the third-order accurate electron thermal conductivity is given as [74]

$$[\kappa_e]_3 = \frac{75 n_e^2 k}{8} \left(\frac{2\pi k T}{m_e} \right)^{\frac{1}{2}} \frac{q^{22}}{q^{11} q^{22} - (q^{12})^2} \tag{3.119}$$

The most important contribution towards thermal conductivity pertains to the contribution from reactions. The species considered in the gas mixture participate in several dissociation reactions at temperatures lower than 10,000 K and ionization reactions at higher temperatures. The reactive thermal conductivity κ_{reac} is primarily responsible for several peaks in the total thermal conductivity κ_{tot}. The first step in the calculation of κ_{reac} is to set-up all possible dissociation and ionization reactions involving the different species in the gas mixture. If there are N_{sp} species and N_{elem} dependent species which can be used to construct the other independent species, $N_{reac} = N_{sp} - N_{elem}$ independent reactions can be set-up. A reaction "i" can be exothermic or endothermic, with an associated net enthalpy per particle Δh_i (J) depending on the enthalpies of its products and reactants. The enthalpy per particle for any species "j" can be determined by multiplying its specific enthalpy h_j by the factor ρ/n_j. Also, the particle flux $(m^{-1}s^{-1}K^{-1})$ resulting from a temperature gradient and hence a mole fraction gradient depends upon the ambipolar diffusion coefficients and can be written as [78]:

$$\Psi_i = \frac{N^2}{\rho} \sum_{j=1}^{N_{sp}} m_j D_{ij}^a \nabla x_j \tag{3.120}$$

The total heat flux resulting from the reactions is obtained by tallying up the product of the net reaction enthalpy per particle and the particle flux of independent species:

$$\mathbf{q}_{reac} = \sum_{i=1}^{N_{reac}} \Delta h_i \Psi_i = \left(\sum_{i=1}^{N_{reac}} \Delta h_i \frac{N^2}{\rho} \sum_{j=1}^{N_{sp}} m_j D_{ij}^a \frac{\partial x_j}{\partial T} \right) \nabla T = \kappa_{reac} \nabla T \tag{3.121}$$

where the term within the parentheses in (3.121) is the reactive thermal conductivity κ_{reac}. The mole fraction derivative with respect to the temperature $\frac{\partial x_j}{\partial T}$ can be determined using simple second-order finite difference schemes.

Additionally, beginning from an expression similar to (3.121), Butler and Brokaw [76] provide an alternate derivation for a gas mixture with $\mu = N_{sp}$ species and $\nu = N_{reac}$

reactions. The ν independent species must be on the left hand side of ν reactions with the N_{elem} dependent species on the right hand side. The matrix $\mathbf{n}$ of size $\nu \times N_{elem}$ stores the stoichiometric coefficients of each reaction. Dealing with molar flux rather than particle flux, κ_{reac} is derived in the usual form of ratio of two determinants:

$$\kappa_{reac} = -\frac{1}{\hat{R}T^2|\mathbf{A}|}\begin{vmatrix} 0 & \Delta H_1 & ..... & \Delta H_\nu \\ \Delta H_1 & A_{11} & ..... & A_{1\nu} \\ . & . & & . \\ . & . & & . \\ \Delta H_\nu & A_{\nu 1} & ..... & A_{\nu\nu} \end{vmatrix} \tag{3.122}$$

where, ΔH_i is the net reaction enthalpy of reaction "i" in J/mol obtained by multiplying Δh_i with the Avogadro number. The $\nu \times \nu$ size matrix $\mathbf{A}$ in the denominator of (3.122) can be written as:

$$|\mathbf{A}| = \begin{vmatrix} A_{11} & ..... & A_{1\nu} \\ . & & . \\ . & & . \\ A_{\nu 1} & ..... & A_{\nu\nu} \end{vmatrix} \tag{3.123}$$

The off-diagonal elements of the symmetric matrix $\mathbf{A}$ are given as:

$$A_{ik} = \sum_{j=\nu+1}^{\mu-1}\sum_{m=j+1}^{\mu} \Delta_{mj}\frac{(n_{ij}x_m - n_{im}x_j)(n_{kj}x_m - n_{km}x_j)}{x_j x_m} + \sum_{j=\nu+1}^{\mu}\sum_{p=1}^{\nu} n_{ij}n_{kj}\Delta_{pj}\frac{x_p}{x_j}$$
$$+ \sum_{j=\nu+1}^{\mu}(n_{kj}\Delta_{ij} + n_{ij}\Delta_{kj}) - \Delta_{ik};\ i,k = 1,2,.....\nu, \tag{3.124}$$

while the diagonal elements of $\mathbf{A}$ are given as:

$$A_{kk} = \sum_{j=\nu+1}^{\mu-1}\sum_{m=j+1}^{\mu} \Delta_{mj}\frac{(n_{ij}x_m - n_{im}x_j)^2}{x_j x_m} + \sum_{j=\nu+1}^{\mu}\sum_{\substack{p=1 \\ p\neq k}}^{\nu} n_{kj}^2\Delta_{pj}\frac{x_p}{x_j} + \sum_{\substack{p=1 \\ p\neq k}}^{\nu}\Delta_{pk}\frac{x_p}{x_k}$$
$$+ \sum_{j=\nu+1}^{\mu}\Delta_{kj}\frac{(x_j + n_{kj}x_k)^2}{x_j x_k};\ k = 1,2,.....\nu. \tag{3.125}$$

In (3.124) and (3.125), $\Delta_{ij} = \hat{R}T/\mathscr{D}_{ij}p$ and n_{ij} are the elements of the stoichiometric

coefficient matrix **n**. In the above derivation, the independent species are given the indices from 1 to ν while the dependent species are given the indices from $\nu+1$ to μ. In this work, κ_{reac} is calculated using the formula of Butler and Brokaw in (3.122) rather than 3.121.

Electrical conductivity

The electrical conductivity σ for partially ionized gas mixtures is related to the ordinary diffusion coefficients D_{ij} through [77]:

$$\sigma = \frac{e^2 N}{\rho k T} \sum_{j=1}^{N_{sp}-1} \left(n_j m_j Z_j D_{ej} - Z_j \sum_{j=1}^{N_{sp}} n_i m_i Z_i D_{ji} \right) \tag{3.126}$$

However, the second term in (3.126) is found to be negligible compared to the first for most gas mixtures and hence, to a good approximation, σ is simplified to be:

$$\sigma \approx \frac{e^2 N}{\rho k T} \sum_{j=1}^{N_{sp}-1} n_j m_j Z_j D_{ej} \tag{3.127}$$

Combined diffusion coefficients

In this work, we are interested in calculating the diffusion coefficients for general air-metal vapor mixtures. In the previous section on diffusion coefficients, we have seen that there are totally $N_{sp} \times N_{sp}$ ordinary diffusion coefficients and N_{sp} thermal diffusion coefficients for an equilibrium gas mixture with N_{sp} species. However, the CFD solver is written in terms of air and metal vapor as the components using a "one-fluid" formulation. Hence, the diffusion coefficients corresponding to diffusion of two components or gases relative to each other, rather than diffusion relative to individual species, are desired. Such diffusion coefficients have the desired characteristic of capturing complex mixing and de-mixing effects [80] in the regions close to the plasma boundaries. Murphy [77] has derived diffusion coefficients for diffusion of two non-reacting gases relative to each other in the presence of (a) mole fraction gradients, (b) pressure gradients and (c) temperature gradients. Hence, the problem is reduced to the determination of a

"combined" diffusion coefficient for each of the afore-mentioned gradients and therefore, three in total. In general, the diffusion coefficients due to mole fraction gradients are significantly higher than those due to pressure or temperature gradients. An important requirement for using Murphy's approach is that the two gases A and B must not share any species or element and hence, metal oxides must not be included in the list of species for either gas. This requirement is easily met for air-metal vapor mixtures, since the mole fractions of metal oxides are usually negligible above the boiling point of the metal. However, this requirement essentially precludes the use of combined diffusion coefficients when plastic vapors are also included in the gas mixture because some of the species with high mole fractions belong to both air and plastic vapor.

A slightly different notation compared to Murphy's is employed in this work: Air is labeled "gas A" with its species given indices from 1 to p, metal vapor is labeled "gas B" with its species given indices from $p+1$ to $N_{sp}-1$ and electrons have the index N_{sp}. The diffusion mass flux of gas A relative to gas B including the three different gradients is defined as [77]:

$$\overline{\boldsymbol{J}_A} = \overline{m_A}\frac{N^2}{\rho}\overline{m_B}\left(\overline{D^x_{AB}}\nabla\overline{x_B} + \overline{D^p_{AB}}\nabla\ln p\right) - \overline{D^T_{AB}}\nabla\ln T \tag{3.128}$$

where, the bar notation alludes to a gas-based rather than a species-based variable. The combined diffusion coefficients owing to mole fraction, pressure and temperature gradients in (3.128) are expressed respectively as:

$$\overline{D^x_{AB}} = \frac{1}{\overline{m_B}}\sum_{i=1}^{p} s_i \sum_{j=1}^{N_{sp}} m_j D^a_{ij}\frac{\partial x_j}{\partial\overline{x_B}}, \tag{3.129}$$

$$\overline{D^p_{AB}} = \frac{1}{\overline{m_B}}\sum_{i=1}^{p} s_i \sum_{j=1}^{N_{sp}} m_j D^a_{ij}\left(x_j - \frac{\rho_j}{\rho} + p\frac{\partial x_j}{\partial p}\right), \tag{3.130}$$

$$\overline{D^T_{AB}} = \overline{m_A}\sum_{i=1}^{p} s_i \left(\frac{D^{Ta}_i}{m_i} - \frac{N^2}{\rho}\sum_{j=1}^{N_{sp}} m_j D^a_{ij} T\frac{\partial x_j}{\partial T}\right) \tag{3.131}$$

where, the stoichiometric coefficients s_i are defined as:

$$
\begin{aligned}
s_i &= b_i \frac{\sum_{k=1}^{p} x_k}{\sum_{k=1}^{p} b_k x_k}, \ 1 \le i \le p, \\
s_i &= b_i \frac{\sum_{k=p+1}^{N_{sp}-1} x_k}{\sum_{k=p+1}^{N_{sp}-1} b_k x_k}, \ p+1 \le i \le N_{sp}-1, \\
s_i &= 0, \ i = N_{sp}
\end{aligned}
\tag{3.132}
$$

and the gas-averaged mole fraction variables $\overline{x_A}$ and $\overline{x_B}$ can be calculated from:

$$
\overline{x_A} = \sum_{k=1}^{p} (1 + Z_k)\, x_k, \ \overline{x_B} = \sum_{k=p+1}^{N_{sp}-1} (1 + Z_k)\, x_k = 1 - \overline{x_A}, \tag{3.133}
$$

while the gas-averaged mass variables $\overline{m_A}$ and $\overline{m_B}$ can be calculated from:

$$
\overline{m_A} = \frac{\sum_{k=1}^{p} (m_k x_k + m_e Z_k x_k)}{\sum_{k=1}^{p} x_k}, \ \overline{m_B} = \frac{\sum_{k=p+1}^{N_{sp}-1} (m_k x_k + m_e Z_k x_k)}{\sum_{k=p+1}^{N_{sp}-1} x_k}, \tag{3.134}
$$

Also, b_i in (3.132) represents the number of atoms in the molecular species "i", with a value of 1 and 2 for monatomic and diatomic species respectively.

In the case of two-temperature plasmas, recently published data [81, 82] indicate that the diffusion coefficients calculated using the methodology of Rat [22] have significant differences compared to those from the methodology of Devoto [66, 72, 74]. The methodology of Rat will be implemented for the two-temperature plasmas in the future work.

3.6 Composition from finite-rate kinetics

The previous sections dealt with calculation of properties, including breakdown fields, assuming chemical equilibrium. However, during dielectric recovery in a realistic LVCB, a temperature decay occurs post-CZ. With the contact gap center-line temperatures expected to be above 6,000 K at the instant of TRV emergence and assuming that a successful thermal interruption has occurred, significant deviations from chemical equilibrium are expected owing to finite-rate kinetics. In this thesis, we intend to quantify the deviations of breakdown fields using finite-rate chemical compositions from those obtained using chemical equilibrium. The breakdown field comparisons for air-metal vapor mixtures will be presented while those for air-metal-plastic vapor mixtures will be taken up in future work.

Analysis of a decaying arc around CZ including finite-rate kinetics has been performed exclusively for SF_6, first by Brand and Kopainsky [8] and later by Gleizes and his co-workers [83, 84]. In their analysis, Brand and Kopainsky provided the following expression for change in species number densities with time, given a temperature decay with time $T(t)$ from the fluid dynamic solution of mass, momentum and energy equations:

$$\frac{\partial n_i}{\partial t} = \sum_k \Gamma_{ik} - \frac{n_i}{p} kT \sum_{i,k} \Gamma_{ik} - \frac{n_i}{T} \frac{\partial T}{\partial t}, \ , i = 1, ...N_{sp} \tag{3.135}$$

where, Γ_{ik} represents the net generation of species "i" from reaction "k". The first term on the right-hand side of equation (3.135) represents the total generation of species "i" arising from all the reactions involving the species "i" and can be formulated as:

$$\sum_k \Gamma_{ik} = Q_i - L_i n_i, \tag{3.136}$$

Q_i and L_i are the rates of formation and decay of species "i". A decay time scale for the species, τ_i, can be derived from L_i as: $\tau_i = 1/L_i$. The second term represents the correction term for pressure increase owing to net generation of particles, while the third term denotes the particle generation owing to a temperature decay. With S, F and E^- being the elements in an SF_6 plasma, three conservation conditions of (i) electro-neutrality, (ii) atomic nucleus and (iii) total number density need to be satisfied. An important assumption implicit in this analysis is that the pressure remains constant

during the entire duration of temperature decay, which is valid for conditions post-CZ. Gleizes *et al.* [83] solved equation (3.135) for species number densities corresponding to a temperature decay from 12,000 K to 3,000 K. Some of the simplifying assumptions include: (a) Homogeneous and ideal gas plasma, (b) Maxwellian EEPF for all species, (c) kinetic equilibrium, meaning $T_h(t) = T_e(t) = T(t)$ obtained from the fluid flow solver and (d) No recovery voltage is applied during the temperature decay. It is worth noting that several different cooling rates are possible for any given temperature decay and hence, Gleizes considered realistic cooling rates of $5{\times}10^8 K/s$, $10^8 K/s$ and $10^7 K/s$ at different intervals of temperature decay. The effect of pressure on the variations in number density were studied for the cooling rate of $10^8 K/s$ at pressures $p = 1,\ 4\ atm$. Two main conclusions from Gleizes *et al.* [83] regarding departures of electron number densities from equilibrium were: (i) Decreasing the cooling rate results in a reduction of departures from equilibrium and (ii) for the cooling rate of $10^8 K/s$, increasing the pressure from $p = 1\ atm$ to $p = 4\ atm$ results in negligible deviations from equilibrium.

In this work, we employ the decaying arc kinetic analysis for atmospheric pressure air-metal vapor mixtures, after relaxing certain assumptions mentioned earlier. These include: (a) a constant recovery voltage appearing instantaneously at time $t = 0$ and (b) a general non-Maxwellian EEPF for electrons. We compare the breakdown fields, at different time instants of the temperature decay, based upon the species composition corresponding to: (i) chemical equilibrium, (ii) finite-rate kinetics assuming Maxwellian EEPF for electrons with $T_e = T$ and (iii) finite-rate kinetics assuming non-Maxwellian EEPF for electrons with $T_e \geq T$. The distinction between (ii) and (iii) is important since the non-Maxwellian EEPF is a direct consequence of the TRV post-CZ. Initially, numerical integration of equations (3.135) was performed using the CHEMEQ [85] solver. However, the species number densities were observed to be unstable resulting in violation of several conservation conditions. Hence, a revised kinetics solver based on the improved CHEMEQ2 method [17], with smoother integration characteristics and acceptable conservation condition tolerances, was developed for integrating the system of equations (3.135). This analysis is expected to quantify the sum total of all possible non-equilibrium effects on the breakdown fields, especially with the CFD and kinetics solvers being "stand-alone" or non-interacting pieces of code.

3.7 Methodology for dielectric breakdown prediction

Based on the experimental observations, dielectric breakdown post-CZ in a circuit breaker is a complex stochastic process involving an initial streamer formation and a final spark breakdown. As mentioned earlier, tracking the nanosecond time-scale streamer leading to a spark breakdown in a realistic circuit breaker geometry is computationally prohibitive. Additionally, streamer tracking would require an elaborate approach involving species-conservation equations for individual species. This entails a complete revision of the current CFD solver, which is possible for an air-metal vapor mixture with less than 50 species but impossible for an air-metal-plastic vapor mixture with greater than 100 species. Henceforth, a simplified methodology is required for a breakdown prediction. In this thesis, we characterize dielectric breakdown by a successful channel formation between the metallic electrodes across which TRV appears, without necessarily characterizing the channel as either a streamer or leader.

In order to clearly distinguish between thermal and dielectric breakdown, experiments can be set-up to introduce a delay time of a few μs between arc extinction and appearance of the TRV. However, in reality, the TRV appears almost instantaneously and hence, a clear distinction between a thermal and dielectric breakdown is not possible. In this work, we are interested in predicting dielectric breakdown in circuit breakers, for which both experimental data and input data from its counterpart CFD simulation are available. The kinetics solver utilizes the input CFD data to assess the probability of channel formation along different paths and a breakdown is predicted upon a successful channel formation. Then, the numerical prediction is compared with the available experimental results. As of date, experimental data and its corresponding CFD simulation data are available for a simplified geometry filled with an air-metal vapor mixture. The details regarding breakdown prediction for air-metal vapor mixtures are provided in chapter 7. Testing of the kinetics solver for general air-metal-plastic vapor mixtures will commence in the future upon obtaining relevant experimental and CFD data.

Chapter 4

Thermodynamic, transport and dielectric properties of compressed air

4.1 Dielectric fluid in an LVCB

During a normal operation of the circuit breaker, the space within the designed geometry is filled with a dielectric fluid. Some of the most desired characteristics for the dielectric fluid include: (a) greater ability to cool the primary arc with a convective cross-flow and (b) a high dielectric withstand capability at temperatures and voltages observed post-CZ. The latter property is extremely crucial since the high-temperature gas is susceptible to dielectric breakdown during the appearance of the TRV post-CZ. Electronegative gases, air and SF_6 for example, are highly favored as the gaseous medium in a circuit breaker owing to their ability to form anions by quenching excess electrons from the highly ionized state. The highly electronegative SF_6 gas is commonly used for high-voltage circuit breaker applications where the TRV ranges between several hundred to a few thousand kV. Even though SF_6 gas could be employed as the medium for low-voltage circuit breaker applications with a TRV of the order of a few hundred volts, weakly electronegative air is preferable since SF_6 gas has an extremely high global-warming potential (GWP).

In this chapter, we first present our results for the thermodynamic and transport properties of dry air (79% N_2, 21% O_2) at different values of pressure. Subsequently, we provide our results for the electron-swarm properties and dielectric breakdown fields at different temperatures and pressures. For thermodynamic and transport properties, we provide comparison of our results with those from Cressault [86]. In the case of electron-swarm parameters and breakdown fields, published data from Dutton [87] and Tanaka [46] are used for comparison respectively.

4.2 Equilibrium composition of compressed air

The LTE thermodynamic and transport properties depend upon the equilibrium species composition. Hence, greater agreement with properties results from published data serves as a validation for the species composition calculations. An LTE plasma com-

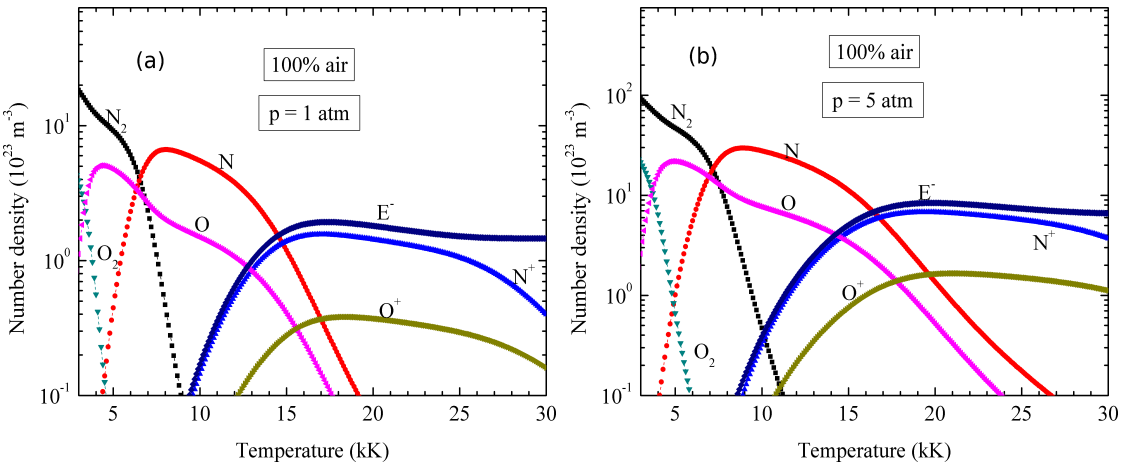

Figure 4.1: The variation of different species number densities with temperature for air at (a) p = 1 *atm* and (b) p = 5 *atm*.

position solver has been written for general air-copper mixtures of different air mole fractions in the range $x_{air} = 0$ (100% Cu) to $x_{air} = 1$ (100% air) with increments of 0.05. The list of species included for the composition calculations and their ground-state energies are provided in Appendix C. The species with the highest mole fractions for air at p = 1 *atm* and p = 5 *atm* are shown in figure 4.1(a) and (b) respectively.

Certain qualitative features can be deduced. Firstly, for both pressures, monatomic oxygen is first generated by dissociation of O_2 and NO, followed by the dissociation of N_2 which produces monatomic nitrogen. The monatomic nitrogen and oxygen then undergo ionization reactions at higher temperatures to form N^+ and O^+ respectively. Secondly, consider the intersection points of (a) N_2 and N curves and (b) N and N^+ curves for both pressures. It can be straight-forwardly observed that the intersection points for both (a) and (b) are shifted to the right for p = 5 atm compared to p = 1 atm. This means that the temperature ranges of dissociation and ionization reactions increase with pressure and the rightward shifts of dissociation and ionization peaks are clearly visible in specific heat (section 4.3) and thermal conductivity profiles (section 4.4).

4.3 Thermodynamic properties of compressed air

The most important thermodynamic properties for any gas mixture are density (ρ), total specific enthalpy (h), and specific heat at constant pressure (C_p). The "total" in enthalpy indicates sum of the contributions from heavy-species and electrons. The distinction between the two contributions becomes especially important while dealing with specific heats of two-temperature plasmas [88]. From (3.72), we can observe that the accuracy of C_p calculation depends upon the accuracies of both h and ρ. Hence, for brevity, the plot for specific heat variation with temperature for different pressures is provided in figure 4.2 instead of the corresponding density and enthalpy variations. The direction of the arrow in all figures of this chapter indicates the direction of increasing pressure p unless otherwise mentioned. The most interesting aspect with regard to specific heat at a given pressure is the presence of several peaks at different temperatures. Specifically, in figure 4.2, there are four different peaks each increasing in magnitude compared to the previous peak. The peaks at atmospheric pressure pertain to - (a) dissociation of diatomic oxygen at around 3,500 K, (b) dissociation of diatomic nitrogen at around 7,000 K, (c) first ionization of atomic oxygen and nitrogen at around 15,000 K, and (d) second ionization of atomic oxygen and nitrogen at around 30,000 K. As pressure increases, the magnitude of each peak decreases owing to lower specific enthalpies for a given temperature at higher pressures. Also, with an increase in pressure,

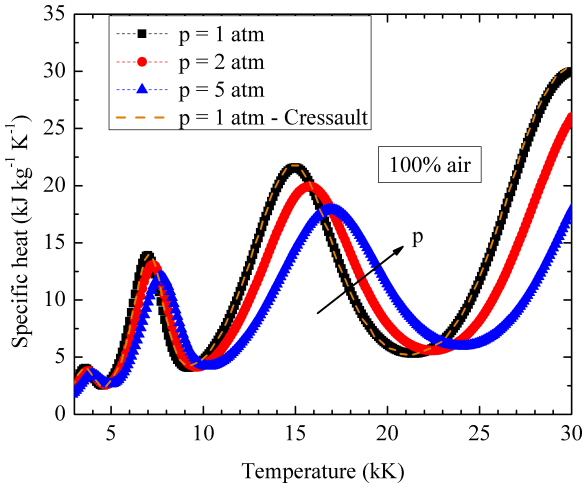

Figure 4.2: The variation of total specific heat of air with temperature at different pressures. The published data [86] is provided for air at atmospheric pressure.

the temperatures at which dissociation and ionization reactions occur increase. This is evident from the dissociation and ionization peaks shifting slightly to the right. The results for C_p at atmospheric pressure can be observed to be in excellent agreement with the published data.

4.4 Transport properties of compressed air

The transport properties of interest in the present work are viscosity, total thermal conductivity and electrical conductivity.

Viscosity

Firstly, the variations of viscosity (μ) and electrical conductivity (σ) with temperature are plotted in figure 4.3(a) for different values of pressure. At a given pressure, viscosity is proportional to the mean free path and temperature. At lower temperatures, when ionization is not present, neutral-neutral collisions with relatively smaller cross sections dominate and increasing temperature results in larger mean free paths. However, when ionization begins to increase, higher cross sections due to charge exchange and charge-charge Coulombic cross sections lower the mean free paths. Hence, the peak of viscosity

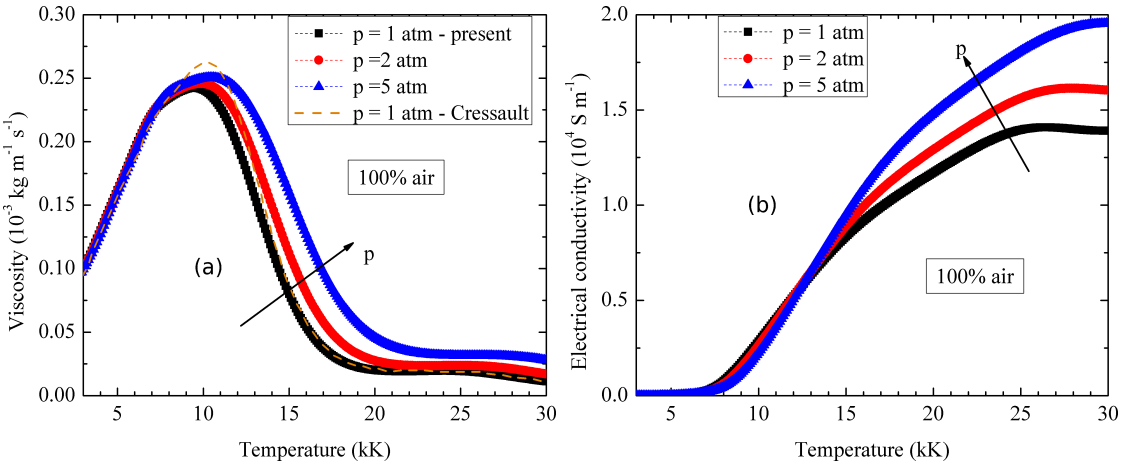

Figure 4.3: The variation of (a) dynamic viscosity and (b) electrical conductivity of air with temperature at different pressures.

roughly corresponds to the beginning of significantly higher contributions from charged species rather than neutrals. As pressure increases, the rightward shift of the peak obviously relates to the delayed contributions from charged species interactions because of greater ionization temperatures at higher pressures. The overlap at temperatures lower than 8,000 K for different pressures agrees with the kinetic theory's prediction of pressure independence of viscosity at lower temperatures. A comparison with Cressault's viscosity results for air at p = 1 atm indicates differences in the temperature range 8,000-15,000 K. This can be primarily attributed to the choice of interaction potentials to calculate electron-neutral and ion-neutral elastic cross sections which predominate in this temperature range. Our method utilizes "Lennard-Jones" type potential for ion-neutral interactions and uses the tabulated data of Laricchiuta *et al.* [70] for electron-neutral interactions to obtain their respective collision integrals. On the other hand, Cressault utilizes collision integral values from Capitelli *et al.* [89], which explains the deviation from his viscosity results. Nonetheless, the maximum relative error with respect to Cressault's values is less than 10%.

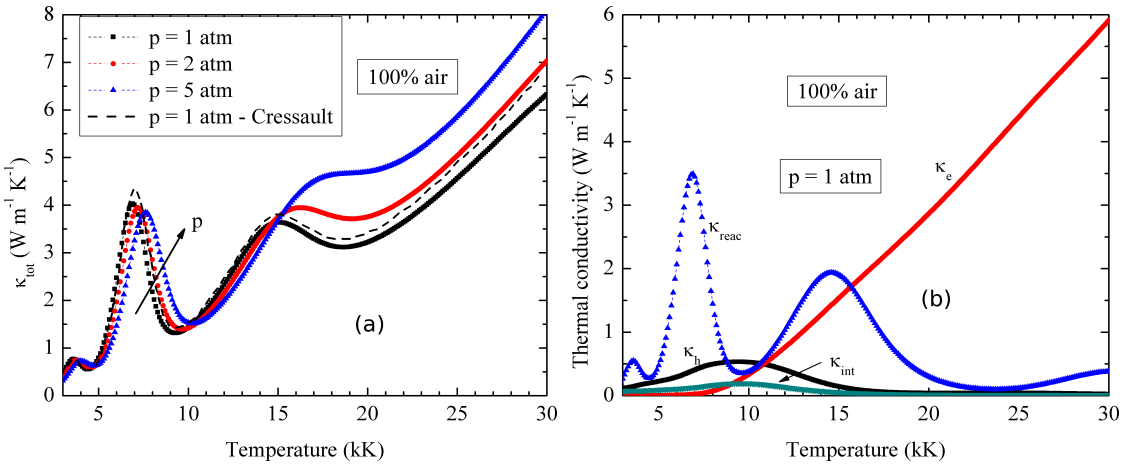

Figure 4.4: (a) The variation of total thermal conductivity of air with temperature at different pressures. (b) Variation of individual contributions toward total thermal conductivity with temperature at atmospheric pressure.

Electrical conductivity

The electrical conductivity σ, on the other hand, is proportional to the electron number density n_e, electron ordinary diffusion coefficient D_{ee}, pressure p and inversely proportional to the mass density ρ of the gas mixture. Hence the profile of σ in figure 4.3(b) for a given temperature mirrors that of the product: $n_e D_{ee} p/\rho$. The variable D_{ee}/ρ decreases with pressure and n_e increases with pressure for any temperature. Hence, the cumulative effect of this product determines the σ profile. For a given pressure, at lower temperatures where neutral-neutral collisions with smaller cross sections dominate, D_{ee} is significantly higher compared to higher temperatures where charged Coulombic collisions with higher cross sections dominate. In the case of air, for temperatures greater than 13,000 K, σ increases with pressure primarily due to greater contribution from increasing n_e compared to decreasing D_{ee}/ρ . The contrary is true for temperatures lower than 13,000 K.

Thermal conductivity

The total thermal conductivity (κ_{tot}) for air at different pressures is depicted in figure 4.4(a). The contributions of different thermal conductivities - heavy-species (κ_h), electron (κ_e), reactive (κ_{reac}) and internal (κ_{int}) - towards κ_{tot} at atmospheric pressure is provided in figure 4.4(b). For temperatures lower than 10,000 K at p = 1 atm, κ_{reac} and κ_h contribute the most towards κ_{tot}. Similar to C_p, κ_{reac} captures the dissociation peaks corresponding to diatomic oxygen and nitrogen at 3,500 K and 7,000 K respectively. Above 10,000 K, the contribution from κ_e becomes significant along with the additional contribution from κ_{reac} capturing the first ionization peak at 15,000 K. In particular, the contributions from the thermal conductivities apart from κ_e are negligible above 20,000 K. As pressure increases, similar to the behavior observed in C_p, the peaks in κ_{reac} shift to right and their amplitudes decrease. Increase in κ_e is observed with increasing pressure and hence its contribution is substantially higher for p = 5 atm compared to p = 1, 2 atm at temperatures above 15,000 K. The contribution from κ_{int} is usually negligible compared to the other three thermal conductivities. A comparison of κ_{tot} values from Cressault in figure 4.4(a) for p = 1 atm indicates excellent agreement at temperatures lower than 7,000 K and reasonable agreement with maximum relative error less than 20% above 7,000 K. The differences can be attributed to two main sources. Firstly, in the temperature range 8,000-15,000 K, slight differences are present in collision integrals due to different interaction potentials for electron-neutral and ion-neutral cross sections. At temperatures greater than 20,000 K, the κ_e values are much closer to those of Capitelli *et al.* [90] rather than Cressault [86]. This implies that there is a possibility of over-estimation of κ_e and hence κ_{tot} in Cressault's work.

4.5 Dielectric properties of compressed air

The species composition-dependent dielectric properties of interest in current work can be categorized into: (a) the swarm parameters, namely the electron drift velocity and electron characteristic energy given in (3.60) and (3.64) respectively, and (b) the net reduced ionization coefficient given in (3.68). Both (a) and (b) depend upon the EEPF and are required for the calculation of the reduced breakdown field E_{crit}/N. A comparison of our E_{crit}/N results with those of Tanaka [46] is presented in this section. It is

a common practice in the electrical discharge literature to consider the reduced electric field E/N, measured in Townsend ($1\ Td = 10^{-21} V m^2$), as an input rather than just the electric field E.

EEPF

In this work, the EEPFs are calculated using the Boltzmann equation solver BOLSIG+ [19] available through the zero-dimensional plasma kinetics package ZDPlasKin [20]. The set of neutral and excited-species required for the EEPF calculation are listed in tables C.1 and C.5 respectively of Appendix C. The list of reversible reactions considered for EEPF calculations are provided in table C.6 of Appendix C. The electron-impact momentum transfer, excitation, ionization and attachment cross section data for these reactions are gathered from standard databases [91, 92, 93, 94]. Specifically, the cross section data for diatomic nitrogen, oxygen and nitric oxide are taken from PHELPS database [93] while those for monatomic nitrogen and oxygen are chosen from MORGAN

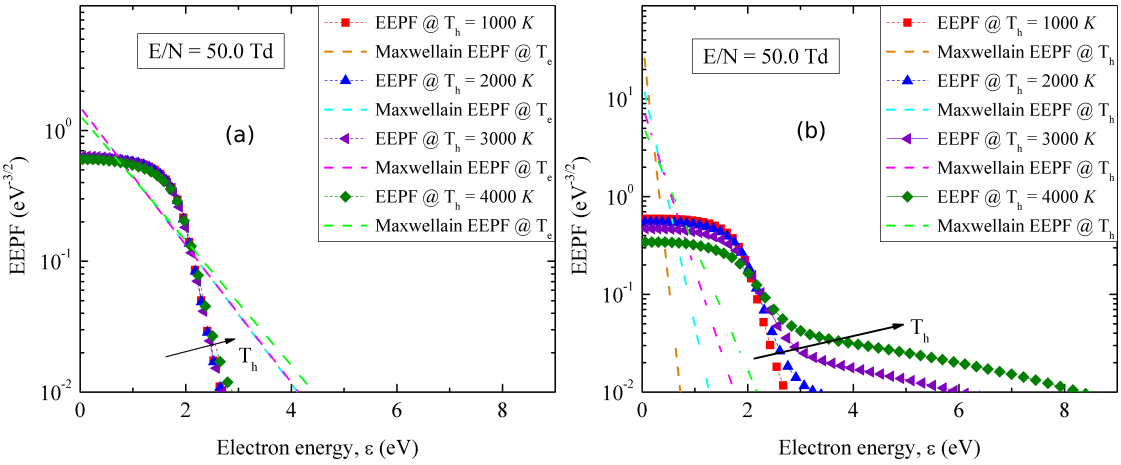

Figure 4.5: EEPF for atmospheric pressure air subjected to an $E/N = 50\ Td$: (a) excluding excited species effects, (b) including excited species effects.

database [94]. From the attachment cross-section data, it can be observed that diatomic oxygen is the most electro-negative species in air and is primarily responsible for the weak electronegativity of compressed air. Tanaka [46] has published results for the EEDF, which is the product of the EEPF with square root of electron energy ϵ, for

different N_2:O_2 gas mixture ratios at different temperatures. Tanaka, however, considers only ground-state species and neglects the effects of electron collisions with vibrationally-excited molecular species on the EEDF. We include these important effects for the EEPF calculation and highlight their significance by eventually comparing the breakdown field profiles with and without the excited species effects.

Depicted in figure 4.5(a) and (b) are the EEPF profiles for atmospheric pressure air at different temperatures, subjected to an E/N of 50 Td, with and without the excited species effects respectively. The population of vibrationally-excited diatomic species in this subsection are assumed to obey an equilibrium Boltzmann distribution. For comparison, the Maxwellian EEPF for these heavy-species temperatures (T_h) and the electron temperatures (T_e) calculated from the actual EEPF are also plotted in figure 4.5(a) and (b) respectively. The Maxwellian EEPFs are straight lines in a semi-log plot with slopes decreasing with increase in temperatures. A straight-forward observation is the significant deviation of the calculated EEPF from a Maxwellian EEPF for a moderately high E/N value observed post-CZ. With regard to the EEPFs without excited species effects, it can be seen that there is an extremely small difference for temperatures 1,000-3,000 K while a slight increase in the population of high-energy electrons is observed at 4,000 K. This is a consequence of greater contribution from electron-electron collisions at 4,000 K compared to 3,000 K. However, stark differences are observed between each temperature with the inclusion of excited species effects. The population of electrons with energies lower than 2 eV decreases while those with energies greater than 2 eV increase substantially with increase in temperature. The latter is primarily a result of super-elastic collisions in which a low-energy electron collides with an excited neutral species resulting in the loss of internal energy leading to de-excitation of the neutral and an increase in kinetic energy of the electron. The same behavior is observed for an $E/N = 100\ Td$. Also, the chief energy loss process for the electrons at each T_h pertains to vibrational excitation of diatomic species. This can be deduced from the collision cross sections of vibrational excitation process, which are related to the probability of occurrence of that process. The electron-neutral collisions leading to the formation of $v2$-$v6$ of N_2, $v1$-$v2$ of NO and $v1$ of O_2 have high cross sections in the order of $10^{-20}m^2$ in the energy ranges 2.0-3.0 eV, 0.7-1.3 eV and 0.4-0.8 eV respectively. Since each of these excited states have an associated threshold energy,

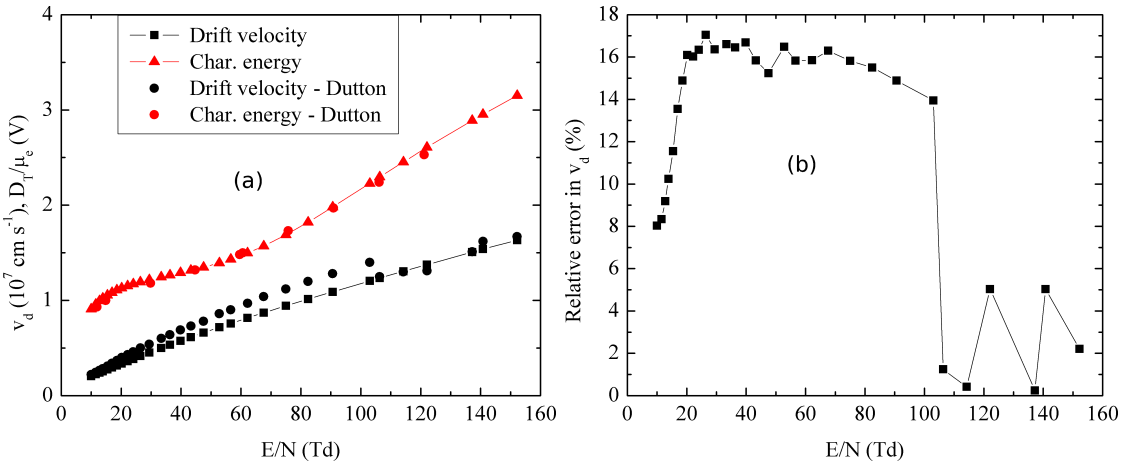

Figure 4.6: (a) Comparison of drift velocity and characteristic energy of atmospheric pressure dry air at 300 K with experimental results provided by Dutton [87]. (b) The relative error in the drift velocity values compared to those of Dutton.

as given in the section D.2, electrons with energies greater than 3.0 eV tend to lose their energies and begin to populate lower electron-energy regions. Since the mole fractions of N_2 are substantially higher than either O_2 or NO, greater electron population with energies lower than 2 eV as observed in figure 4.5 is a result of energy losses towards vibrational excitation of neutral N_2.

Swarm parameters

Several databases for electron-impact momentum transfer cross sections exist and hence, the chosen cross sections in the current work need to be validated. This validation is undertaken by comparing our electron swarm parameter results with the experimental data reported by Dutton [87], with the plots for 300 K provided in figure 4.6(a). To our knowledge, experimental data are available only at lower temperatures and are lacking at higher temperatures. The calculated characteristic energies D_T/μ_e at different E/N are observed to closely agree with experimental results with relative errors lower than 5%. With the relative error based on the experimental data provided in figure 4.6(b), the drift velocities (v_d) are found to be in reasonable agreement with the published data considering the reported experimental uncertainties.

Ionization coefficients

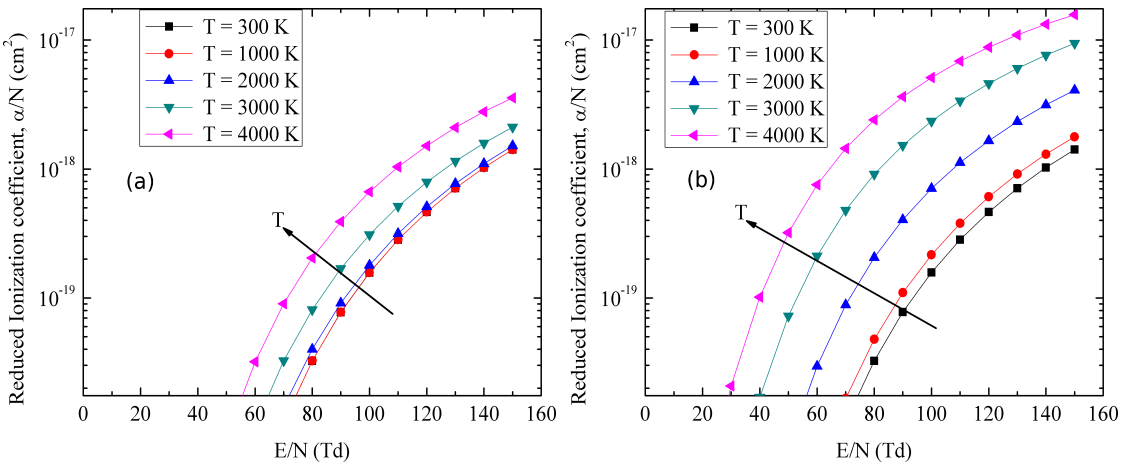

Figure 4.7: Reduced ionization coefficient α/N for atmospheric pressure air at different temperatures: (a) excluding excited species effects, (b) including excited species effects.

The Townsend ionization coefficients α are obtained from the reaction rates of electron-impact ionization collisions, labeled "I" in table C.7 of Appendix C. The accuracy of reaction rates depends upon the accuracy of ionization cross sections and hence, comparing these coefficients with experimental data serves as a validation for these cross sections. We have verified that the reduced ionization coefficient α/N profile at 300 K for E/N values lower than 150 Td agree extremely well with available experimental data [95]. The effects of excluding and including excited species on α/N of air at different temperatures are plotted in figure 4.7(a) and (b) respectively. Excluding excited species results in grossly under-predicting α/N especially at temperatures greater than 2,000 K. This is owing primarily to the significantly greater contribution from high-energy electrons in the EEPF tail, which are not captured while excluding excited species.

Reduced breakdown fields

In addition to α, breakdown fields depend upon the attachment coefficient η which depends upon the reaction rates of electron-impact attachment collisions. These attachment reactions are labeled "A" and listed in table C.7 of Appendix C. Finally, the

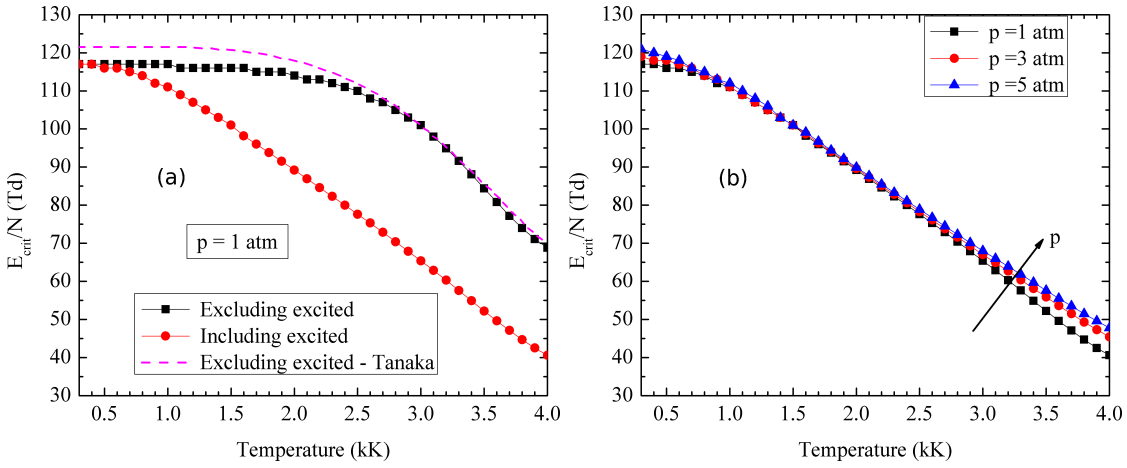

Figure 4.8: (a) Reduced breakdown field E_{crit}/N variation with temperature for atmospheric pressure dry air with and without excited species effects. (b) E_{crit}/N profiles for air at different pressures.

variation of the reduced breakdown field E_{crit}/N with temperature for air including and excluding excited species effects is displayed in figure 4.8(a). The relative error for E_{crit}/N calculated excluding excited species effects, with respect to the published results of Tanaka [46], is less than 5%. The decrease in E_{crit}/N after 1,500 K is related to the dissociation of O_2 and creation of NO, resulting in lower reduced attachment coefficients η/N. However, since E_{crit}/N depends on α/N, there is a significant over-prediction of E_{crit}/N owing to the neglection of excited species effects. For example, the exclusion of excited species effects increases E_{crit}/N at 4,000 K by approximately 75%. The E_{crit}/N profiles including excited species effects at different pressures are highlighted in figure 4.8(b). It can be observed that there is appreciable overlap between the profiles below 2,500 K, with a maximum deviation of approximately 20% at 4,000 K for the results at p = 5 atm from those at p = 1 atm. The observed overlap is an advantage arising from the use of E/N rather than E, because E/N captures the effects of both electric field and pressure simultaneously.

Chapter 5

Metal vapor effects

5.1 Sources and effects of metal vapor before CZ

5.1.1 Sources of metal vapor

There are two major sources of metal vapor in an LVCB prior to current zero - (a) electrodes/contacts and (b) splitter plates. There are two types of contact materials possible - (i) refractory or "hot" electron emitters possessing high vaporization temperatures, tungsten (W) for example, and (ii) non-refractory or "cold" emitters possessing low vaporization temperatures, copper (Cu) for example. An alloy of refractory and non-refractory materials with a suitable weight percentage is utilized in realistic circuit breakers, 50%-50% Cu-W for example. Owing to high (low) boiling points, refractory (non-refractory) materials suffer lower (greater) material losses due to evaporation. Nonetheless, owing to high current density and high temperature of the arc, significant erosion of the metallic contacts occurs during the time interval between arc initiation and arc motion away from the contacts towards the splitter plates. Additionally, several secondary arcs result from breaking up of the primary arc between the splitter plates. Owing to the ferromagnetic property of the splitter plates, usually composed of iron, the secondary arcs traverse within the splitter plate gaps for several hundreds of μs before their eventual extinction close to CZ. As a result, significant erosion of the non-refractory splitter plate material occurs during the time interval between initial attachment of secondary arc roots to the splitter plate surfaces and the eventual

extinction of the arcs. Hence, the metal vapor within the contact gap at and post-CZ is a mixture of vapors from the afore-mentioned sources.

5.1.2 Effects of metal vapor

The metal vapors in an LVCB prior to current zero contribute to significant radiative cooling of the primary arc. The presence of metal vapor in air, even in proportions as small as 1%, dramatically increases the emission and absorption coefficients [14]. This results in significantly higher rate of radiative arc cooling compared to the case of pure air. The increase in the radiation coefficients is a direct consequence of lower energy electronically excited states and lower ionization potentials of metal vapors. Apart from the radiation coefficients, addition of metal vapors affects both thermodynamic and transport properties of the plasma. For example, metal vapors result in greater electrical conductivity especially at temperatures lower than 10,000 K. We have computed the thermodynamic and transport properties of air-copper vapor plasma at LTE and a comparison of our results with published data [86, 96] will be provided in this chapter. Other important effects include the formation of metal particles by nucleation, condensation and coagulation during the gas cooling post-CZ [97, 98]. Even though liq-

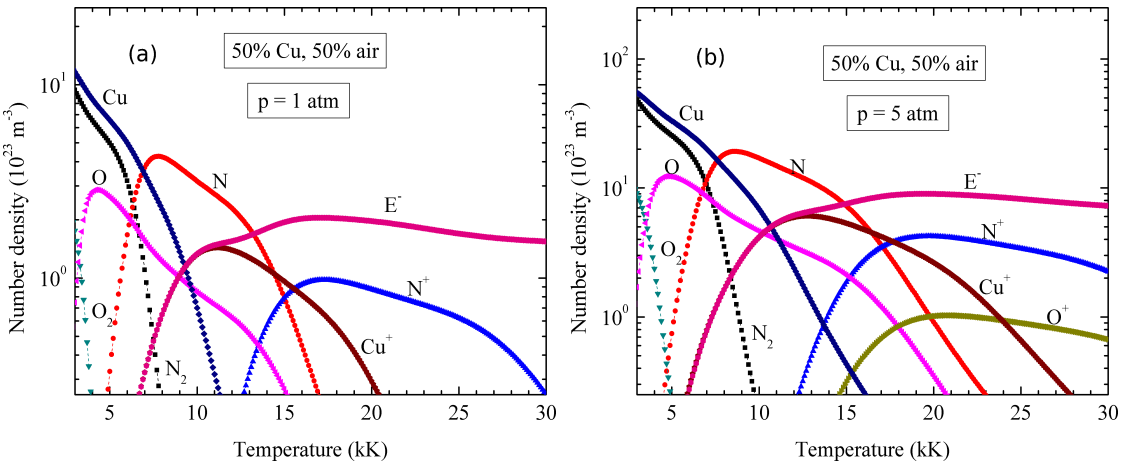

Figure 5.1: The variation of different species number densities with temperature for 50% Cu, 50% air at (a) p = 1 atm and (b) p = 5 atm.

uid/crystalline metallic condensed species are included in the composition calculations,

tracking their formation and capturing their effects on the breakdown field is beyond the scope of current thesis.

5.2 Equilibrium composition of air-copper mixtures

As mentioned in the previous chapter, the equilibrium composition for a general air-copper mixture is obtained by suitably setting the mole fraction of air x_{air} in the composition solver. In this chapter, the effect of copper vapor on properties at a given pressure will be presented in the form of results for $x_{air} = 0$ (100% Cu), $x_{air} = 0.5$ (50% Cu, 50% air), and $x_{air} = 1$ (100% air). The effect of pressure on different properties of air-copper mixtures are provided either for 50% Cu or 100% Cu case. The results for intermediate values of x_{air} will be presented in our forthcoming publications. The direction of the arrow in figures of this chapter either indicates the direction of increasing pressure p or increasing copper mole fraction %Cu, wherever appropriate. Since the boiling point of copper is approximately 2,800 K, we provide the results in the temperature range 3,000-30,000 K.

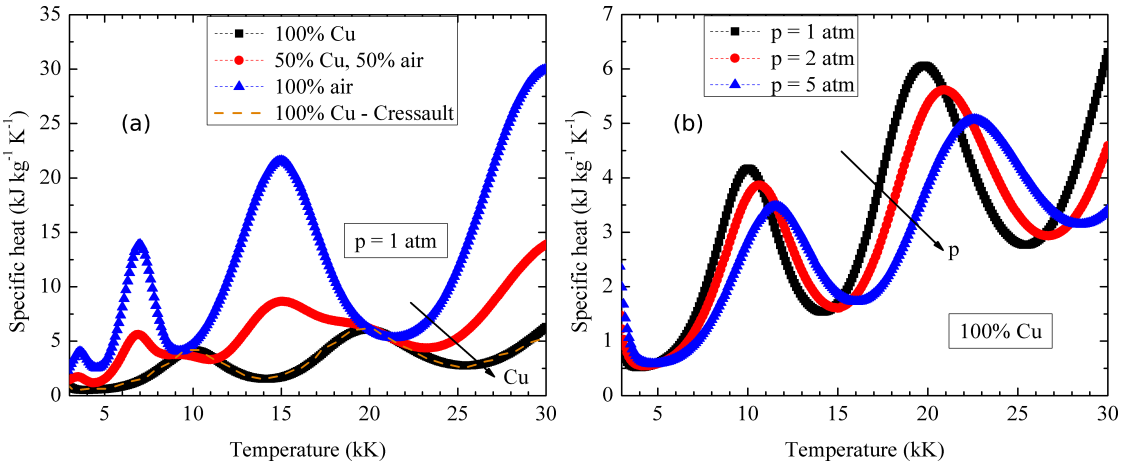

Figure 5.2: The variation of specific heat with temperature for (a) different %Cu at atmospheric pressure and (b) 100% Cu at different pressures.

The species with highest mole fractions for the 50% Cu case at p = 1 atm and p = 5 atm are captured in figure 5.1(a) and (b) respectively. The notable additions

to the 100% air results in the previous chapter are: monatomic copper (Cu) and its first ion (Cu^+). Monatomic copper has the lowest ionization energy of 7.72 eV among the species considered and hence, electrons are generated by ionization reactions at much lower temperatures compared to 100% air. This can be observed in the overlap of electron and Cu^+ number densities for temperatures lower than 10,000 K at both pressures in figure 5.1. It is worth mentioning that even though Cu^{2+} has significant number densities in the temperature range 15,000-30, 000 K, it is not included in the figure for the sake of clarity.

5.3 Thermodynamic properties of air-copper mixtures

The specific heat C_p profiles for different %Cu at $p = 1$ atm and 100% Cu at different pressures are presented in figure 5.2 (a) and (b) respectively. With the increase in %Cu, C_p decreases significantly in general and the amplitudes of the peaks for 100% Cu are approximately equal to the amplitudes of the troughs for 100% air. This is primarily due to the significant decrease in specific enthalpy resulting from significant increase in mass density ρ with increase in %Cu. Considering the profile for 100% Cu, the first and second peaks pertain to the first and second ionization of atomic copper respectively.

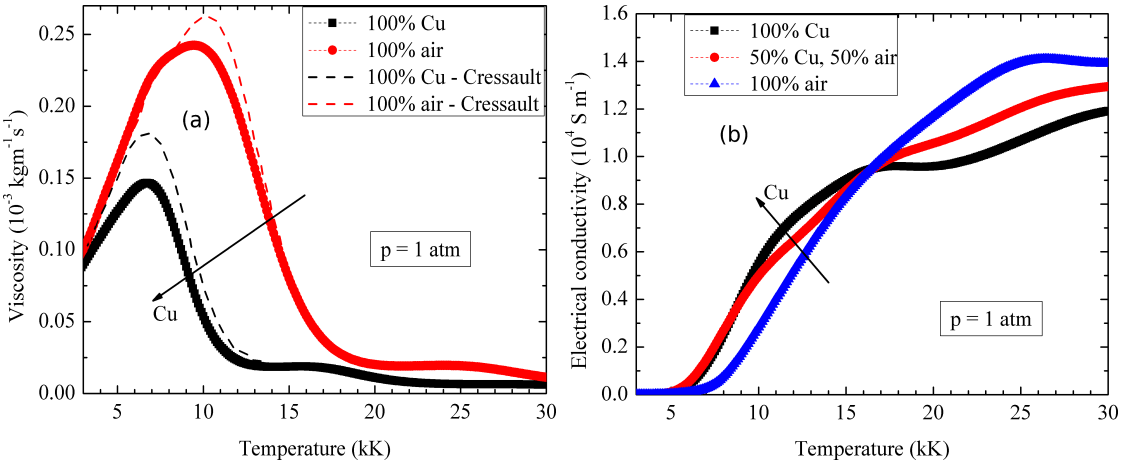

Figure 5.3: The variation of (a) dynamic viscosity and (b) electrical conductivity with temperature for different %Cu at atmospheric pressure.

The results for 100% Cu are in excellent agreement with the published data. The behavior of specific heat for 100% Cu with increasing pressure is similar to that for 100% air - peaks with decreasing amplitudes while shifting to higher temperatures.

5.4 Transport properties of air-copper mixtures

Viscosity

The viscosity profiles for pure air and pure copper at p = 1 atm including their comparison with published results are depicted in figure 5.3 (a). As the mole fraction of copper increases, the viscosity decreases significantly in the temperature range 7,000-17,000 K and there is a shift in the peak towards lower temperatures. The peak amplitude for pure copper is lower by approximately 40% compared to that for pure air. The lower viscosity can be explained by the emergence of ionization at lower temperatures compared to pure air, resulting in higher cross sections for charge-exchange and charge-charge interactions at these temperatures. The deviation from published results are greater for pure copper compared to that for pure air, which can be attributed to different collision integrals used by Cressault for Cu-Cu^+ interactions. Cressault [86] has considered a polarizability potential for Cu-Cu^+ interaction while a phenomenological Lennard-Jones model has been used in the current work.

Electrical conductivity

The electrical conductivities for different %Cu at p = 1 atm are plotted in figure 5.3(b). The profiles can be explained with the dependence of σ on the interplay between n_e and D_{ee}/ρ at a given pressure. Firstly, D_{ee} decreases significantly with the addition of copper to air because of charge generation at lower temperatures and increased Coulombic attraction suppressing the diffusion of electrons. Secondly, ρ and n_e increase with increase in copper mole fractions. At temperatures lower than 17,000 K, contribution from greater n_e compensates for the lower contribution from D_{ee}/ρ. However, the opposite effect is observed beyond 17,000 K since n_e begins to taper and decrease around 17,000 K.

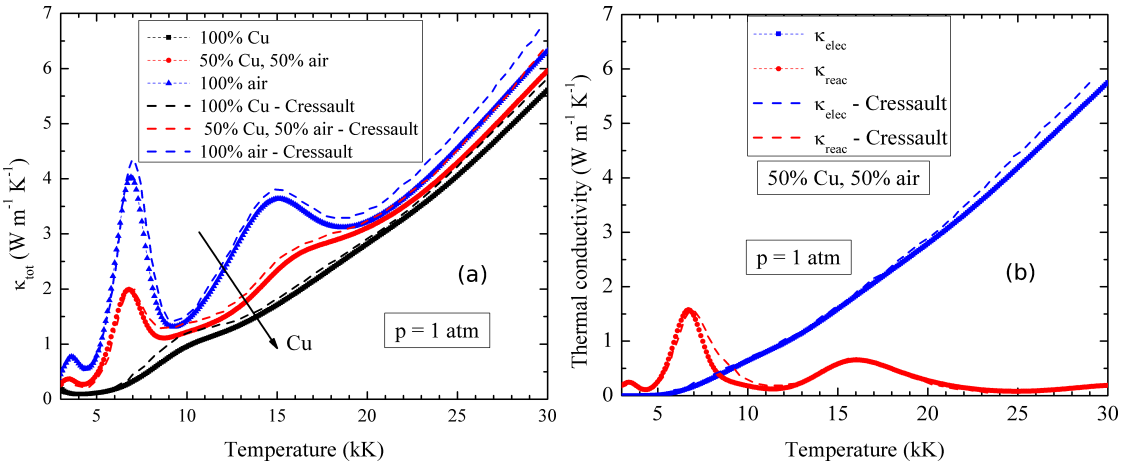

Figure 5.4: (a) The variation of total thermal conductivity with temperature for different %Cu. (b) Contributions from reactive (κ_{reac}) and electron (κ_e) thermal conductivity towards total thermal conductivity for 50% Cu at atmospheric pressure.

Thermal conductivity

Thermal conductivities for different %Cu at p = 1 atm are provided alongside published results in figure 5.4(a). As the copper mole fraction increases, the thermal conductivity decreases significantly especially at temperatures lower than 15,000 K. The O_2 dissociation peak at 3,500 K, N_2 dissociation peak at 7,000 K and first ionization peak at 15,000 K for pure air are diminished progressively with increase in %Cu. The dissociation and ionization peaks with diminished amplitudes can be observed for the 50% Cu case. Since the peaks are primarily due to the contribution from κ_{reac}, lower κ_{tot} are a consequence of decreasing κ_{reac} with increasing %Cu. The deviation of our κ_{tot} calculations from published data is observed to increase with increase in %Cu. The contributions from κ_{reac} and κ_e toward κ_{tot}, along with published results, for 50% Cu are presented in figure 5.4(b). At temperatures in the range 7,000-10,000 K, the deviation from κ_{reac} is owing to the different collision integrals used by Cressault for Cu-Cu^+ interactions. Similar to the pure air case, κ_e is over-predicted by Cressault at temperatures greater than 15,000 K. The contribution from κ_{int} is negligible at all temperatures.

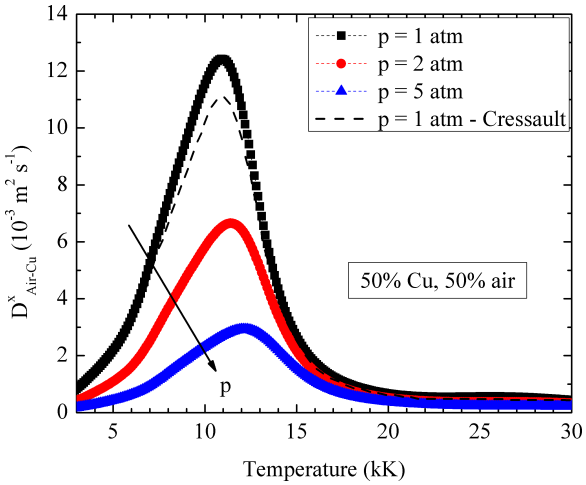

Figure 5.5: The variation of combined ordinary diffusion coefficient ($\overline{D^x}_{Air-Cu}$) with temperature for 50% air, 50% Cu at different pressures. The published data [96] is provided for $\overline{D^x}_{Air-Cu}$ at atmospheric pressure.

Combined diffusion coefficients

For air-copper mixtures with intermediate mole fraction values between 0 and 1, combined diffusion coefficients owing to gradients in mole fraction, pressure and temperature can be calculated. Since the combined diffusion coefficients due to mole fraction gradients are significantly higher compared to pressure and temperature, we present only the combined ordinary diffusion coefficients ($\overline{D^x}$) in this work. The variation of $\overline{D^x}$ with pressure for 50% Cu is presented in figure 5.5 and it can be deduced easily that $\overline{D^x}$ decreases with pressure. This is primarily because $\overline{D^x}$ depends upon the ordinary diffusion coefficients D_{ij}, which have an inverse proportionality with pressure as seen from (3.108).

5.5 Dielectric properties of air-copper mixtures

In this section, we focus on the characteristics of EEPF for air-copper mixtures with different %Cu. We then provide the variation of E_{crit}/N with temperature for different %Cu and the temperature range of interest is 300-6,000 K. We chose 6,000 K as the maximum temperature for the breakdown field calculations since the electron

mole fractions at 6,000 K for different %Cu range between 10^{-2}-10^{-1}, meaning that a small residual current flow can be expected at higher temperatures with correspondingly higher electron number densities.

Composition including condensed species

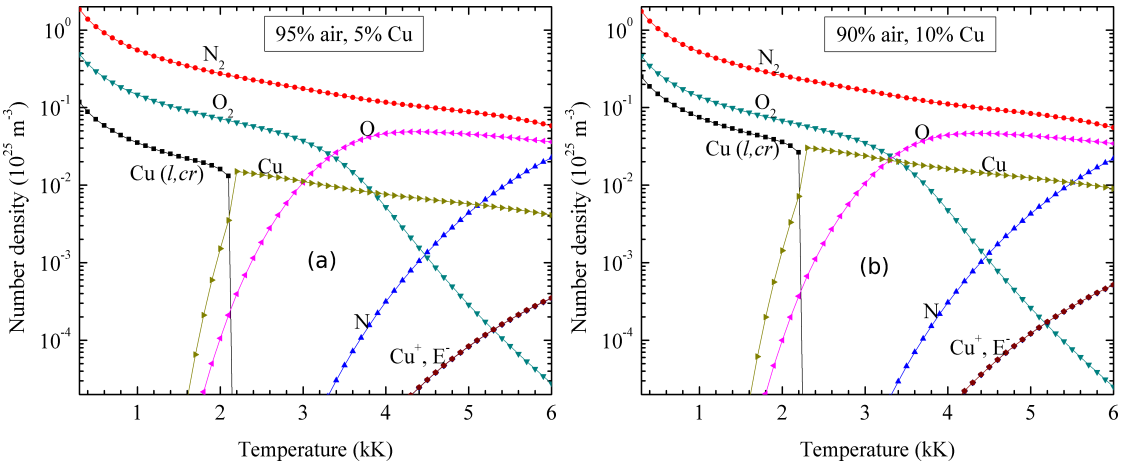

Figure 5.6: The variation of different species number densities with temperature for atmospheric pressure air-copper mixtures with: (a) 5% Cu and (b) 10% Cu.

The minimum temperature considered for the equilibrium composition in the previous section is 3,000 K, since pure copper exists in gaseous form at temperatures above its boiling point of approximately 2,800 K. However, we require breakdown fields for the temperature range of interest and hence, it is imperative that the condensed species of copper Cu(l,cr) be included at temperatures lower than 3,000 K. The composition calculation is split into the following parts: (i) 300-4000 K including condensed species using White's method, (ii) 4000-6,000 K excluding condensed species using Godin's method. This split provides high computational efficiency as well as accuracy. As a validation, the neutral species number densities between 4,000-6,000 K from both the methods are observed to be in excellent agreement with each other. We have also verified that the NIST-JANAF tables for Cu^+ result in erroneously high internal partition function values leading to significantly high number densities of Cu^+. Owing to electroneutrality, the electron number densities are significantly high and hence, there is an

over-prediction of ionic number densities between 4,000-6,000 K. Since, the Boltzmann solver requires the knowledge of electron number densities at all temperatures, Godin's method is utilized to determine the charged species number densities between 300-6,000 K.

The species composition corresponding to 5% and 10% copper mole fractions are plotted in figure 5.6(a) and (b) respectively. A sudden plunge of the condensed species number densities can be observed around approximately 2100 K, which corresponds to the isothermal phase change of liquid-crystalline copper ($\mathrm{Cu}(l, cr)$) to gaseous copper (Cu). The temperature at which the phase change occurs increases with increase in %Cu, reaching 2,800 K for 100% Cu. The atomic copper number densities for 10% Cu are roughly twice as those for 5% Cu. Higher electron number densities are observed at a lower temperature for 10% Cu compared to 5% Cu and in general, the electron number densities increase with increase in %Cu.

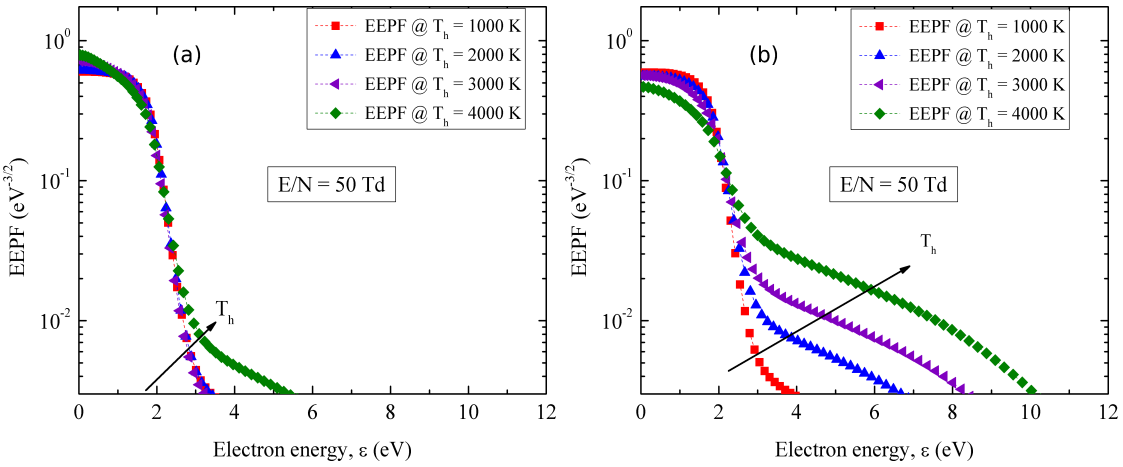

Figure 5.7: EEPF for atmospheric pressure air-copper mixture with 5% Cu subjected to an $E/N = 50\ Td$ at different T_h: (a) excluding excited species effects, (b) including excited species effects.

EEPF

The electron-impact reactions, including those related to copper, considered for the EEPF calculations are listed in table C.5 of Appendix C. The momentum-transfer cross

section of monatomic copper is extremely important and needs to be carefully chosen from the available published data [50, 99, 100]. We choose the momentum-transfer data of Chervy [99] in the lower energy range 0-15 eV and the data of Tkachev [100] in the energy range 15-100 eV. This cross section data was utilized for determining the collision integrals corresponding to electron-atomic copper interaction in the calculation of transport properties. The reasonable agreement with published transport properties serves as a validation for the cross section data. In this work, we neglect the effects of condensed species on EEPF despite capturing their number densities in the composition calculation. Including the particulate effects in partially ionized gases at atmospheric pressure is highly complicated because the high collision frequencies at these pressures necessitates the inclusion of particles of several sizes and charges along with other species. Practically speaking, the size of particles found on a circuit breaker wall surface after a TRV breakdown test are several hundred μm, which is much higher or on the order of Debye length in a high-pressure collisional plasma. This results in the breakdown of the simplified orbital motion limited (OML) theory [101] which holds approximately for low pressure plasma. Moreover, the CFD solver currently does not possess a module dealing with the tracking of particulate matter because of the extremely high computational effort required. We first consider figure 5.7(a) depicting the EEPF for 5% Cu subjected

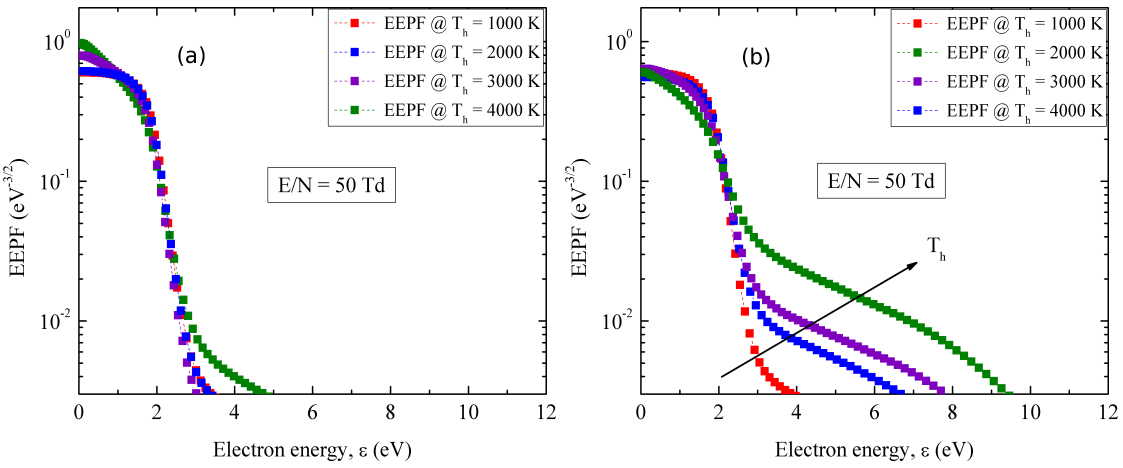

Figure 5.8: EEPF for atmospheric pressure air-copper mixture with 10% Cu subjected to an $E/N = 50\ Td$ at different T_h: (a) excluding excited species effects, (b) including excited species effects.

to an E/N of 50 Td excluding excited species effects. Atomic copper possesses significantly high momentum transfer cross sections at electron energies in the range 0-2 eV, compared to the species related to air. Hence, at temperatures in the range 2,000-4,000 K in the presence of Cu, there are significantly high electron-energy losses due to elastic scattering resulting in a greater population of lower energy electrons. This can be observed from the increase in the lower energy peak at 3,000 and 4,000 K compared to 2,000 K. Also, at 4,000 K, with electron mole fractions around 10^{-5}, electron-electron

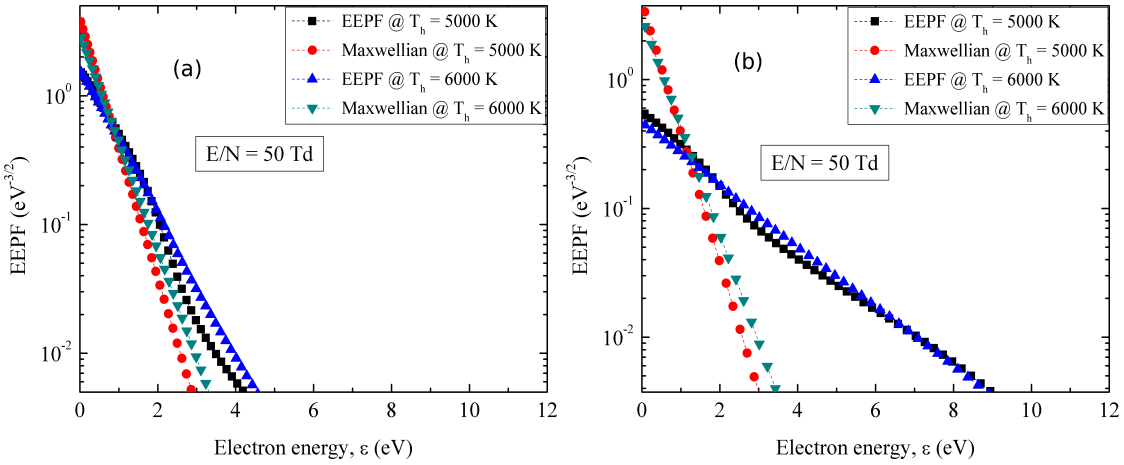

Figure 5.9: Maxwellization of EEPF for air-copper mixture with 10% Cu at higher temperatures subjected to an $E/N = 50\ Td$: (a) excluding excited species effects, (b) including excited species effects.

collisions at high E/N result in the re-population of the high-energy tail [19]. The electron-electron collisions result in the "Maxwellization" of the EEPF, which will be clarified later in this subsection. Similar to the observations for pure air, inclusion of excited species effects in the form of super-elastic collisions results in significant increase in the population of high-energy electrons. In addition to the vibrationally-excited species considered for air, there are electronically-excited species for Cu at lower energy levels of 1.5-3.0 eV compared to other species. The electronically-excited species of Cu are assumed to follow a Boltzmann distribution and hence, their number densities increase with increase in T_h. Hence, the inclusion of super-elastic collisions corresponding to these excited species in addition to those considered for air results in greater population of high-energy electrons at higher T_h. These observations hold true for 10% Cu as

illustrated in figure 5.8, albeit with minor differences. With increase in %Cu, and hence the electron and Cu number densities, the energy loss due to elastic scattering increases resulting in greater electron population with lower energies for 10% Cu compared to 5% Cu. This translates to a smaller population within the high-energy tail at 3,000 and 4,000 K for 10% Cu compared to 5% Cu. Finally, the EEPFs for 10% Cu are shown in figure 5.9 at 5,000 and 6,000 K. At these temperatures, electron-electron collisions

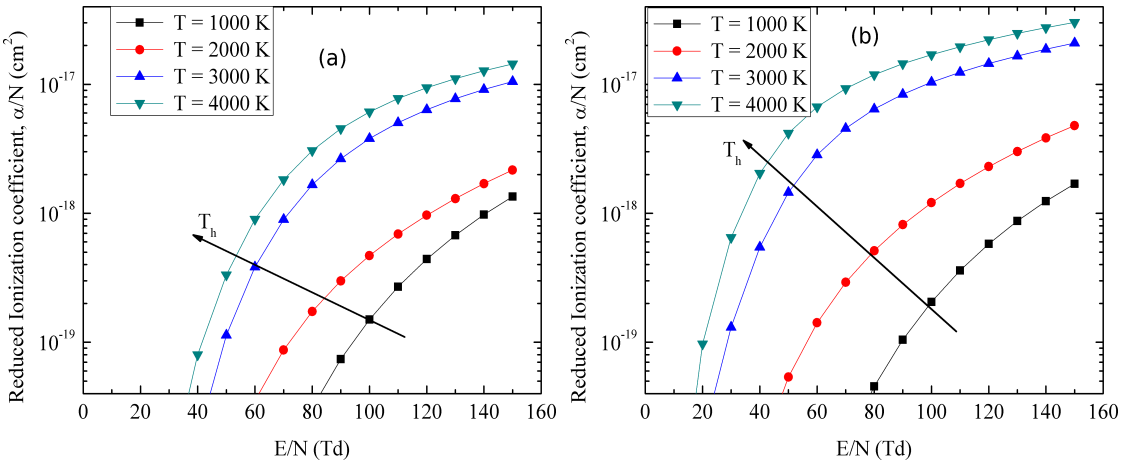

Figure 5.10: Reduced ionization coefficient α/N variation with reduced electric field for atmospheric pressure air-copper mixture with 5% Cu at different temperatures: (a) excluding excited species effects, (b) including excited species effects.

begin to affect the EEPF by increasing the population of electrons at high energy levels resulting in a near-Maxwellian distribution. With or without excited species effects, a Maxwellian EEPF is observed for 6,000 K. Most importantly, the lower slope observed after including excited species effects corresponds to a higher electron temperature T_e compared the case excluding those effects. Additionally, at these high temperatures and extremely small E/N values ($\approx 10^{-2}\ Td$), exclusion of super-elastic collisions produces an erroneous EEPF which results in a T_e lower than T_h, which is unphysical.

Ionization coefficients

In order to calculate the ionization coefficients (α), the contributions from different ionization reactions listed in table C.7 of Appendix C are tallied. The ionization cross

sections for electronically-excited monatomic species are not available in the literature. To circumvent this limitation, we utilize the ionization cross sections of their ground-state monatomic parent species [102, 103] and reduce the electron energies in the cross section data by the relevant thresholds of excited species' energies. For example, we consider ground state Cu with an ionization energy of 7.72 eV and the excited species Cu($e1$) possessing a threshold of 1.5 eV with respect to ground state Cu. The ionization cross section data for Cu($e1$) was obtained by reducing the electron energies in ionization cross section data for Cu by 1.5 eV. This approximation imitates the process of step-wise ionization: an electron with energy lower than the ionization energy of Cu but higher

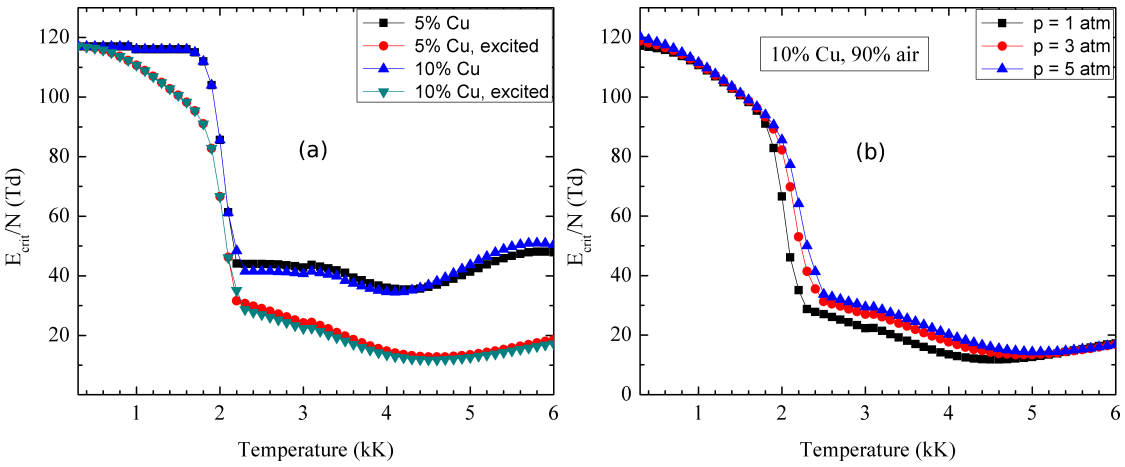

Figure 5.11: (a) Reduced breakdown field E_{crit}/N variation with temperature for atmospheric pressure air-copper mixture with 5% and 10% Cu, with and without excited species effects. (b) E_{crit}/N profiles for air-copper mixture with 10% Cu at different pressures.

than the threshold energy of Cu($e1$) results in the formation of Cu($e1$), which possesses an ionization energy lower than Cu's ionization energy by 1.5 eV. Subsequently, an electron with energy around 6.5 eV, which is still lower than Cu's ionization energy of 7.72 eV, is capable of ionizing Cu($e1$).

Similar to air, the super-elastic collision effects on EEPF are clearly visible through the plot of α/N in figure 5.10. Even though only a small mole fraction value of 5% Cu is considered, the α/N including excited species effects are roughly twice those excluding the effects for 3,000 and 4,000 K. The addition of a small percentage of Cu results in

higher α/N compared to pure air, which can be observed from the comparison of figures 4.7(b) and 5.10(b) respectively.

Reduced breakdown fields

The reduced breakdown fields E_{crit}/N are calculated by tallying the contributions to ionization (α) and attachment (η) coefficients from ionization and attachment reactions listed in table C.7 of Appendix C. A comparison of E_{crit}/N with and without excited species effects is provided in figure 5.11(a) for 5% and 10% Cu at atmospheric pressure. We first consider the case excluding excited species effects. Tanaka [50] has plotted the E_{crit}/N variation with temperature for copper mole fractions in the range 0-10%. Following Tanaka's procedure, we have verified that our E_{crit}/N results for 10% Cu agree extremely well with his published results. However, we refrain from providing the comparison because Tanaka does not include all the excited species of Cu in his EEPF and E_{crit}/N calculation. From figure 5.11(a), it can be observed that including excited-species effects on EEPF results in significant reduction in E_{crit}/N for both 5% and 10% Cu. A greater %Cu results in a greater energy loss through elastic scattering resulting in lower α for 10% Cu compared to 5% Cu at temperatures greater than 4,000 K. Hence, the E_{crit}/N excluding excited species effects is higher for 10% Cu at these temperatures. On the other hand, at temperatures greater than 2,000 K, the E_{crit}/N including excited species effects is lower for 10% Cu compared to 5% Cu. As % Cu increases, the E_{crit}/N including excited species effects decreases with temperature. This trend rightly describes the detrimental effects of higher concentrations of metal vapor, resulting in lowering the breakdown fields.

The effect of pressure on E_{crit}/N of 10% Cu, including excited species effects, is presented in figure 5.11(a). The boiling point of Cu increases with increase in pressure and hence, the isothermal phase change at which $\mathrm{Cu}(l, cr)$ gets converted to gaseous Cu occurs at a higher temperature at higher pressures. This is reflected in the E_{crit}/N profiles traversing to the right at around 2,200 K. With increasing pressure, the number densities of Cu and hence its excited states increase resulting in slightly higher E_{crit}/N at higher pressures, especially for temperatures in the range 2,000-4,500 K. At other temperatures, an excellent overlap of E_{crit}/N profiles is observed.

5.6 Finite-rate kinetics in air-copper mixtures

In the previous section, breakdown fields were calculated with species composition obtained assuming chemical equilibrium. However, deviations from chemical equilibrium are observed post-CZ due to finite-rate chemical reactions. Lower chemical reaction rates are a result of the contact gap cooling and the ensuing temperature decay post-CZ, compared to the faster reaction rates in the high-temperature, high-current arc phase. Computation of species composition variation with time for a specified temperature decay and an associated cooling rate has been performed for SF_6 gas [8,83] in a HVCB. Two of the important assumptions of interest to this work, considered by Gleizes *et al.*, [83], are: (a) Maxwellian EEPF for all species and (b) no recovery voltage applied across the contacts. However, based on our literature survey, we have not found equivalent studies for air-metal-plastic vapor mixtures in an LVCB. To address this shortcoming, we have developed a finite-rate chemical reaction solver following the CHEMEQ2 method [17] for air-metal-plastic vapor mixtures. The two assumptions made by Gleizes are relaxed by taking into account: (i) a general non-Maxwellian EEPF for electrons and (ii) a recovery voltage of suitable magnitude across the contact gap. These two assumptions are essentially inter-related since the appearance of (ii) is responsible for (i). Our solver is capable of calculating chemical non-equilibrium composition including temperature decay and non-Maxwellian reaction rate effects.

In realistic LVCBs, it is roughly estimated that cooling rates range from 10^7 to 10^8 K/s and the temperatures near CZ range between 5,000-8,000 K. In this work, we assume a temperature decay from an initial temperature of 8,000 K to a final temperature of 2,000 K over time durations of 60 μs and 600 μs. The time durations considered correspond to the cooling rates of 10^8 and 10^7 K/s respectively. In this section, we present results for the species composition variation with time pertaining to air-copper mixtures, for a cooling rate of 10^8 K/s. The results for 10^7 K/s cooling rate are currently under investigation and will be provided in a future publication. Also, TRV magnitudes of 400 V and 300 V are applied across a contact gap of length 2 cm. Since the deviation of breakdown field results for 300 V are within 5% compared to those for 400 V, species composition and breakdown field results are presented for

400 V alone. In order to facilitate a comparison with published data, the air and copper related reaction rates are gathered from Teulet *et al.* [51] and the NIST kinetics database [104]. In the reaction set considered, there are 15 species: N_2, N, O_2, O, NO, Cu_2, Cu, N_2^+, N^+, O_2^+, O^+, O^-, NO^+, Cu^+, E^- and 84 reversible reactions [51]. Condensed species are not included in the reaction mechanism and hence, the composition calculations below 2,500 K are not expected to be accurate. This will be remedied in a future work by including gas-solid reactions leading to particulate formation. The electron-impact reactions in the set include: (a) ionization reactions of N_2, N, O_2, O, NO, Cu and (b) attachment reactions of O_2, O. There are two variations possible with the electron-impact reaction rates calculated using: (i) a Maxwellian EEPF and (ii) a non-Maxwellian EEPF calculated using Boltzmann equation solver. The Maxwellian and non-Maxwellian EEPFs correspond to the absence and application of the 400 V TRV. Subsequently, the breakdown fields based computed using the composition from finite-rate kinetics with Maxwellian and non-Maxwellian EEPFs are compared with the breakdown fields using chemical equilibrium. The computational effort is expected to increase significantly when the effects of plastic vapor are included in future.

The following steps are followed to obtain the non-equilibrium composition, provided the mass fraction of copper (y_{Cu}), TRV magnitude and the constant cooling rate values are known:

1. At time $t = 0$, the species number densities are set according to the chemical equilibrium composition at 8,000 K. The initial time step Δt_{init} is determined by the kinetics solver, based on the reaction with the smallest time scale.

2. If the computation does not involve an applied TRV, a Maxwellian EEPF corresponding to the heavy-species temperature is utilized for calculating the reaction rates for electron-impact processes. On the other hand, if a finite TRV is introduced at $t = 0$, the electron-impact reaction rates are evaluated using the non-Maxwellian EEPF from BOLSIG+. The time steps Δt can be in the order of a few ns and hence, the steady-state must be reached much faster for the EEPF calculation to be valid. Fortunately, the collision frequencies in air-copper mixtures are on the order of 10^{10}-10^{11} s^{-1} and hence the steady state time scales for EEPF are in the range 10^{-10}-10^{-11} s.

3. With all the relevant reaction rates known, the species composition at the end of Δt_{init} is obtained.

4. The following four conservation conditions need to be satisfied within acceptable tolerances: (a) Ideal gas law, (b) electro-neutrality, (c) nucleus ratio between the elements nitrogen and oxygen and (d) nucleus ratio between the elements oxygen and copper. Even though it is mentioned in the literature [83] that the conservation conditions are satisfied at each time step provided they are satisfied at $t = 0$, deviations from these conditions need to be evaluated. For our 10^8 K/s cooling rate calculations, the deviations were much smaller than 5%.

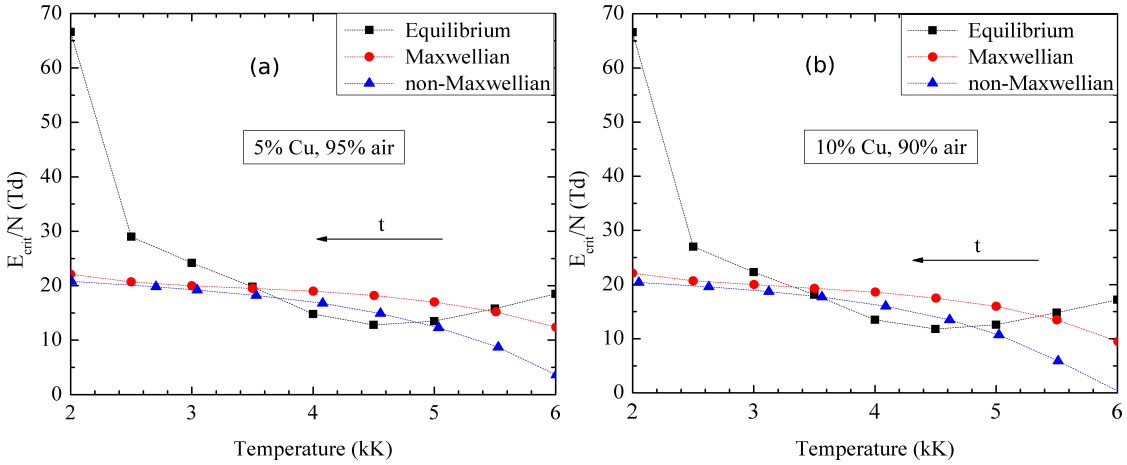

Figure 5.12: Comparison of E_{crit}/N variation with temperature, between Maxwellian and non-Maxwellian EEPF-based rates, for mole fractions: (a) 5% Cu and (b) 10 % Cu. The equilibrium composition based E_{crit}/N is additionally plotted.

5. Using the non-equilibrium composition at the end of a time-step, E_{crit} is calculated using the same procedure used for chemical equilibrium composition.

6. Steps 2-5 need to be repeated for every subsequent Δt till the end time (t_{end}) is reached, starting with the composition at the end of previous Δt. For 10^8 K/s and 10^7 K/s constant cooling rates, t_{end} equals 60 μs and 600 μs respectively.

This procedure is then repeated for different values of y_{Cu}. Finally, the E_{crit} calculated with the non-equilibrium compositions using the Maxwellian and non-Maxwellian reaction rates are added as new columns to the look-up table containing E_{crit} from equilibrium composition. In the figures presented, the two non-equilibrium cases are labeled as "Maxwellian rates" and "non-Maxwellian rates" respectively, for convenience.

In this section, we furnish results for $y_{Cu} = 0.2$, 400 V TRV and 10^8 K/s, at different time instants during the temperature decay. This y_{Cu} equals 10% in mole fraction terms. The mass fraction values in the CFD solver post-CZ are predominantly close to 20%. For clarity, the variables of interest are plotted against temperature, with an arrow depicting

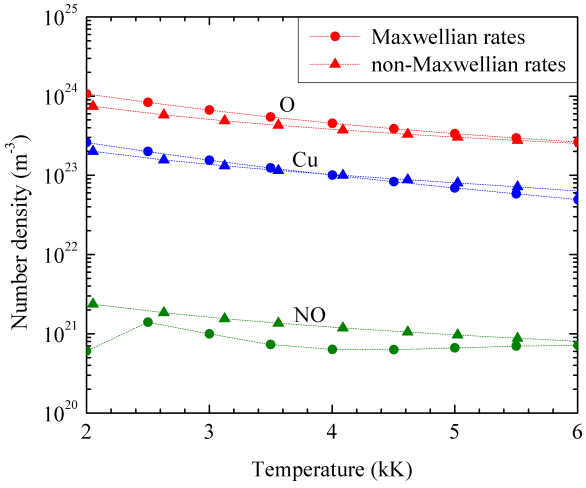

Figure 5.13: Important species with significant contributions toward determining the reduced breakdown field. Their number densities for 10% Cu are plotted against temperature.

the direction of increasing time and decaying temperature. Plotted in figure 5.12 is the variation of reduced breakdown field with temperature for two different copper mole fractions of 5% and 10%. The temperature range of interest is 2,000-6,000 K. The upper limit of 6,000 K is chosen in accordance with the maximum temperature in the equilibrium breakdown field calculations. Below 2,000 K, significantly high number densities of monatomic copper are expected to be form due to condensation. Since the reaction mechanism does not include phase-transition reactions, the number densities of copper will be over-predicted below 2,000 K and hence, the choice of 2,000 K as the lower limit. We would like to re-iterate that the reduced breakdown field values calculated

below 2,500 K are expected to be inaccurate since the effects of particulate matter are not included in the EEPF calculations. From figure 5.12, for both 5% and 10% mole fractions, E_{crit}/N values calculated using non-Maxwellian EEPF-based composition are lower than those computed using Maxwellian EEPF-based composition. The difference in the E_{crit}/N values between the Maxwellian and non-Maxwellian EEPF-based rates increase substantially above 4,000 K. The results in the following paragraphs will be used to explain the reasons for the profiles in figure 5.12, at temperatures greater than 4,000 K.

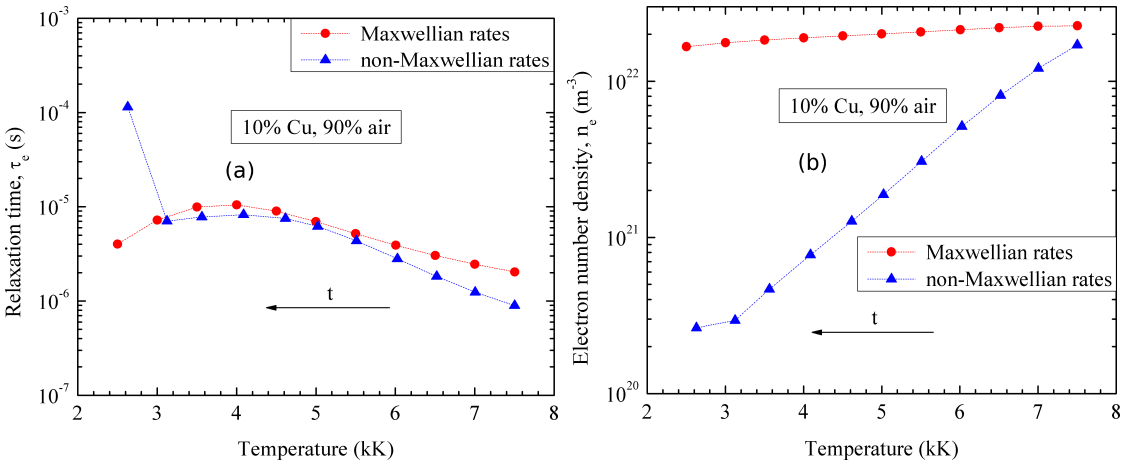

Figure 5.14: (a) Relaxation time for electrons and (b) electron number densities, at different time instants for Maxwellian and non-Maxwellian cases, with Cu mole fraction equal to 10%.

Firstly, we focus on the important species which contribute significantly to the ionization and attachment coefficients. With regard to the ionization coefficient, ionization of Cu is the chief contributor while for the attachment coefficient, direct electron attachment to O and dissociative electron attachment to NO are the major contributors. The variation of their number densities with temperature is provided in figure 5.13. In a direct contrast to the equilibrium composition where oxygen atoms recombine to form diatomic oxygen at lower temperatures leading to decline in their number densities, the non-equilibrium monatomic oxygen composition increases with decrease in temperature. A similar trend for monatomic nitrogen is observed. This leads to the important conclusion that in the faster cooling rate regime of 10^8 K/s, there is not enough time

available for chemical equilibrium to be attained. Also, the difference in the copper number densities between Maxwellian and the non-Maxwellian cases increases above 4,500 K.

Secondly, we focus on the electrons. We plot the electron relaxation times and number densities in figure 5.14. With the decay time τ_i in section obtained for all reactions in which electrons are lost, the total electron relaxation or decay time τ_e is computed using:

$$\frac{1}{\tau_e} = \sum_i \frac{1}{\tau_i}, \tag{5.1}$$

From figure 5.14, the electron relaxation times for the Maxwellian EEPF-based rates is higher compared to those for non-Maxwellian EEPF-based rates and this is reflected in turn in the electron number densities which are much lower for the latter compared to the former. The greatest contribution towards electron decay for non-Maxwellian case is from the electron-Cu^+ recombination reaction at all temperatures. On the other hand, for the Maxwellian case, the greatest contributions are from the dissociative recombi-

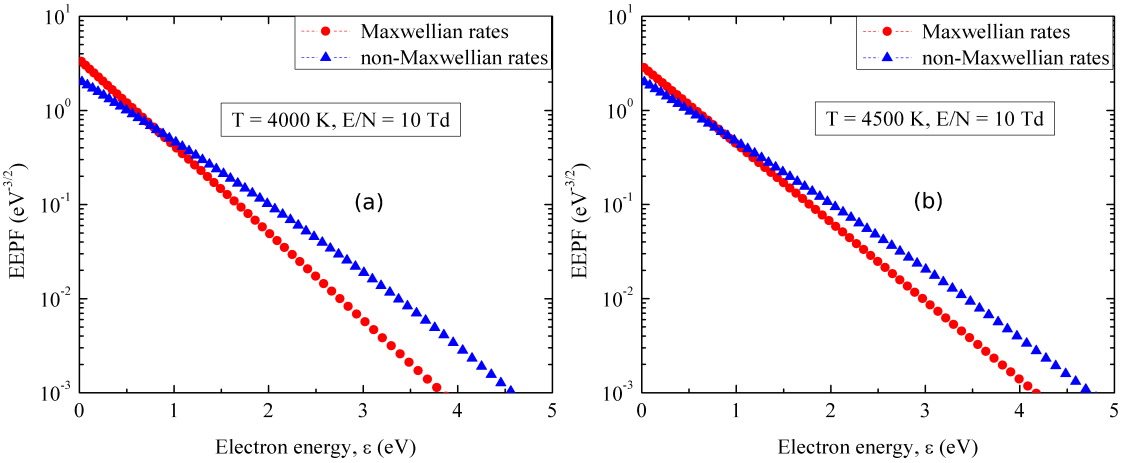

Figure 5.15: EEPFs calculated at $E/N = 10\,Td$ using the non-equilibrium compositions, at times (a) $t = 40\ \mu s$ and (b) $t = 35\ \mu s$ post-CZ when the temperatures are 4,000 K and 4,500 K respectively. The cooling rate is constant and equals $10^8\ K/s$.

nation of electron-NO^+ and electron attachment to monatomic oxygen at temperatures above and below 4,500 K respectively. The reduced breakdown fields for temperatures in the range 4,000-5,500 K for both the Maxwellian and non-Maxwellian cases are in

the proximity of 10 Td. Hence, a comparison of the EEPFs using the compositions from Maxwellian and non-Maxwellian cases, at two different time instants and $E/N = 10\ Td$ are depicted in figure 5.15. At $t = 35$ and 40 μs, the temperatures 4,500 and 4,000 K are reached. Comparing the EEPFs in figure 5.15(a) and (b), the EEPF corresponding to the composition from Maxwellian EEPF-based rates has lower population of high-energy electrons compared to that from non-Maxwellian EEPF-based rates. With the difference in copper number densities extremely small at 4,000 and 4,500 K, the contribution from copper towards the ionization coefficient is significantly higher for the non-Maxwellian case compared to the Maxwellian case. Also, owing to higher electron-electron collisions arising from much higher electron number densities, the composition from Maxwellian EEPF-based rates leads to a near-Maxwellian EEPF at these temperatures. At temperatures greater than or equal to 5,000 K, the EEPFs calculated using either compositions tend to merge. However, the copper number densities are higher for the non-Maxwellian case compared to the Maxwellian case. This results in lower E_{crit}/N for the former compared to the latter above 5,000 K, as seen from figure 5.12. Also, for 10% Cu, the breakdown field at 6,000 K is extremely small ($\sim 0.1\ Td$) for the non-Maxwellian based composition compared to the Maxwellian based composition ($\sim 10\ Td$).

Chapter 6

Plastic vapor effects

6.1 Sources and effects of plastic vapor before CZ

6.1.1 Sources of plastic vapor

One of the primary challenges in any circuit breaker design is the approach used for cooling the arc generated by the fault current and ridding the contact gap of the exhaust gases. In the case of HVCBs employed in industrial installations, a high velocity convective flow of SF_6 gas is generated by a suitable mechanism upon detecting the contact separation [105]. The convective flow is a result of a pressure gradient between a highly pressurized reservoir and a lower pressure arc chamber. Additionally, a complicated flow mechanism arising out of ablating plastic wall material is possible. Similar to a HVCB, the arc chamber of an LVCB employed for residential installations is confined within a plastic enclosure. During the high current phase when an arc with temperatures around 20,000-30,000 K is formed, plastic wall ablation is observed owing to significant radiative heating. In recent years, an additional plastic gassing insert is placed adjacent to the contacts which acts as an additional source of plastic vapor [106].

The plastic walls are usually composed of any of the following insulation materials [107]: (a) Polyethylene Terephthalate (PETP, $C_{10}H_8O_4$), (b) Polymethylmethacrylate (PMMA, $C_5H_8O_2$), (c) Polyamide-6/6 (PA-66, $C_{12}H_{22}O_2N_2$), (d) Polyvinyl chloride (PVC, C_2H_3Cl) or (e) Polytetrafluoro ethylene (PTFE, C_2F_4). There are, however, concerns regarding the by-products generated from PVC and PTFE vapors which can

be composed of hydrofluorocarbons and perfluorocarbons with extremely high global warming potential. Hence, the plastic vapors arising only out of (a)-(c) will be analyzed in the current work.

6.1.2 Effects of plastic vapor

The vaporization temperatures of most plastic materials are significantly lower than the high arc temperatures in high-current phase and hence the plastic walls are subject to evaporation. The plastic vapor arising out of the side walls is an insulator which cools the arc rapidly and quenches the excess electrons from the partially-ionized gas resulting in eventual dielectric gas formation. The former characteristic is important in the high-current phase leading to arc extinction and the latter important in the low-current or post-CZ phase for preventing re-ignition or restrike. Another desirable property in an LVCB is a low contact resistance during the life of circuit breaker, which prevents severe heating overload of the circuit breaker equipment. Shea [108] compared the performances of a ceramic and a plastic with regard to the gases released during arcing, which contribute towards an increase in contact resistance. The contact materials were the same and chosen to be Ag-W and Ag-C. Shea concluded that utilizing plastic wall material does not increase the contact resistance significantly, while the increased pressure in the arc chamber and hydrocarbon gases due to the plastic ablation improve arc interruption. Similar to the metallic particles from metal vapor, plastic vapors contribute towards the formation of carbon particles and soot during gas cooling post-CZ. Graphite is included in the list of species for equilibrium composition, but not included in the EEPF and breakdown field calculations. The number of species considered in air-metal-plastic vapor mixtures is approximately thrice that for air-metal vapor mixtures. This implies significantly greater effort required for the calculation of transport properties, which is still a work in progress and hence will not be presented in this work.

6.2 Equilibrium composition of air-copper-plastic mixtures

In this section, we focus on the composition of the three plastics PA-66, PETP and PMMA at temperatures greater than 4,000 K. The presence of condensed species,

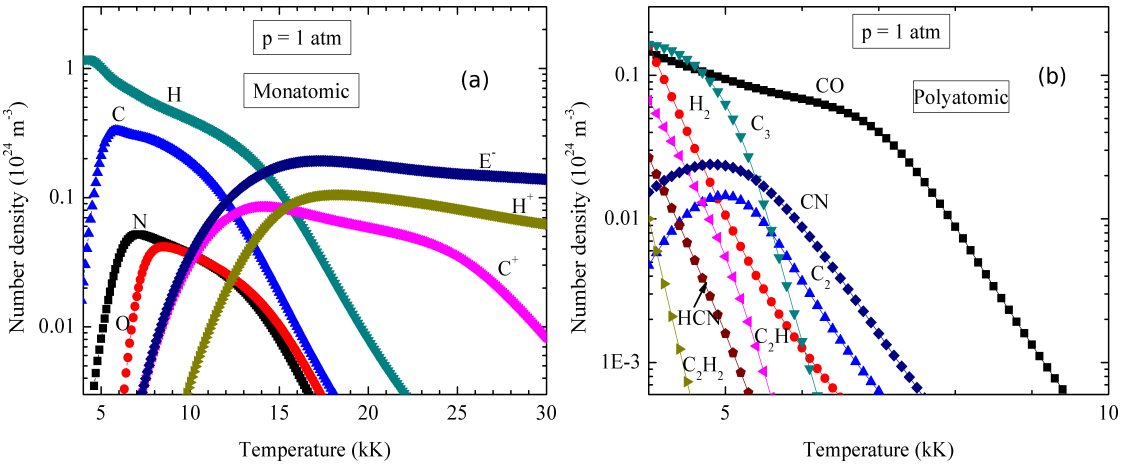

Figure 6.1: The variation of different species number densities with temperature for pure PA-66 at p = 1 *atm*: (a) monatomic and (b) polyatomic species.

graphite, at lower temperatures will be considered later. For the sake of clarity, the number densities of monatomic and polyatomic species are provided separately which renders it convenient for comparison with published data of André [109]. The number densities variation with temperature for 100% PA-66 are provided in figure 6.1. Even though the plots for the other two plastics are not provided for brevity, comparisons between the three will be mentioned in this section.

From the chemical formulae of the plastics, it can be observed that only PA-66 contains nitrogen out of the three plastics. This translates to the presence of nitrogen-based compounds, cyanide (CN) and hydrogen-cyanide (HCN) for example, in PA-66 which are totally absent in the composition of PETP and PMMA. Monatomic and di-atomic hydrogen are present in greater concentrations for PA-66 and PMMA compared to PETP. On the other hand, PETP possesses significantly higher number densities of carbon-monoxide (CO) compared to PA-66 and PMMA. PETP and PMMA generate greater number densities of monatomic oxygen compared to PA-66. The number density of diatomic carbon (C_2) initially increases and then decreases with a peak around 5,000 K for all the plastics. The number density of ethynyl radical (C_2H) for all the plastics is observed to be much higher than that of ethylene (C_2H_2), with the ratio being approximately equal to 5 at 4,000 K.

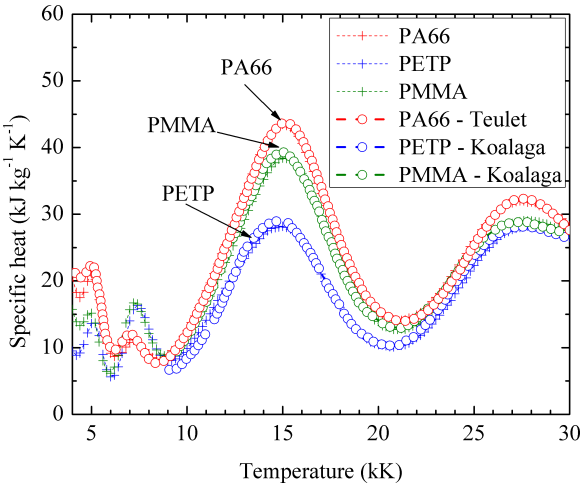

Figure 6.2: The variation of total specific heat for different plastics with temperature at atmospheric pressure. The published data are provided for PA-66 [51], PETP [110] and PMMA [110] at high temperatures.

6.3 Thermodynamic properties of air-copper-plastic mixtures

As mentioned in previous chapters, owing to its dependence on the two thermodynamic properties - density and enthalpy, specific heat is an essential thermodynamic property for validating the species composition. Figure 6.2 depicts the variation of specific heat at constant pressure with temperature for PA-66, PETP and PMMA alongside the respective published data of Teulet [51] and Koalaga [110]. The data from Koalaga for PETP and PMMA are available for temperatures above 9,000 K, while those for PA-66 from Teulet are available above 4,000 K. For PETP and PMMA at temperatures below 9,000 K, published data is available from André [109] but is not presented in the figure. The calculated specific heat (C_p) values for the plastics agree extremely well with the relevant published data. A comparison of C_p for PETP and PMMA results with those from André [109] indicates that even though the peaks are correctly observed around 5,000 K and 7,500 K, the magnitude of the peaks from his calculations are higher. On the other hand, a comparison of André's [109] PA-66 results with those from the fairly recent results of Teulet [51] at temperatures below 9,000 K indicates wide-spread discrepancies in the magnitude of the peaks at 5,000 K and 7,500 K. Since our C_p

values for PA-66 agree extremely well with those from Teulet, we conclude that André's results over-estimate the peak magnitudes for PETP and PMMA at temperatures below 9,000 K. Excellent agreement above 9,000 K is observed between all published data since most of the diatomic and polyatomic species have dissociated to form monatomic species.

In figure 6.2, the peak at around 5,000 K for PA-66 includes contributions from dissociation of triatomic carbon (C_3), C_2H, CN and C_2 while the peak at 7,000 K includes contributions from dissociation of CO and N_2. The peaks at 15,000 K and 27,500 K are owing to first ionization of monatomic carbon and hydrogen and second ionization of monatomic carbon respectively. Likewise, for PETP and PMMA, the peak at 5,000 K is from the dissociation of C_3, C_2H and C_2 while the peak at 7,000 K is owing to the dissociation of CO. The ionization peaks are from the same sources as PA-66.

6.4 Dielectric properties of air-copper-plastic mixtures

Similar to air-copper mixtures, we are interested in computing the breakdown fields in the temperature range 300-6000 K. Firstly, we choose one of the most commonly used insulation materials, PA-66, as the source of plastic vapor. It has been experimentally observed that utilizing PA-66, compared to other plastics, results in cleaner combustion and hence lower particular matter or soot formation. Next, we compare the breakdown fields for pure PA-66, PETP and PMMA. All the results provided in this section, except the breakdown fields comparison between the plastics, have been presented in our publication [111].

6.4.1 Air-copper-PA66 mixtures

Composition including condensed species

In order to validate our composition calculations, we have computed the species number densities for the case of pure PA-66 including the presence of graphite. Our results are in excellent agreement with the published data [107]. Polyatomic species with the highest mole fractions for the pure PA-66 case over the temperature range 1,000-5,000 K are

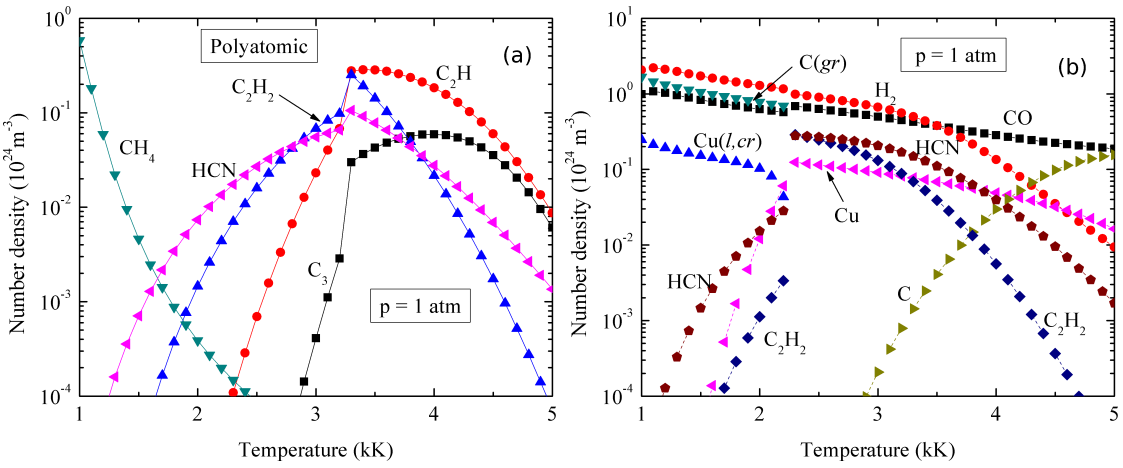

Figure 6.3: (a) The variation of polyatomic species number densities with temperature for pure PA-66, including condensed species, at p = 1 *atm*. (b) Species with high number densities for the mass fractions: 44% air, 12% Cu and 44% PA-66, including the condensed species C(*gr*) and Cu(*l,cr*).

shown in figure 6.3(a). Most importantly, we have verified with the published data that the exclusion of condensed species in the equilibrium calculations would result in over-prediction of polyatomic species number densities at temperatures lower than 3,300 *K*. The jump in number densities observed in figure 6.3(a) around 3,300 K can be attributed to the isothermal phase change of gaseous carbon (C) into graphite (C(*gr*)). Additionally, we calculate the composition corresponding to a few cases for which dielectric strength results will be presented in the next subsection. The two cases are: (i) the mass fractions of air, copper and PA-66 are 0.44, 0.12 and 0.44 respectively, (ii) the mass fractions of air, copper and PA-66 are 0.48, 0.04 and 0.48 respectively. The mass fraction values were chosen from a CFD simulation dataset [14] corresponding to two different control volumes at a particular time instant post-CZ. As part of testing the kinetics solver, the CFD data was obtained along a straight line path joining the two copper electrodes, for a simplified 2D axisymmetric geometry and a stipulated TRV profile applied post-CZ. Hence, there is no equivalent experimental setup representative of the CFD simulation. In mole fraction terms, the values for case (i) are 0.8, 0.1 and 0.1 for air, copper and PA-66 respectively and the corresponding values for case (ii) are 0.86, 0.03 and 0.11. The results corresponding to case (i) alone are presented in

figure 6.3(b) for clarity, owing to similar order of magnitude estimates between the two cases. It can be observed from figure 6.3(b) that the species number densities undergo a jump around 2,200 K owing to the phase change of the two condensed species. The condensed species of carbon and copper, C(gr) and Cu(l, cr) respectively, are marked separately in the figure. As the mass fraction of copper increases, the temperature at which the jump is observed approaches the boiling point of copper (2,835 K). A few important diatomic and polyatomic species with significant number densities are also shown in figure 6.3(b) and the jump in number densities is much more significant for the polyatomic molecules compared to the diatomic molecules.

Breakdown fields

We now present the critical electric field results for mass fraction cases (i) 0.44, 0.12, 0.44 and (ii) 0.48, 0.04, 0.48 mentioned in the previous subsection. As mentioned earlier, the ionization and attachment coefficients on the left hand side of equation (3.68) represent the summation of contributions from several species. These coefficients are calculated from ionization and attachment reaction rates respectively. The rates require the collision cross sections for the species involved in ionization or attachment reaction and the EEPF for the integration to be performed on the right hand side of equation (3.68). Apart from the ionization and attachment cross sections, electron-impact momentum transfer cross sections are also required for the drift velocity calculation in equation (3.60). In the case of pure PA-66, there are several small-chain hydrocarbon species for which experimental collision cross section for momentum transfer are not available in the literature and hence, certain approximations need to be made. For example, the cross sections for C_2H are taken to be equal to those of C_2H_2. We would like to note that even though condensed species have been included in the species composition, analyzing their effects on the EEPF are beyond the scope of current work. Hence, the EEPF and the critical electric field values are expected to be inaccurate at lower temperatures where significant condensed species number densities are observed.

Dry air is a weakly electronegative gas with O_2 being the most electronegative species and it was shown by Tanaka [50] that at temperatures greater than 3,000 K diatomic oxygen dissociated to form monatomic oxygen resulting in drastic reduction in the attachment coefficient. Also, nitric oxide contributes significantly to the ionization

coefficient at temperatures greater than 1,500 K owing to its lower ionization potential (9.25 eV) compared to other species. Moreover, addition of gaseous copper to dry air was found to significantly increase the ionization coefficient owing to its lower ionization potential (7.7 eV) [50]. Addition of PA-66 to air and copper mixture results in the addition of several hydrocarbon species which contribute to the ionization and attachment coefficients. Most of the hydrocarbon species considered possess significantly higher ionization potentials compared to copper and hence, their contribution to the ionization coefficient is expected to be negligible in the presence of high number densities of copper. However, recent experimental investigations have observed significantly high dissociative attachment cross sections at lower electron energy thresholds for HCN [112]. Hence, a high number density of HCN is expected to contribute significantly to the attachment coefficient. For a general air-Cu-PA66 mixture excluding excited species effects, we consider 31 electron-impact ionization and 19 electron attachment reactions in total corresponding to 27 different species.

An important effect previously not considered in the dielectric strength calculations [50] is that of the excited species, i.e., the effects of vibrationally-excited diatomic species and electronically-excited monatomic species on the coefficients equation (3.68) were neglected. Apart from their contribution to photo-ionization which is beyond the scope of current work, the excited species serve as an intermediate to electron-ion pair formation through step-wise ionization [43, 52]. Briefly speaking, instead of requiring a high energy electron possessing energy greater than the ionization energy of a target molecule or atom, a lower energy electron with energy higher than the targets vibrational or excitation threshold excites the target to a vibrationally- or electronically-excited state, thereby lowering the threshold for the excited targets eventual ionization. Because of their lower excitation thresholds and ionization potentials compared to diatomic species, monatomic metallic species like copper atoms are expected to contribute significantly to ionization coefficient through step-wise ionization. Also, an interesting effect with regard to diatomic hydrogen (H_2) is that: with an increase in vibrational level of ground-state H_2, electron-attachment threshold decreases by a few electron volts while the peak of electron-attachment cross section increases by approximately an order of magnitude [113]. For example, the electron-attachment thresholds for vibrational

levels n=0 and n=3 are 3.75 eV and 2.29 eV respectively, while the peak electron-attachment cross sections are 2.8×10^{-25} m^2 and 7.5×10^{-22} m^2 respectively. For a general air-Cu-PA66 mixture including excited species effects, the number of electron-impact ionization and electron attachment reactions increase from 31 and 19 to 35 and 22 respectively. Moreover, the copper mass fraction in case (ii) is three times lower than that for case (i), while the air and PA-66 mass fractions are roughly the same. Based on our equilibrium number densities calculations, this difference in copper mass fraction translates to roughly twice the number of copper atoms for case (i) compared to case (ii). The hydrocarbon number densities are roughly the same for both the cases.

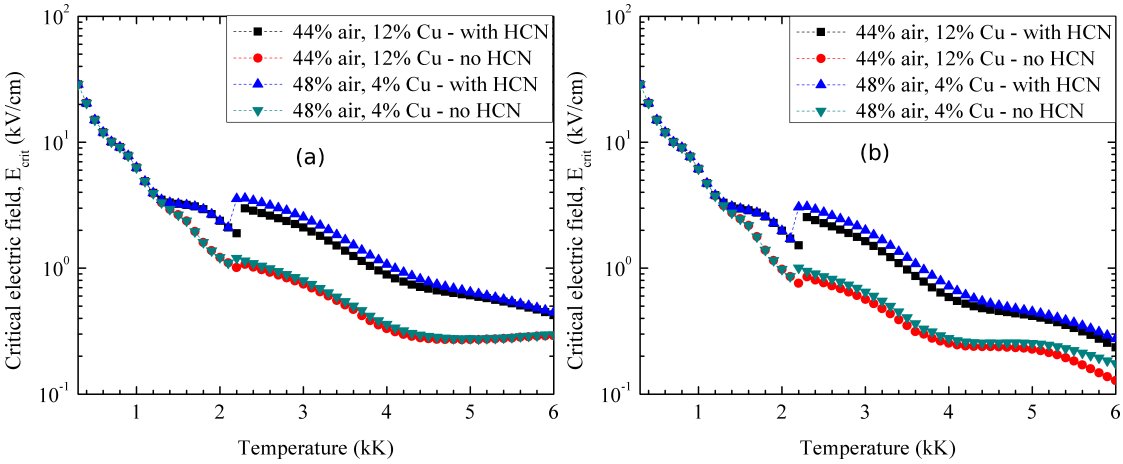

Figure 6.4: Critical electric field (E_{crit}) variation with temperature at p = 1 atm for cases (i) and (ii): (a) excluding contributions from HCN, (b) including contributions from HCN towards the attachment coefficient η.

The variation of the critical electric field (E_{crit}) over the temperature range 300-6000 K without including the excited species effects for mass fraction cases (i) 0.44, 0.12, 0.44 and (ii) 0.48, 0.04, 0.48 is depicted in figure 6.4(a). In order to substantiate the importance of HCNs contribution to attachment, the E_{crit} values with and without including HCNs attachment reaction are plotted separately in figure 6.4(a). Firstly, we comment on the effects of exclusion of condensed species for both cases. At temperatures lower than 2,200 K, copper and carbon are present in their condensed form and hence, are not included in the critical field calculations. Especially below 1,100 K, where the number densities of HCN are not significant, our calculations reproduce the breakdown field

variations with temperature for atmospheric pressure air. For example, our calculations yield an E_{crit} of approximately 30 kV/cm at 300 K for both cases, which is the breakdown field for air at ambient temperature and pressure. In the range 1,100-2,200 K, the number densities and hence the contribution to attachment coefficient of HCN increase significantly, resulting in increase in E_{crit} with the inclusion of HCNs contribution. Secondly, we comment on the effect of the difference in atomic copper number densities between cases (i) and (ii). Case (ii) is observed to have greater E_{crit} values compared to case (i) for temperatures greater than 2,200 K primarily because of having lower number densities of copper. Copper contributes the highest towards the ionization coefficient compared to other species and higher number densities of copper in case (i) result in lower E_{crit} compared to case (ii). This observation is in excellent agreement with the conclusions in published data [50]. Thirdly, we compare the effects of excluding and including HCN on E_{crit} for both cases. It can be clearly seen from figure 6.4(a) that the inclusion of HCN's attachment reaction increases E_{crit} significantly, ranging from a factor of 4 at 2,200 K to an increase of 33% at 6,000 K. Also, at temperatures greater than around 4,500 K, the decrease in contribution from copper towards the ionization coefficient results in either the increase of E_{crit} as evident from the "no HCN" plots or slower decrease of E_{crit} as evident from the with HCN plots of figure 6.4(a). The overall trend for E_{crit} is that it is decreasing with temperature, except at 2,200 K when a jump in E_{crit} is observed. This jump can be attributed primarily to the number density of HCN suddenly increasing by an order of magnitude at 2,200 K for both cases (i) and (ii), as evident from the absence of such a jump in the "no HCN" plots. The jump in HCN number densities is a direct consequence of isothermal phase change of C and Cu at 2,200 K.

Table 6.1: Critical electric field (kV/cm) vs. temperature (K) for cases (i) and (ii), excluding excited species effects.

Temp. (K)	Case(i) - no HCN	Case(ii) - no HCN	Case(i) - with HCN	Case(ii) - with HCN
1000	6.297	6.297	6.297	6.297
2000	1.217	1.217	2.377	2.377

Continued on next page

Table 6.1 – continued from previous page

Temp. (K)	Case(i) - no HCN	Case(ii) - no HCN	Case(i) - with HCN	Case(ii) - with HCN
3000	0.746	0.797	2.101	2.536
4000	0.331	0.358	0.889	1.072
5000	0.271	0.277	0.607	0.646
6000	0.291	0.297	0.428	0.445

Table 6.2: Critical electric field (kV/cm) vs. temperature (K) for cases (i) and (ii), including excited species effects.

Temp. (K)	Case(i) - no HCN	Case(ii) - no HCN	Case(i) - with HCN	Case(ii) - with HCN
1000	6.145	6.145	6.145	6.145
2000	0.982	0.982	1.982	1.982
3000	0.565	0.647	1.635	2.0
4000	0.253	0.277	0.588	0.719
5000	0.227	0.253	0.417	0.452
6000	0.128	0.175	0.235	0.275

The variation of E_{crit} with temperature including the excited species effects for cases (i) and (ii) is illustrated in figure 6.4(b). In this work, we assume that the vibrational energies for diatomic species and electronic levels of monatomic species obey the equilibrium Boltzmann distribution. The comments pertaining to E_{crit} results excluding excited species effects are valid for those including excited species. However, at temperatures greater than 3,500 K, the number densities of electronically-excited copper atoms become significant and result in an increase in the population of electrons in the high-energy tail of the EEPF through super-elastic collisions. Super-elastic collisions are those in which an electron colliding with an excited target atom or molecule attains

greater energy and de-excites the target. This results in an increase in the contribution to the ionization coefficient from copper and hence, a significantly lower E_{crit} in figure 6.4(b) compared to those in figure 6.4(a). Additionally, for temperatures in the range 2,000-3,500 K, super-elastic collisions with vibrationally-excited diatomic molecules result in reduction of E_{crit}. However, the effects of electronically-excited copper cause a greater reduction to E_{crit} compared to vibrationally-excited diatomic molecules. E_{crit} values at selected temperatures pertaining to figure 6.4(a) and figure 6.4(b) are listed in Tables 6.1 and 6.2 respectively, for convenience. By comparing the species number

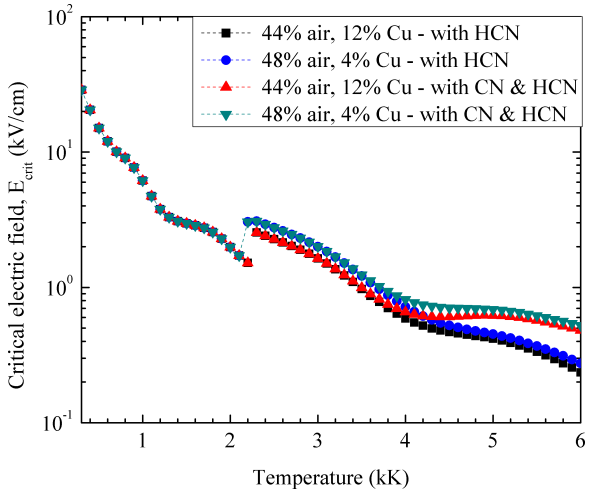

Figure 6.5: Critical electric field (E_{crit}) variation with temperature at p = 1 atm for cases (i) and (ii) including both the excited species effects and contribution from CN towards attachment coefficient η.

densities for pure PA-66 in figures 6.1(b) and 6.3(a) respectively, it can be observed that HCN begins to dissociate around 3,300 K to form CN and as a result, the number densities of CN attain a peak around 5,000 K. This observation is in general true for general air-Cu-PA66 mixtures, with the dissociation peak of HCN decreasing with decrease in % PA-66. Even though the breakdown field results in figure 6.4(b) include the important contributions from attachment and ionization coefficients from HCN and excited species respectively, the results do not include the contributions from CN towards the attachment coefficient. This is primarily because of the lack of electron-attachment cross sections for CN in the literature. If a simplifying assumption of CN possessing

the same attachment cross sections as HCN is made, the breakdown fields for both cases (i) and (ii) become significantly higher especially at temperatures above 5,000 K. A comparison between the breakdown fields in figure 6.4(b) with those including this additional contribution from CN is shown in figure 6.5. Although we expect the experimental breakdown results to be closer to the results in figure 6.5, the breakdown fields excluding the contribution from CN will be used in the next chapter for testing the kinetics solver.

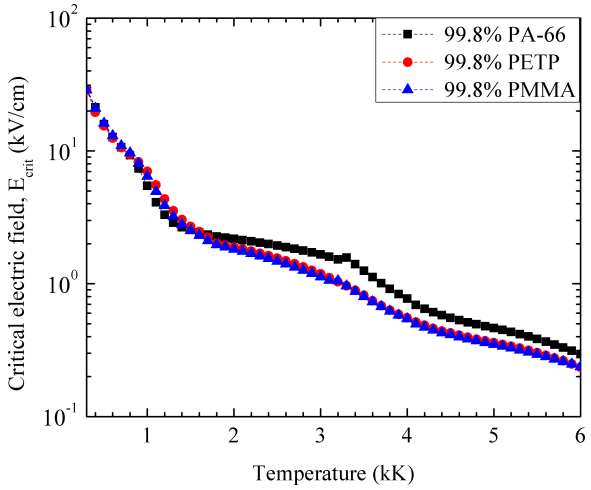

Figure 6.6: Critical electric field (E_{crit}) variation with temperature at p = 1 atm, corresponding to a mass fraction of 99.8% for PA-66, PETP and PMMA, including excited species effects.

6.4.2 Breakdown field comparison for different plastics

Apart from PA-66, there are several other plastics which have been used as enclosure materials in experiments and numerical models. In this subsection, we demonstrate the capability of our kinetics solver to compare the performances of different plastics by plotting their respective breakdown fields. From the E_{crit} values for pure PA-66, PETP and PMMA plotted in figure 6.6, it can be observed that PA-66 possesses higher breakdown fields compared to PETP and PMMA and hence, is preferable to the other plastics. While this observation is in agreement with published data [13], the current work represents the first effort to quantitatively compare the performances of plastics

in terms of their breakdown field strengths. Previous works have argued for the better performance of PA-66 on the basis of thermodynamic (C_p) or transport (σ) properties, rather than a dielectric property (E_{crit}). The primary reason for better performance of PA-66 is that among the plastics under consideration, PA-66 is the only plastic which contains nitrogen atoms and this translates to greater HCN number densities. Inclusion of the contribution from CN is expected to significantly increase the gap in E_{crit} between PA-66 and the other two plastics. Since the effects of C(gr) are not included in the EEPF and E_{crit} calculations, the results in figure 6.6 are not expected to be accurate below 3,000 K. Nonetheless, the profile observed below 3,000 K is physically acceptable, since it has been established experimentally [114, 115] that the metallic particulate contamination reduces the breakdown threshold for atmospheric pressure air gaps.

Chapter 7

Comparison with experiments

In the previous chapters, we focused on determining dielectric breakdown fields for general air-metal-plastic vapor mixtures and presented results for air-copper-PA66 mixtures. We now focus on utilizing the breakdown field results towards predicting dielectric breakdown for a known circuit breaker geometry, for which experimental results on breakdown are available post-CZ. In the pre-CZ high-current phase, the arc voltage results from the CFD solver [14] for a free burning arc were observed to be in good agreement with experiments. As a logical extension, the CFD solver was deemed appro-

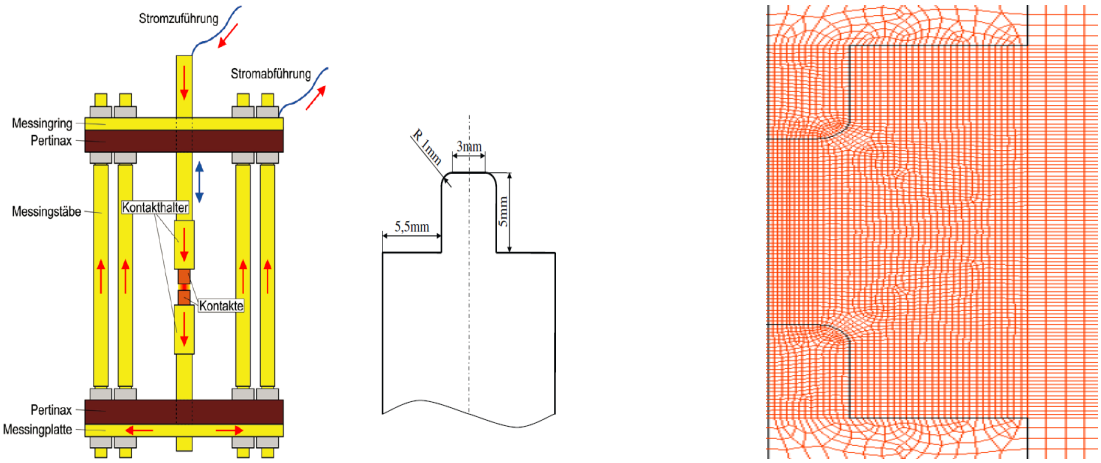

Figure 7.1: Experimental set-up with stationary electrodes and the corresponding computational mesh for a 2D axi-symmetric geometry [14].

priate to analyze fluid flow post-CZ and provide the required input data for the kinetics solver developed in current work. In addition to the CFD solver, Rümpler and his co-workers have devised experimental set-ups for studying dielectric breakdown post-CZ. Experimental results are available for a simple circuit breaker geometry shown in figure 7.1, involving air-copper mixtures without plastic wall ablation. The details regarding the experiments are provided in Rümpler's doctoral thesis [14]. In the experiments, a well-defined voltage pulse is applied across the contact gap after CZ and time at which

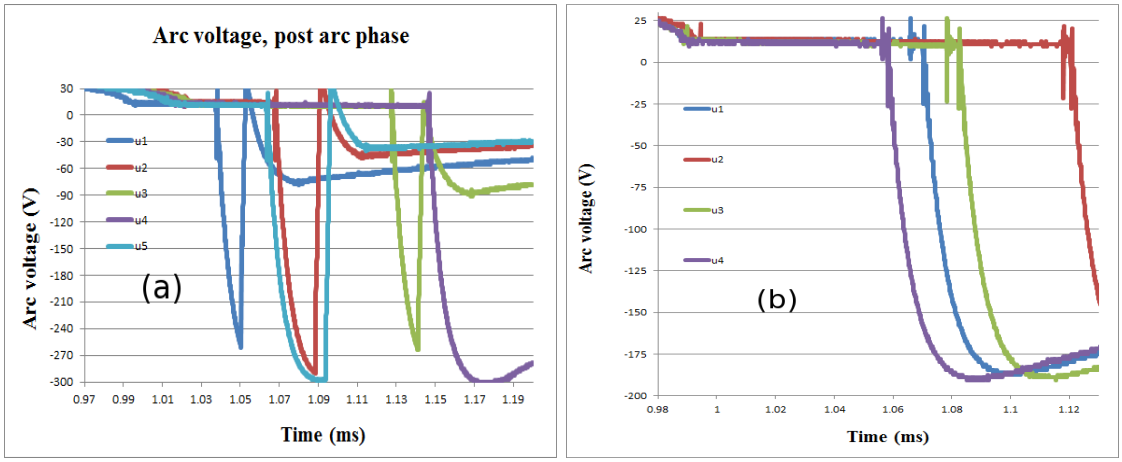

Figure 7.2: Experimental results [14] at different delay times (t_v) for the (a) Reignition and (b) Extinction cases. The delay times (in μs) post-CZ for the experiments numbered 1-4 in each case are given in table 7.1.

Table 7.1: Delay times (μs) for the experimental data in figure 7.2 for (a) Re-ignition and (b) Extinction cases.

Expt. no.	Re-ignition	Breakdown	Extinction	Breakdown
1	44.3	Yes	80.9	No
2	44.0	Yes	128.5	No
3	100.0	Yes	93.4	No
4	128.08	No	67.2	No

the spark breakdown occurs post-CZ is noted. The load voltages (U_l) across the contact gap are generated by the Surge Impulse Generator (SIP). Accordingly, numerical simulation data from a CFD set-up which closely mimics the experimental set-up is required and as a consequence, the same voltage pulse applied on the gap in the experiments is also applied after a suitable time delay as nodal voltage. The computational mesh for the CFD simulation's 2D axi-symmetric geometry is also presented in figure 7.1. In this chapter, we first briefly describe the numerical procedure utilized to generate CFD data for an equivalent experimental set-up. Elaborate descriptions of the numerical procedure are available in Rümpler's thesis [14]. Of particular interest to the current work, we then describe a simple methodology to predict dielectric breakdown for a given CFD data post-CZ and compare the numerical predictions with the experimental results.

7.1 Experimental results

Experimental results are available from Rümpler [14] for two different load voltage magnitudes: (i) $U_l = 1.2\ kV$, and (ii) $U_l = 2.0\ kV$, labeled as the "Extinction" and "Re-ignition" cases respectively for convenience. The terminology implies a greater possibility of dielectric breakdown for the "Re-ignition" case owing to the greater magnitude of the load voltage. For both the cases, the load voltages are applied after different delay times (t_v) post-CZ in order to allow for different levels of arc cooling. In general, we expect the arc temperatures to decrease with increase in the delay time.

We are particularly interested in the arc voltage profiles across the contact gap, which are provided in figure 7.2. The delay times post-CZ for application of the TRV in both cases in listed in table 7.1. Breakdown of the contact gap is characterized by the sudden collapse of arc voltage, and the time between CZ and the collapse of the arc voltage is termed the "breakdown time" (t_{br}) measured in μs. We first consider the re-ignition case. From the plots in figure 7.2(a) and data in table 7.1, it can be clearly seen that breakdown is observed for delay times lower than 100 μs while no breakdown is observed for the delay time of 128 μs. Also, it can be straight-forwardly deduced that the breakdown times (t_{br}) increase with increase in delay times (t_v). Similarly, for the extinction case in figure 7.2(b), no breakdown is observed for any of the experimental trials and the minimum delay time for which breakdown does not occur is 67.2 μs.

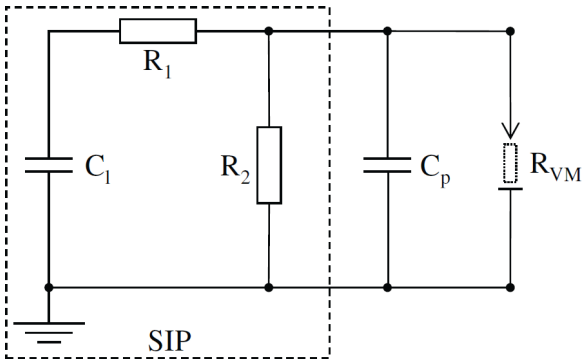

Figure 7.3: Electrical circuit including a Surge Impulse Generator (SIP) source with a parallel capacitor to generate the voltage pulse after CZ [14].

Apart from arc voltages, several transport variables are required for characterizing dielectric breakdown in the current work. It is important to note that the transport variables of interest to current work are difficult to be obtained experimentally for the entire domain, owing to the miniature contact gap. The CFD solver is expected to resolve this issue. The accuracy of the CFD solver can also be quantified by the proximity of its arc voltage results to the experimental results. The numerical arc voltage results will be presented in the next section and reasonable agreement with experimental results will be observed. Hence, as an extrapolation, the transport variables from the CFD solver are expected to closely resemble the corresponding experimental results.

7.2 Numerical procedure for CFD data

The simplified electrical circuit, corresponding to the actual experimental circuit, used for generating the CFD data post-CZ is shown in figure 7.3. The voltage pulse is generated by SIP in the measurements along with parallel capacitance C_p and the load voltage of the SIP in the actual electrical circuit is denoted by U_l. The electrical circuit for SIP has the following values: $C_l = 0.1\ \mu F$, $R_1 = 100\ \Omega$ and $R_2 = 700\ \Omega$. The contact gap is represented by a time-varying ohmic resistance. The subscript "VM" is an abbreviation for "verification mode". The following ordinary differential equations

(ODEs) for the voltages u_{C_l} and u_{C_p} are derived for this circuit [14]:

$$\begin{aligned}\frac{du_{C_l}(t)}{dt} &= -\frac{u_{C_l}(t)}{C_l R_1} + \frac{u_{C_p}(t)}{C_l R_1},\\ \frac{du_{C_p}(t)}{dt} &= \frac{u_{C_l}(t)}{C_p R_1} - \frac{u_{C_p}(t)}{C_p R_1} - \frac{u_{C_p}(t)}{C_p R_2} - \frac{u_{C_p}(t)}{C_p R_{VM}},\end{aligned} \tag{7.1}$$

This system of equations is solved with a Runge-Kutta method using the GNU Scientific Library (GSL) [116] and the solution is linked to FLUENT. The following are the steps followed by Rümpler [14] for post-arc calculation with a suitable delay time t_v:

1. **FLUENT**: Calculate arc resistance R_{VM} using the latest current and voltage values, $i_{VM}(t)$ and $u_{C_p}(t)$.

2. **FLUENT**: Solve flow problem with time step size Δt. The updated distribution of electrical conductivity (σ) can be obtained.

3. **GSL (FLUENT)**: Solve the set of ODEs with time step size Δt. The result is the voltage $u_{C_p}(t + \Delta t)$.

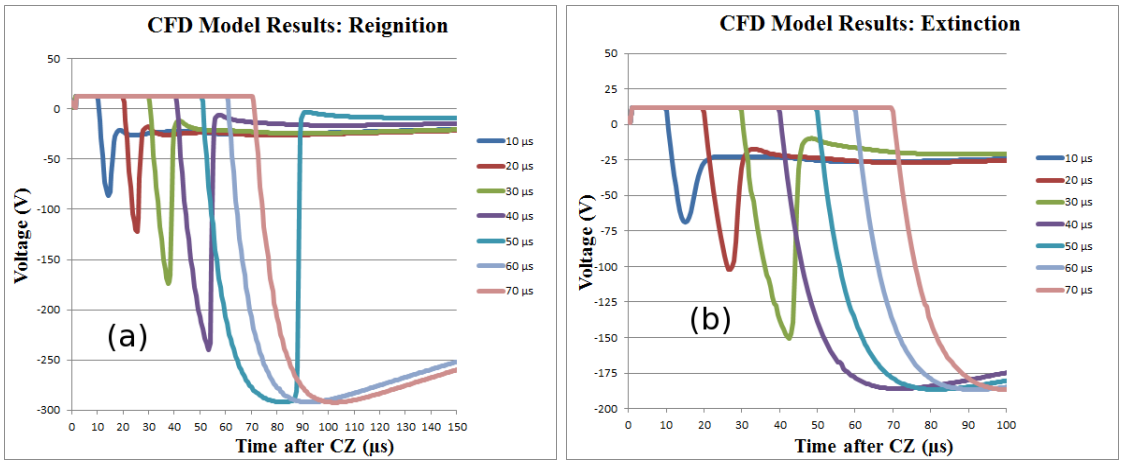

Figure 7.4: Numerical results [14] at different delay times (t_v) for the (a) Reignition and (b) Extinction cases. The delay times (in μs) post-CZ for the simulations are indicated in the legend.

4. **FLUENT**: Transfer the values $u_{C_p}(t + \Delta t)$, σ and Δt to ANSYS.

5. **ANSYS**: Calculate the electric potential for the new time using the voltage $u_{C_p}(t + \Delta t)$ as the load. Results obtained are the total current flowing through the gap $i_{VM}(t + \Delta t)$, the distribution of current density and Joule losses.

6. **ANSYS**: Transfer the values of $i_{VM}(t + \Delta t)$, current density and Joule losses back to FLUENT.

The afore-mentioned approach is an explicit coupling of the ODE solver with the calculation of the current density or electric potential and the flow solver. Therefore, small time step sizes are necessary to avoid instabilities and get a physical solution.

Numerical simulations are performed post-CZ using the CFD solver for delay times in steps of 10 μs, with the maximum delay time of 70 μs. The arc voltage results from the CFD simulations for the re-ignition and extinction cases are depicted in figure 7.4. For both the cases, the breakdown time is observed to increase with the delay time. However, the occurrence of breakdown is observed for delay times below 50 μs and 30 μs for re-ignition and extinction cases respectively. For the re-ignition case, by comparing the results in figures 7.2(a) and 7.4(a), the CFD solver predicts breakdown for delay times 40 μs and 50 μs, meaning that the CFD solver predicts breakdown at approximately 44 μs in accordance with the experimental data. Likewise, for the extinction case, the CFD solver predicts no breakdown for the 60 μs and 70 μs delay times, in accordance with the experimental observation for the intermediate value of 67 μs. Nonetheless, the CFD solver is expected to capture thermal breakdown alone and requires the breakdown field values from the kinetics solver to predict dielectric breakdown.

7.3 Breakdown prediction procedure

Formulation of the prediction procedure requires the breakdown field results from kinetics solver in addition to the transport variables from CFD solver. In this procedure, we assume that both the CFD and kinetics solvers are stand-alone or non-interacting. Using the methodology described in section 3.4, dielectric breakdown field (E_{crit}) data for air-copper mixtures in the air mass-fraction (y_{air}) range 0 to 1.0, with increments of 0.05, are calculated and stored in the form of look-up tables. It is expected that

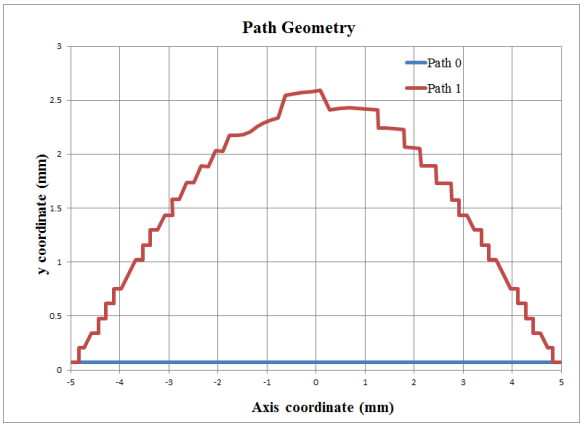

Figure 7.5: The two chosen paths from the 2D axi-symmetric geometry for which CFD simulation data are available after CZ [14]. There are 72 and 88 control volumes along path0 and path1 respectively.

the y_{air} values from the CFD solver might have general values, rather than multiples of 0.05. The breakdown fields at these intermediate y_{air} values are calculated by linear interpolation. In this section, we describe a procedure to incorporate the look-up tables from the kinetics solver into the CFD solver and predict the possibility of dielectric breakdown.

Earlier, we have defined dielectric breakdown as a successful formation of a conductive channel between the two electrodes post-CZ. In reality, the channel forms in a random 3D path between the contacts. However, the CFD solver assumes a simplified 2D axi-symmetric geometry and hence, CFD data are obtained along several 2D paths connecting the two electrodes. In this work, we present breakdown prediction results for two different paths, labeled as "path0" and "path1" respectively, shown in figure 7.5. Path0 is the center straight line of length 1 cm joining the two contacts with 72 control volumes while path1 is a curved path with 88 control volumes. Also, as seen from figure 7.4, the data for these paths are available over a time duration of 215 μs after CZ. The transport variables of interest in the atmospheric pressure air-copper mixtures considered in this section include: (i) temperature (T_h), (ii) mass fraction of air (y_{air}) and (iii) electric field (E). It is important to note that E_{crit} data at different y_{air} values are available in the temperature range 300-6,000 K. The upper limit of 6,000 K is chosen because the electron mole fractions at this temperature range between 10^{-2}-10^{-1},

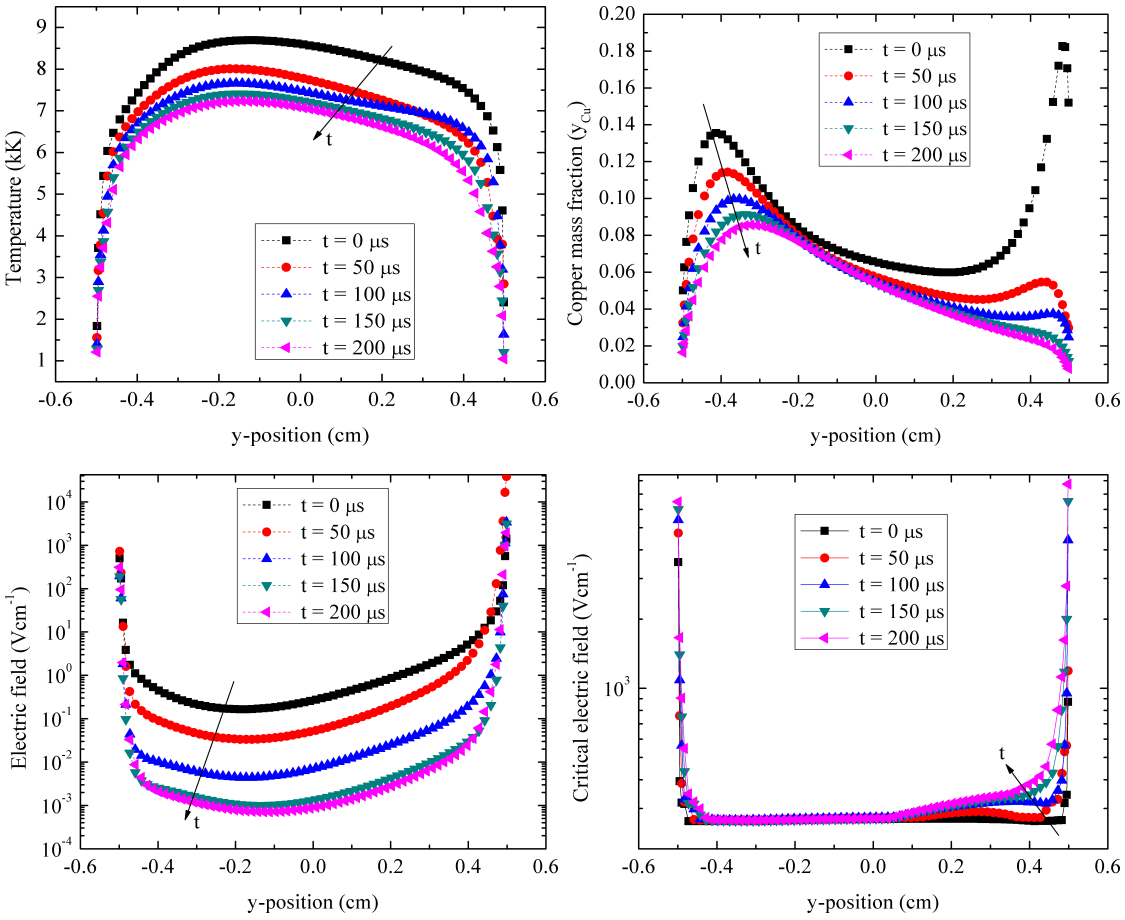

Figure 7.6: T_h and y_{Cu} variation along path0 at various time instants, for the reignition case with a delay time of 40 μs [14].

depending on the copper mole fraction. Hence, a small residual current on the order of a few milliamperes (mA) can be expected above 6,000 K. For brevity, we present the plots of important transport variable along path0 from the CFD simulation for a particular delay time. The plots of temperature, copper mass fraction, electric field and critical electric field along path0, from the CFD simulation with a delay time of 40 μs, are shown in figure 7.6. The profiles are provided from CZ till 200 μs in increments of 50 μs and the direction of the arrow represents the direction of increasing time post-CZ. As time increases, the temperatures within contact gap are observed to decrease, the

copper mass fractions near the electrodes decrease owing to diffusion losses and the electric fields in the bulk decrease. The critical electric fields are exceeded by the electric field only close to the electrodes and hence, the control volumes closest to the electrodes are susceptible to dielectric breakdown. Also, E_{crit} values not calculated above 6,000 K and hence, an additional criterion needs to be considered to overcome this limitation.

We now describe the procedure to determine if path0 is capable of forming a conductive channel and hence is susceptible to dielectric breakdown.

1. At a given time instant, the following criteria are used to label a particular control volume in the path as "conductive": (1) If the temperature (T_h) within the control volume exceeds 6,000 K. (2) If the electric field (E) in the control volume exceeds the breakdown electric field (E_{crit}) corresponding to T_h and y_{air} of the control volume.

   The first and second criterion can be considered as contributions from thermal breakdown and dielectric breakdown respectively. Using these criteria on the data plotted for path0 in figure 7.6, several control volumes in path0 are labeled conductive. However, a few control volumes remain non-conductive.

2. Sum of the lengths of conductive control volumes is determined and an "effective length", l_{eff}, equal to the difference between the total path length (1 cm) and the total conductive path length is calculated. l_{eff} is the total length of non-conductive control volumes.

   The question to be addressed next is: what are the possible effects associated with the conductive control volumes? Based on our analysis, diffusion of electrons from the conductive control volumes to neighboring control volume has time-scales on the order of a few milliseconds (ms) and hence electron diffusion is negligible in the time interval of interest. From the analysis of streamer channel in SF_6 [25], after E in a region near the cathode exceeds E_{crit}, heating of the region results in a voltage drop between the cathode and the boundary of the region. This process occurs over time-scales of tens of nanoseconds (ns) and as a consequence, the applied voltage gets re-distributed over the remaining non-conductive region between the two electrodes. We accommodate this voltage re-distribution in our breakdown prediction in the following way:

3. With the fluid-dynamic time steps on the order of 0.1 μs, CFD results available post-CZ in steps of 1 μs and the voltage re-distribution occurring on the order of ns, the re-distribution is assumed to occur instantaneously at the end of a time-step.

   The potential field needs to be re-calculated by solving the Poisson's equation in the CFD solver, but is computationally expensive. We consider a simplified alternative:

4. The total voltage across the path, V_{tot}, is determined by summing the product of electric field and control volume length over all control volumes in the path. The total voltage carried by the non-conductive control volumes, $V_{tot,nc}$, alone is calculated separately.

5. The electric field in each of the non-conductive control volumes is scaled by a factor $V_{tot}/V_{tot,nc}$.

6. Steps 1-2 are repeated with the scaled-up electric fields on the non-conductive control volumes.

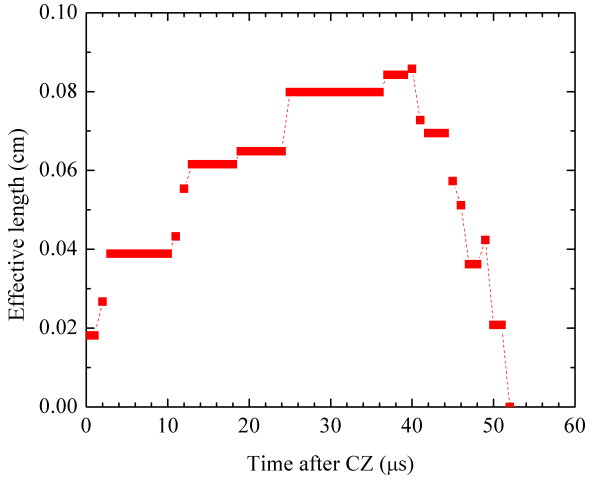

Figure 7.7: The plot of effective length (l_{eff}) variation with time, for the CFD data corresponding to the re-ignition case with 40 μs delay time. A conductive channel is successfully formed at 52.0 μs post-CZ.

7. If the re-calculated l_{eff} from step 6 equals zero, then a conductive channel has successfully formed and a breakdown is predicted. The time instant of breakdown t_{br} is also noted.

8. If l_{eff} from step 6 is non-zero, no dielectric breakdown is predicted. Steps 1-8 are then repeated for the CFD data at next time increment till either a channel is formed or the final time instant data (215 μs) from the CFD simulation.

One of the important features in the methodology presented is that the l_{eff} calculation at a given instant is independent of l_{eff} in the preceding time instants. This means that a control volume which was declared conductive in a previous time need not remain conductive in the current time instant, unless it satisfies the two criteria highlighted in step 1 at the current time. This independence from previous history can be considered to account for the stochastic nature of breakdown and can roughly be associated with the possibility of arrested leaders [25]. Using the afore-mentioned steps, we have calculated l_{eff} for the available CFD data corresponding to different delay times between 10-70 μs. For brevity, the variation of l_{eff} with time, for path0 and 40 μs delay time data in figure 7.6, is shown in figure 7.7. The effective length increases with time for approximately 40 μs and then decreases until it reaches zero at 52 μs. Hence, based on our definition, a conductive channel has successfully formed at a breakdown time of 52 μs. Curved paths, path1 for example, necessitate a slight modification to the method.

Table 7.2: Breakdown predictions for the Re-ignition case with different delay times.

Delay time	Breakdown CFD (Yes/No)	Breakdown time (μs)	Breakdown Kin (Yes/No)	Breakdown time (μs)
10.0	Yes	14.5	Yes	12.0
20.0	Yes	25.5	Yes	24.0
30.0	Yes	37.5	Yes	37.0
40.0	Yes	53.0	Yes	52.0
50.0	Yes	82.0	Yes	86.0
60.0	No	-	No	-
70.0	No	-	No	-

Table 7.3: Breakdown predictions for the Extinction case with different delay times.

Delay time	Breakdown CFD (Yes/No)	Breakdown time (μs)	Breakdown Kin (Yes/No)	Breakdown time (μs)
10.0	Yes	15.0	Yes	14.0
20.0	Yes	26.5	Yes	26.0
30.0	Yes	42.5	Yes	42.0
40.0	No	-	No	-
50.0	No	-	No	-
60.0	No	-	No	-
70.0	No	-	No	-

As seen from figure 7.5, curved paths are expected to have greater number of control volumes compared to path0 owing to their curvature. While keeping the CFD data unchanged, we consider a 1D projection of the control volumes in the curved path onto the center line (path0) as a simplification. Steps 1-8 can be carried out once the projected length for each of the control volume is calculated. In essence, our overall approach can be considered as a simplified 1D model for a given 2D data.

As mentioned earlier, the CFD simulations were performed for delay times between 10-70 μs for both re-ignition and extinction cases. Input data from the CFD solver is available for the two paths shown in figure 7.5. We have applied our methodology to each of the 14 data sets, and the results for the re-ignition and extinction cases are summarized in tables 7.2 and 7.3 respectively. It can be clearly observed from the tables that for most of the cases, the methodology (labeled "Kin") is able to predict breakdown before the eventual voltage collapse in the CFD solver. There is also agreement with the experimental data in table 7.1 that a breakdown is possible for the re-ignition case at 44 μs. Hence, we consider our methodology to be a simple but valuable first step to which further improvements can be made in a future work for better breakdown predictions. Furthermore, the methodology can also be implemented for air-copper-PA66 mixtures.

Chapter 8

Summary, Conclusions and future work

8.1 Summary

The recent trend towards miniaturization of low voltage circuit breakers has encouraged research on improving the circuit breaker's performance and longevity. One of the key factors contributing to the deterioration of performance and life of an LVCB is the occurrence of breakdown post-CZ. The weakly-ionized gas present in the contact gap post-CZ, which is a complex mixture of compressed air, metal vapor and plastic vapor, cools rapidly when a recovery voltage appears across the contacts. However, the gas mixture is generally not expected to retain its dielectric withstand capability instantaneously and hence, the formation of a conductive channel leading to a dielectric breakdown is possible. Even though controlled experimental studies have categorized breakdown distinctly into a high-temperature thermal and a low-temperature dielectric breakdown [3], breakdown in realistic circuit breakers possesses characteristics belonging to both types. By controlling the appearance of the TRV post-CZ using a stipulated delay time, experiments have shown that thermal breakdown can occur within a few μs post-CZ while dielectric breakdown can occur after a few hundreds of μs post-CZ. In this work, we are interested in analyzing dielectric breakdown once a successful thermal interruption has occurred. Since the pressure within the circuit breaker geometry is on the order of atmospheric pressure and the gap length is on the order a few cm, the

dielectric breakdown has a closer resemblance towards a streamer breakdown rather than a Townsend breakdown. One of the major drawbacks of experimental set-ups is the lack of repeatability of breakdown results, since breakdown is inherently a stochastic process. Also, the set-ups can be both time-consuming and expensive. Hence, numerical modeling is imperative for understanding the important features of dielectric breakdown and developing a simplified dielectric breakdown prediction model has been the primary objective of this research work.

Numerical studies on breakdown have been predominantly directed towards high voltage circuit breakers employing SF_6 gas. However, in the past decade, a shift towards utilization of compressed gases with lower global warming potential has been explored. In particular, compressed air has been considered as a candidate for dielectric fluid in an LVCB. We have avoided the approach of tracking a nanosecond time-scale streamer, which leads to a spark breakdown, because of computational constraints associated with this approach for complex gas mixtures. Some of the earlier work on breakdown in an LVCB [13,51] have addressed thermal breakdown, by considering electrical conductivity profiles and arguing that the regions of high electrical conductivity have a greater probability of breakdown. Rümpler [14] has devised a CFD solver for tracking plasma arc motion and its eventual extinction within the LVCB's splitter plates close to CZ. The CFD solver, which is capable of capturing thermal breakdown, obtains transport variables by considering a "one-fluid" formulation for air-metal-plastic vapor mixtures, while assuming local thermodynamic equilibrium. The kinetics solver developed in this work considers several non-equilibrium effects, extracts relevant input from the CFD solver and predicts the possibility of a conductive channel formation leading to dielectric breakdown.

In this dissertation, we have developed a generalized framework for predicting dielectric breakdown in an LVCB involving air, metal and plastic vapor mixtures. Importantly, this framework enables performance comparisons between different metal and plastic vapors. The most important contribution from current work is the computation of dielectric breakdown fields (E_{crit}) for gas mixtures employed in an LVCB. E_{crit} depends upon the following inputs from the CFD solver: (i) temperature, (ii) pressure and (iii) mass fractions of air (y_{air}), metal vapor (y_{metal}) and plastic vapor ($y_{plastic}$). The temperature range of interest is 300-6,000 K and the solver assumes

thermal breakdown above 6,000 K owing to high electron number densities. At temperatures below 2,500 K, metallic droplets and particles are observed within an LVCB. Even though condensed species are included in the species composition calculations, their effects on E_{crit} are neglected in the current work. Some of the important non-equilibrium effects considered in E_{crit} calculation include: (i) non-Maxwellian EEPF which is a direct consequence of the TRV, (ii) vibrationally- and electronically-excited species and (iii) finite-rate chemical reactions. The non-Maxwellian EEPF is obtained from a Boltzmann-equation solver [19], which requires electron-impact collision cross sections for elastic and inelastic processes as input. Some of the electron-impact inelastic collisions under consideration in current work include (a) vibrational excitation, (b) electronic excitation, (c) super-elastic collisions which result in de-excitation of excited species, (c) ionization and (d) attachment. We have extensively validated our code by comparing our results with published data for: (i) equilibrium composition of air-copper mixtures [50], (ii) equilibrium composition of PA-66 [107], and (iii) E_{crit}/N results for air-copper mixtures [50]. An important parameter of concern in E_{crit} calculations is the electron-impact momentum-transfer cross section of the metal vapor. There are several standard databases available for these cross sections and hence, careful validation is required before finalizing the cross section data. The accuracy of transport properties depend upon the accuracy of collision integrals, which in turn depend upon the momentum transfer cross sections. Hence, we have validated our momentum transfer cross section data of metal vapor by obtaining good agreement for our transport property results with the published data. Finally, we have proposed a simplified methodology to predict dielectric breakdown, by assessing the possibility of a conductive channel formation along different paths between the two electrodes. The predictions from this methodology are compared with available experimental data for air-copper mixtures.

8.2 Conclusions

This research work was commissioned with the primary objective of quantifying dielectric breakdown in an LVCB containing complex gas mixtures post-CZ. A few of the expected outcomes included identifying: (i) important species, (ii) reactions and (iii) possible hot-spots within an LVCB. During the course of pursuing the objective

and outcomes, we have taken into account realistic non-equilibrium effects which contribute significantly to enhance or suppress dielectric breakdown. We have highlighted the importance of these effects on the calculation of critical electric field, E_{crit}, for air-copper-PA66 mixtures. We regard this effort as the first attempt to quantify E_{crit} for general air-metal-plastic vapor mixtures. E_{crit} is calculated by tallying the contribution of individual species towards ionization (α) and attachment coefficients (η), with the coefficients depending upon the general non-Maxwellian EEPF. Air as a dielectric fluid is weakly electronegative with diatomic oxygen being the chief contributor to its electronegativity. We have validated with published data [50] that metal vapors in air drastically reduce E_{crit} by virtue of their lower ionization energies. Through our transport property calculations for air-copper mixtures, we have verified that an important consequence of low ionization energy is higher electrical conductivity at moderate temperatures 5,000-10,000 K [86]. Also, excluding the effects of electron super-elastic collisions with vibrationally-excited diatomic species (N_2, O_2) and electronically-excited monatomic species (Cu) engenders an over-estimation of the published E_{crit} values [50]. This is because the super-elastic collisions generate greater population of high energy electrons, thereby increasing α and decreasing E_{crit}. Including super-elastic collisions also leads to a correct Maxwellian EEPF at very small electric fields. For air-copper mixtures, we have also studied the effects of finite-rate kinetics on E_{crit} for a temperature decay from 8,000 K to 2,000 K, corresponding to different constant cooling rates 10^7 K/s and 10^8 K/s. The cooling rate of 10^8 K/s is usually observed in approximately the first 10-20 μs of temperature decay while the slower rate of 10^7 K/s is observed for the next several 100 μs. We have presented the comparison of E_{crit} values using (i) chemical equilibrium, (ii) Maxwellian EEPF based reaction rates and (iii) non-Maxwellian EEPF based reaction rates at different time instants, for the 10^8 K/s cooling rate and a TRV of 400 V appearing instantaneously across the contact gap of 2 cm. It is worth noting that the non-Maxwellian EEPF is a direct consequence of the appearance of TRV and the difference in E_{crit} values calculated using (ii) and (iii) are primarily due to the TRV. The electron and monatomic species decay slowly in the chemical non-equilibrium case and hence, their number densities are higher compared to the equilibrium composition. The E_{crit} values with the finite-rate reaction composition can be higher or lower than those using equilibrium composition, depending upon the temperature range of interest.

This conclusion is true for any given mass-fraction of copper (y_{Cu}).

The addition of plastic vapor results in a nearly three-fold increase in the total number of species. Plastic vapor has been observed to rapidly cool the arc prior to CZ and some of the earlier works [13] have related better post-arc interruption characteristics of a plastic vapor with its lower electrical conductivity. In this thesis, we have established that better interruption capability of PA-66 is a consequence of its higher E_{crit} compared to the other plastics - PETP and PMMA. Unlike PETP and PMMA, PA-66 contains nitrogen in its formula. From the equilibrium composition of the three plastics, PA-66 was observed to generate greater number densities of nitriles - CN and HCN compared to PETP and PMMA. HCN possesses high electron attachment cross sections for the dissociative-attachment collision process: $HCN + E^- \rightarrow H + CN^-$ [112]. This reaction contributes significantly towards η, resulting in high E_{crit} for PA-66. At temperatures above 3,000 K, HCN begins to dissociate to form the cyano radical (CN). Since CN has an extremely high electron affinity of 3.862 eV, there exists a high probability of direct electron attachment to CN to form a stable cyanide anion CN^-. Unfortunately, electron-impact attachment cross sections for CN are unavailable in the literature and hence, contributions from CN to η were neglected in E_{crit} calculations for pure plastics. On the other hand, if we assume that CN has the same electron-attachment cross sections as HCN and include its contribution to η, the E_{crit} values are considerably higher compared to the case where CN's contribution to η was neglected. The effects of finite-rate kinetics on E_{crit} with the inclusion of plastic vapor will be taken up in a future work.

Using the kinetics solver developed in this work, look-up tables for breakdown fields were generated for different pressures, temperatures and mass fractions of air, metal vapor and plastic vapor. The temperature range of interest for E_{crit} in this work is 300-6,000 K. Electron mole fractions in the range 0.01-0.1 are possible for gas temperatures above 6,000 K, leading to a small residual current flow. Experimental data on arc current and arc voltage are available for a simple circuit breaker geometry containing an air-copper mixture, with the contact gap subjected to two different TRV magnitudes - (i) 1.2 kV and (ii) 2.0 kV. The two cases are labeled as "Extinction" and "Re-ignition" for convenience. Breakdown is characterized by a sudden collapse of the arc voltage and time after CZ at which the voltage collapses is termed the breakdown time,

t_{br} (μs). The experimental t_{br} values are noted for the TRVs applied with a delay time of several μs post-CZ. The numerical breakdown prediction model developed in this thesis requires both the stand-alone CFD and kinetics solvers, with the kinetics solver obtaining the transport variables from CFD solver. Transport variables, especially the temperature and electric field, are difficult to be measured for the experimental set-up. Hence, the transport variable data is obtained from the CFD solver by extending the simulation time interval to a few ms post-CZ and applying the same TRVs across the contacts as the experiments. The breakdown in realistic circuit breakers possesses characteristics of both thermal and dielectric breakdown. The CFD solver is capable of predicting thermal breakdown, but incapable of capturing dielectric breakdown. In this work, we characterize breakdown by the formation of a conductive channel formation between the metallic contacts and we have devised a simple methodology to predict the channel formation. The CFD transport data is available for two specific paths, stored in time intervals of 1 μs till 215 μs post-CZ, and delay times in the range 10-70 μs in increments of 10 μs. Hence, for each of re-ignition and extinction cases, there are 14 datasets in total (7 for each path), with each containing 216 time instant data for transport variables. For a given path-delay time combination and its corresponding data at each stored time, a control volume along the path where: (a) E exceeds E_{crit} and (b) T exceeds 6,000 K are marked as "conductive". Criteria (a) and (b) pertain to dielectric and thermal breakdown respectively. The total length of non-conductive control volumes, l_{eff}, is calculated. A simple voltage re-scaling is performed for the non-conductive control volumes at that time instant and the criteria (a) and (b) are implemented again. If l_{eff} after the voltage re-scaling and re-application of breakdown criteria is non-zero, we conclude that no conductive channel is formed and vice-versa. Breakdown occurs for the experimental re-ignition case with a 44 μs delay time, and our methodology predicts breakdown for CFD input corresponding to 40 μs and 50 μs. Likewise, no breakdown occurs for the experimental extinction case with a 67 μs delay time, and our methodology predicts no breakdown for CFD input corresponding to 60 μs and 70 μs. Also, our approach predicts the breakdown a few μs earlier than the arc voltage collapse is observed in the CFD solver, meaning that shorter breakdown times are observed with our approach compared to the CFD solver. With these agreements with experimental data, our simple methodology can be considered a valuable first

step towards breakdown prediction and we intend to introduce stochasticity into the methodology in future. In reality, the leader formation and propagation leading to the dielectric breakdown have a stochastic nature [35]. Furthermore, our methodology will be examined for air-copper-PA66 related experimental data which are expected to be available in the near future.

8.3 Directions of future work

Possible improvements to our solver as part of immediate future work are first discussed briefly. These enhancements will be assigned a high priority.

8.3.1 Condensed species effects on EEPF

In the current work, we neglect the effects of condensed species on EEPF and hence the E_{crit} values obtained using the EEPF are expected to be inaccurate at temperatures below 3000 K. We expect to improve the accuracy of the EEPF and E_{crit} at lower temperatures where the number densities of crystalline copper and/or graphite are expected to be significant. In a low pressure argon plasma with particulate matter [117], the populations in low-energy region of the EEPF are higher compared to that for a pristine plasma. This is primarily the result of high momentum-transfer cross sections of the particle, leading to greater energy losses through elastic collisions. Denysenko *et al.* [118] provide evidence of greater populations in the high-energy tail and lower populations in the mid-energy portion, with the former owing to increase in the electric field sustaining the plasma and the latter resulting from Maxwellization of the EEPF through electron-dust collisions. In our future work, the particle size distribution will be assumed to be mono- disperse with a size 1 μm. The charge on the particle needs to be determined, for which the approach of Gatti [119] in the high-collisionality regime will be considered. To obtain the steady-state EEPF, the Boltzmann equation solver will be provided the additional inputs: momentum transfer and attachment cross sections for electron-dust collisions.

8.3.2 Stochastic breakdown methodology

Based on breakdown field results from current work, we expect the air-metal-plastic vapor mixture to exhibit breakdown characteristics similar to SF_6. In this work, we employed a simplified methodology to predict the possibility of breakdown without considering whether the conductive channel attains the transition from a streamer to a leader. Even though it has not yet been verified from experiments, we surmise that the initial streamer originates from a metallic/carbon micro-protrusion on the breaker surface. For a quiescent SF_6 gas between a 2 *cm* contact gap, Seeger and his co-workers [25,35] have developed a stochastic model addressing breakdown at protrusions while considering leader propagation. We are currently working to incorporate Seeger's stochastic model into our methodology for an accurate breakdown prediction. However, the stochastic model requires several parameter fits from experimental data, which are expected to be obtained from on-going experimental investigations for air-copper-PA66 mixtures.

8.3.3 Modifications to CFD solver

Using a two-temperature NLTE approach for a thermal plasma spraying application, Trelles [21] has observed excellent agreement with experimental arc voltage values. The CFD solver is expected to be updated to address kinetic non-equilibrium through the addition of an electron enthalpy conservation equation. An additional modification to the CFD solver will be conversion from the "one-fluid" formulation to a multi-species formulation. Instead of considering air and metal vapor as separate components, the solver could be updated to consider multiple species-conservation equations alongside momentum and energy equations. Even though this approach makes it easier to incorporate chemical non-equilibrium owing to finite-rate kinetics, an upper limit of 50 species conservation equations exists in ANSYS/FLUENT. Hence, the multi-species formulation can only be tested for air-metal vapor mixtures rather than air-metal-plastic vapor mixtures. The right hand side of a species conservation equation contains a net generation term due to chemical reactions, which can be obtained straight-forwardly from the kinetics solver developed in this work.

8.3.4 Transport properties including plastic vapor

LTE thermodynamic and transport properties for air-metal vapor mixtures have been calculated in this work using Devoto's approach [66, 72]. The next major update required is the calculation of transport properties including plastic vapor. Thermodynamic properties of different plastic vapors computed in current work were observed to be in excellent agreement with the published data, meaning that the equilibrium composition is highly accurate. There are 77 species in total for air-metal-plastic vapor mixtures and hence, polarizability and Lennard-Jones parameters required for the collision integral calculations need to be gathered from literature. In case the CFD solver is modified to consider two-temperature non-equilibrium, the transport properties need to be calculated using the accurate method of Rat *et al.* [22].

8.3.5 Finite-rate kinetics including plastic vapor

In this thesis, comparison of breakdown fields between chemical equilibrium and non-equilibrium compositions for air-copper mixtures in the temperature range 2,000-6,000 K was presented. The condensed species effects were neglected in the reaction mechanism and hence, one of the possible improvements in future will be to include solid-gas reaction kinetics. A similar effort is expected to be performed in future with the inclusion of plastic vapor. The computational effort is expected to increase substantially arising from a three-fold increase in the number of species. However, reaction mechanisms resulting in soot formation from carbon clustering will be beyond the scope of future work.

The following improvements will be considered in the long term and assigned a lower priority.

8.3.6 Plasma sheath dynamics

In a high-temperature plasma, a plasma sheath with a thickness of few μm forms adjacent to electrode walls. Capturing plasma-sheath effects in a circuit breaker requires extremely small grid sizes close to the wall, which increases computational time manyfold. A zero-dimensional plasma sheath model has been considered in the CFD solver [14].

However, as the plasma cools post-CZ, the cathode sheath is expected to slightly expand depending on the bulk temperature. During the expansion, the metallic electrodes can be expected to evaporate accompanied by a release of metal vapor. An accurate expanding plasma sheath model with metal vapor emanating from the electrode surface needs to be developed and smoothly stitched to the weakly-ionized bulk. This effort will improve the accuracy of simulation results since the TRV is expected to be sustained mostly by the cathode sheath.

8.3.7 Turbulence effects

Fluid flow within the contact gap post-CZ is highly turbulent. The turbulence is mostly a consequence of the circuit breaker geometry and is further enhanced by surface roughness of the electrodes and circuit breaker walls. Experiments confirm the presence of turbulent re-circulation regions which enhance mixing between hotter and colder eddies within the contact gap. High rates of heat and mass transfer are the fundamental characteristics of turbulent flows [120]. The grid resolution in the CFD solver needs to be increased to accurately capture the effects of turbulence. Direct numerical solution (DNS) of thermal plasma is prohibitive because the high Reynolds numbers require extremely high grid resolution. However, large eddy simulation (LES) alleviates this limitation by considering coarser grid resolutions compared to DNS and using sub-grid scale models [21] to approximate the effects of small-scales on the larger eddy scales. If numerical instabilities are observed while using ANSYS/FLUENT, a complete migration to the open-source platform OpenFOAM [30] will be attempted. Nonetheless, LES is computationally expensive and hence Reynolds-averaged Navier-Stokes (RANS) or Prandtl mixing length models [28] might also be examined.

References

[1] Garzon, R.D., 2002. *High voltage circuit breakers: Design and applications*, Marcel Dekker Inc., New York.

[2] Rümpler, C., & Zacharias, A., 2007. Simulation of the switching arc for a motor protective circuit breaker. *Proceedings of Fraunhofer SCAI MpCCI user forum*, 62–69.

[3] Shea, J.J., 2001. The influence of arc chamber wall material on arc gap dielectric recovery voltage. *IEEE Transactions on Components and Packaging Technologies*, 24, 342–348.

[4] Llewellyn-Jones, F., 1983. *The Development of Theories of the Electrical Breakdown of Gases*, NATO ASI Series - Electrical breakdown and discharges in gases: Part A - Fundamental Processes and Breakdown, 89a, 1–71.

[5] Brown Jr., T.E., 1984. *Circuit interruption: theory and techniques*, Marcel Dekker Inc., New York.

[6] Schade, E., & Ragaller, K., 1982. Dielectric recovery of an axially blown SF_6-arc after current zero: Part I - Experimental investigations. *IEEE Transactions on Plasma Science*, 10, 141–153.

[7] Brand, K.P., Egli, W., Niemeyer, L., Ragaller, K., & Schade, E., 1982. Dielectric recovery of an axially blown SF_6-arc after current zero: Part III - Comparison of Experiment and Theory. *IEEE Transactions on Plasma Science*, 10, 162–172.

[8] Brand, K.P., & Kopainsky, J., 1978. Particle densities in a decaying SF_6 plasma. *Applied Physics*, 16, 425–432.

[9] Ragaller, K., Egli, W., & Brand, K.P., 1982. Dielectric recovery of an axially blown SF_6-arc after current zero: Part II - Theoretical investigations. *IEEE Transactions on Plasma Science*, 10, 154–162.

[10] Pietronero, L., & Wiesmann, H.J., 1984. Stochastic model for dielectric breakdown. *Journal of Statistical Physics*, 36, 909–916.

[11] Lindmayer, M., Marzahn, E., Mutzke, A., Ruther, T., & Springstubbe, M., 2006. The process of arc splitting between metal plate in low voltage arc chutes. *IEEE Transactions on Components and Packaging Technologies*, 29, 310–317.

[12] Rong, M., Yang, F., Wu, Y., Murphy, A.B., Wang, W., & Guo, J., 2010. Simulation of arc characteristics in miniature circuit breaker. *IEEE Transactions on Plasma Science*, 38, 2306–2311.

[13] Teulet, Ph., Gonzalez, J.J., Mercado-Cabrera1, A., Cressault, Y., & Gleizes, A., 2009. One-dimensional hydro-kinetic modelling of the decaying arc in air-PA66-copper mixtures: II. Study of the interruption ability. *Journal of Physics D: Applied Physics*, 42, 185207 1–10.

[14] Rümpler, C., 2009. *Lichtbogensimulation für Niederspannungsschaltgeräte*, Ph.D. dissertation, Technischen Universität Ilmenau, Germany.

[15] Kee, R.J., Rupley, F.M., Meeks, E., & Miller, J.A., 1996. *CHEMKIN-III: A FORTRAN chemical kinetics package for the analysis of gas-phase chemical and plasma kinetics*, Technical Report: SAND96-8216, Sandia National Laboratories, California.

[16] Brown, P.N., Byrne, G.D., & Hindmarsh, A.C., 1989. VODE: a variable-coefficient ODE solver. *SIAM Journal on Scientific and Statistical Computing*, 10, 1038–1051.

[17] Mott, D.R., & Oran, E.S., 2001. *CHEMEQ2: A solver for the stiff ordinary differential equations of chemical kinetics*, Technical Report: NRL/MR/6400–01-8553, Naval Research Laboratory, Washington DC.

[18] Morgan, W.L., & Penetrante, B.M., 1990. ELENDIF: A time-dependent Boltzmann solver for partially ionized plasmas. *Computer Physics Communications*, 58, 127–152.

[19] Hagelaar, G.J.M., & Pitchford, L.C., 2005. Solving the Boltzmann equation to obtain electron transport coefficients and rate coefficients for fluid models. *Plasma Sources Science and Technology*, 14, 722–733.

[20] Pancheshnyi, S., Eismann, B., Hagelaar, G.J.M., & L.C. Pitchford, L.C., 2008. *Computer code ZDPlasKin*, http://www.zdplaskin.laplace.univ-tlse.fr, University of Toulouse, LAPLACE, CNRS-UPS-INP, Toulouse, France.

[21] Trelles, J.P., 2007. *Finite element modeling of flow instabilities in arc plasma torches*, Ph.D. dissertation, University of Minnesota, USA.

[22] Rat, V., André, P., Aubreton, J., Elchinger, M.F., Fauchais, P., & Lefort, A., 2001. Transport properties in a two-temperature plasma: Theory and application. *Physical Review E*, 64, 026409 01–20.

[23] Rat, V., André, P., Aubreton, J., Elchinger, M.F., Fauchais, P., & Vacher, D., 2002. Transport coefficients including diffusion in a two-temperature argon plasma. *Journal of Physics D: Applied Physics*, 35, 981–991.

[24] Ghorui, S., Heberlein, J.V.R., & Pfender, E., 2007. Non-equilibrium modelling of an oxygen-plasma cutting torch. *Journal of Physics D: Applied Physics*, 40, 1966–1976.

[25] Seeger, M., Niemeyer, L., & Bujotzek, M., 2008. Partial discharges and breakdown at protrusions in uniform background fields in SF_6. *Journal of Physics D: Applied Physics*, 41, 185204 01–14.

[26] Latham, R.V., 1995. *High Voltage Vacuum Insulation: Basic Concepts and Technological Practice*, Academic Press Limited, San Diego.

[27] Frind, G., & Rich, J.A., 1974. Recovery speed of axial flow gas blast interrupter: dependence on pressure and dI/dt for air and SF_6. *IEEE Transactions on Power Apparatus and Systems*, 93, 1675–84.

[28] Gonzalez, J.J., Girard, R., & Gleizes, A., 2000. Decay and post-arc phases of a SF_6 arc plasma: a thermal and chemical non-equilibrium model. *Journal of Physics D: Applied Physics*, 33, 2759–68.

[29] FLUENT Inc., 2006. *Fluent User's Manual 6.3.26*, http://www.ansys.com, NH, USA.

[30] OpenCFD Ltd., 2011. *OpenFOAM User Guide 2.2*, http://www.openfoam.com/, Bracknell, UK.

[31] Slepian, J., 1928. Extinction of an A-C. Arc. *Transactions of the American Institute of Electrical Engineers*, 47, 1398–1407.

[32] Pedersen, A., 1970. Criteria for Spark Breakdown in Sulfur Hexafluoride. *IEEE Transactions on Power Apparatus and Systems*, 89, 2043–2048.

[33] Pedersen, A., 1975. The effect of surface roughness on breakdown in SF_6. *IEEE Transactions on Power Apparatus and Systems*, 94, 1749–1754.

[34] Seeger, M., Naidis, G., Steffens, A., Nordborg, H., & Claessens, M., 2005. Investigation of the dielectric recovery in synthetic air in a high voltage circuit breaker. *Journal of Physics D: Applied Physics*, 38, 1795–1804.

[35] Seeger, M., Niemeyer, L., & Bujotzek, M., 2009. Leader propagation in uniform background fields in SF_6. *Journal of Physics D: Applied Physics*, 42, 185205 01–11.

[36] Seeger, M., Schwinne, M., Bini, R., Mahdizadeh, N., & Votteler, T., 2012. Dielectric recovery in a high-voltage circuit breaker in SF_6. *Journal of Physics D: Applied Physics*, 45, 395204 01–12.

[37] Hartmann, G., & Gallimberti, I., 1975. The influence of metastable molecules on the streamer progression. *Journal of Physics D: Applied Physics*, 8, 670–680.

[38] Lowke, J.J., 1992. Theory of electrical breakdown in air - the role of metastable oxygen molecules. *Journal of Physics D: Applied Physics*, 25, 202–210.

[39] Lowke, J.J., & Morrow, R., 1994. Theory of electric corona including the role of plasma chemistry. *Pure and Applied Chemistry*, 66, 1287–1294.

[40] Lowke, J.J., & D'Alessandro, F., 2003. Onset corona fields and electrical breakdown criteria. *Journal of Physics D: Applied Physics*, 36, 2673–2682.

[41] Simek, M., Clupek, M., Babicky, V., & Sunka, P., 2006. Production of reactive species by atmospheric pressure streamers in N_2-O_2 mixtures. *Pure and Applied Chemistry*, 78, 1213–1225.

[42] Mnatsakanyan, A.K., & Naidis, G.V., 1991. Charged particle production and loss processes in nitrogenoxygen plasmas. *Reviews of Plasma Chemistry*, 1, 259–292.

[43] Naidis, G.V., 1999. Simulation of streamer-to-spark transition in short non-uniform air gaps. *Journal of Physics D: Applied Physics*, 32, 2649–2654.

[44] Kossyi, I.A., Kostinsky, A.Y., Matveyev, A.A., & Silakov, V.P., 1992. Kinetic scheme of the non-equilibrium discharge in nitrogen-oxygen mixtures. *Plasma Sources Science and Technology*, 1, 207–220.

[45] Starik, A.M., N.S. Titova, N.S., & Arsentiev, I.V., 2010. Comprehensive analysis of the effect of atomic and molecular metastable state excitation on air plasma composition behind strong shock waves. *Plasma Sources Science and Technology*, 19, 1–23.

[46] Tanaka, Y., 2004. Prediction of dielectric properties of N2/O2 mixtures in the temperature range of 3003500K. *Journal of Physics D: Applied Physics*, 37, 851–859.

[47] Shea, J.J., 2002. Dielectric recovery characteristics of a high current arcing gap. *IEEE Transactions on Components and Packaging Technologies*, 25, 402–408.

[48] Shea, J.J., 2004. Gassing arc chamber wall material effect on post current-zero recovery voltage breakdown. *IEEE Transactions on Components and Packaging Technologies*, 27, 42–50.

[49] Shea, J.J., & Zhou, X., 2006. Contact material and arc current effect on post-current zero contact surface temperature. *IEEE Transactions on Components and Packaging Technologies*, 29, 286–293.

[50] Tanaka, Y., 2005. Influence of copper vapor contamination on dielectric properties of hot air at 300-3500 K in atmospheric pressure. *IEEE Transactions on Dielectrics and Electrical Insulation*, 12, 504–512.

[51] Teulet, Ph., Gonzalez, J.J., Mercado-Cabrera1, A., Cressault, Y., & Gleizes, A., 2009. One-dimensional hydro-kinetic modelling of the decaying arc in airPA66copper mixtures: I. Chemical kinetics, thermodynamics, transport and radiative properties. *Journal of Physics D: Applied Physics*, 42, 175201 1–15.

[52] Luque, A., Ratushnaya, V., & Ebert, U., 2008. Positive and negative streamers in ambient air: modeling evolution and velocities. *Journal of Physics D: Applied Physics*, 41, 1–10.

[53] Vincenti, W.G., & Kruger Jr., C.H., 1975. *Introduction to physical gas dynamics*, Wiley Inc., New York.

[54] Drellishak, K.S., Aeschlimann, D.P., & Cambel, A.B., 1965. Partition functions and thermodynamic properties of nitrogen and oxygen plasmas. *Physics of Fluids*, 8, 1590–1600.

[55] Capitelli, M., Colonna, G., Giordano, D., Marraffa, L., Casavola, A., Minelli, P., Pagano, D., Pietanza, L.D., Taccogna, F., & Warmbein, B., 2005. *Tables of internal partition functions and thermodynamic properties of high-temperature Mars-atmosphere species from 50K to 50000K*, Technical Report: ESA STR-246, European Space Agency Publications Division, Noordwijk, Netherlands.

[56] Herzberg, G., 1963. *Molecular Spectra and Molecular Structure, I. Spectra of diatomic molecules*, 2nd ed., D. Van Nostrand Inc., New York.

[57] Jenkins, M.A., & Traub, J.F., 1972. Algorithm 419: Zeros of a Complex Polynomial. *Communications of the ACM*, 15, 97–99.

[58] Chase, M.W., 1998. NIST-JANAF Thermochemical tables, fourth edition. *Journal of Physical and Chemical Reference Data*, Monograph No. 9.

[59] Kramida, A., Ralchenko, Y., Reader, J., & NIST ASD Team, 2013. *NIST Atomic Spectra Database (version 5.1)*, http://physics.nist.gov/asd, National Institute of Standards and Technology, Gaithersburg, MD.

[60] White, W.B., Johnson, S.M., & Dantzig, G.B., 1958. Chemical equilibrium in complex mixtures. *Journal of Chemical Physics*, 28, 751–755.

[61] Eriksson, G., 1971. Thermodynamic studies of high temperature equilibria. *Acta Chemica Scandinavica*, 25, 2651–2658.

[62] Godin, G., & Trépanier, Y., 2004. A robust and efficient method for the computation of equilibrium composition in gaseous mixtures. *Plasma Chemistry and Plasma Processing*, 24, 447–473.

[63] Huxley, L.G.H., & Crompton, R.W., 1974. *The diffusion and drift of electrons in gases*, Wiley Inc., New York.

[64] Hirschfelder, J.O., Curtiss, C.F., & Bird, R.B., 1954. *Molecular Theory of Gases and Liquids*, John Wiley Inc., New York.

[65] Chapman, S., & Cowling, T.G., 1970. *The mathematical theory of non-uniform gases*, Third ed., Cambridge University Press, U.K.

[66] Devoto, R.S., 1966. Transport Properties of Ionized Monatomic Gases. *Physics of Fluids*, 9, 1230–1240.

[67] Hulburt, H.M. & Hirschfelder, J.O., 1941. Potential energy functions for diatomic molecules. *Journal of Chemical Physics*, 9, 61–69.

[68] O'Hara, H., & Smith, F.J., 1970. The efficient calculation of the transport properties of a dilute gas to a prescribed accuracy. *Journal of Computational Physics*, 5, 328–344.

[69] Pirani, F., Alberti, M., Castro, A., Teixidor, M.M., & Cappelletti, D., 2004. Atom-bond pairwise additive representation for intermolecular potential energy surfaces. *Chemical Physics Letters*, 394, 37–44.

[70] Laricchiuta, A., Colonna, G., Bruno, D., Celiberto, R., Gorse, C., Pirani, F., & Capitelli, M., 2007. Classical transport collision integrals for a Lennard-Jones like phenomenological model potential. *Chemical Physics Letters*, 445, 133–139.

[71] Barker, J.A., Fock, W. & Smith, F., 1964. Calculation of gas transport properties and the interaction of argon atoms. *Physics of Fluids*, 7, 897–903.

[72] Devoto, R.S., 1967. Transport Coefficients of Partially Ionized Argon. *Physics of Fluids*, 10, 354–364.

[73] Laricchiuta, A., Bruno, D., Capitelli, M., Catalfamo, C., Celiberto, R., Colonna, G., Diomede, P., Giordano, D., Gorse, C., Longo, S., Pagano, D., & Pirani, F., 2009. High temperature Mars atmosphere. Part I: transport cross sections. *The European Physical Journal D*, 3, 607–612.

[74] Devoto, R.S., 1967. Simplified Expressions for the Transport Properties of Ionized Monatomic Gases. *Physics of Fluids*, 10, 2105–2112.

[75] Intel MKL, 2012. *Math Kernel Library (MKL), Version 10.3*, http://www.intel.com/software/products/mkl, Intel Corporation, California.

[76] Butler, J.N., & Brokaw, R.S., 1957. Thermal Conductivity of Gas Mixtures in Chemical Equilibrium. *Journal of Chemical Physics*, 26, 1636–1643.

[77] Murphy, A.B., 1993. Diffusion in equilibrium mixtures of ionized gases. *Physical Review E*, 48, 3594–3603.

[78] Ghorui, S., Heberlein, J.V.R., & Pfender, E., 2008. Thermodynamic and Transport Properties of Two-Temperature Oxygen Plasmas. *Plasma Chemistry and Plasma Processing*, 27, 267–291.

[79] Ghorui, S., Heberlein, J.V.R., & Pfender, E., 2008. Thermodynamic and Transport Properties of Two-Temperature Nitrogen-Oxygen Plasma. *Plasma Chemistry and Plasma Processing*, 28, 553–582.

[80] Murphy, A.B., 1996. The influence of demixing on the properties of a freeburning arc. *Applied Physics Letters*, 69, 328–330.

[81] Rat, V., André, P., Aubreton, J., Elchinger, M.F., Fauchais, P., & Murphy, A.B., 2002. Diffusion in two-temperature thermal plasmas. *Physical Review E*, 66, 056407 01–09.

[82] Colombo, V., Ghedini, E., & and Sanibondi, P., 2011. Two-temperature thermodynamic and transport properties of carbonoxygen plasmas. *Plasma Sources Science and Technology*, 20, 035003 1–8.

[83] Gleizes, A., Mbolidi, F., & Habib, A.A.M., 1993. Kinetic model of a decaying SF_6 plasma over the temperature range 12000 K to 3000 K. *Plasma Sources Science and Technology*, 2, 173–179.

[84] Girard, R., Belhaouari, J.B., Gonzalez, J.J., & Gleizes, A., 1999. A two-temperature kinetic model of SF_6 plasma. *Plasma Sources Science and Technology*, 2, 173–179.

[85] Young Jr., T.R., 1980. *CHEMEQ - A Subroutine for solving stiff Ordinary Differential Equations*, NRL Memorandum Report: 4091, Naval Research Laboratory, Washington DC.

[86] Cressault, Y., Hannachi, R., Teulet, Ph., Gleizes, A., Gonnet J-P, & Battandier, J-Y, 2008. Influence of metallic vapours on the properties of air thermal plasmas. *Plasma Sources Science and Technology*, 17, 1–9.

[87] Dutton, J., 1975. A survey of electron swarm data. *Journal of Physical and Chemical Reference Data*, 4, 577–856.

[88] Trelles, J.P., 2013. Computational study of flow dynamics from a dc arc plasma jet. *Journal of Physics D: Applied Physics*, 46, 255201 1–17.

[89] Capitelli, M., Gorse, C., Longo, S., & Giordano, D., 2001. Collision Integrals of High-Temperature Air Species. *Thermophysics and Heat Transfer*, 14, 259–268.

[90] Capitelli, M., Colonna, G., Gorse, C., & D'Angola, D., 2000. Transport properties of high temperature air in local thermodynamic equilibrium. *The European Physical Journal D - Atomic, Molecular, Optical and Plasma Physics*, 11, 279–289.

[91] SpringerMaterials - Landolt-Börnstein database, 2000. *Photon and Electron Interactions with Atoms, Molecules and Ions: Interactions of Photons and Electrons with Atoms*, http://www.springermaterials.com, 17A, DOI: 10.1007/b59858, ISBN: 978-3-540-64296-1, Springer-Verlag.

[92] SpringerMaterials - Landolt-Börnstein database, 2003. *Photon and Electron Interactions with Atoms, Molecules and Ions: Interactions of Photons and Electrons with Molecules*, http://www.springermaterials.com, 17C, DOI: 10.1007/b83711, ISBN: 978-3-540-44338-4, Springer-Verlag.

[93] Phelps, A.V., 2010. *PHELPS database*, http://www.lxcat.net, retrieved on July 20, 2010.

[94] Morgan, W.L., 2010. *MORGAN database*, http://www.lxcat.net, retrieved on July 20, 2010.

[95] Raja Rao, C., & Govinda Raju, G.R., 1971. Growth of ionization currents in dry air at high values of E/N. *Journal of Physics D: Applied Physics*, 4, 494–503.

[96] Cressault, Y., & Gleizes, A., 2010. Calculation of diffusion coefficients in airmetal thermal plasmas. *Journal of Physics D: Applied Physics*, 43, 434006 01–06.

[97] Girshick, S.L., & Chiu, C.P., 1989. Homogeneous nucleation of particles from the vapor phase in thermal plasma synthesis. *Plasma Chemistry and Plasma Processing*, 9, 355–369.

[98] Panda, S., & Pratsinis, S.E., 1995. Modeling the synthesis of aluminum particles by evaporation-condensation in an aerosol flow reactor. *Nanostructured Materials*, 5, 755–767.

[99] Chervy, B., Dupont, O., Gleizes, A., & Krenek, P., 1995. The influence of the cross section of the electron-copper atom collision on the electrical conductivity of Ar-Cu and SF_6-Cu plasmas. *Journal of Physics D: Applied Physics*, 28, 2060–2066.

[100] A. N. Tkachev, A.N., Fedenev, A.A., & Yakovlenko, S.I., 2007. Townsend coefficient, escape curve, and fraction of runaway electrons in copper vapor. *Laser Physics*, 6, 775–781.

[101] Mott-Smith, H.M., & Langmuir, I., 1926. The theory of collectors in gaseous discharges. *Physical Review*, 28, 727–763.

[102] Bolorizadeh, M.A., Patton, C.J., Shah, M.B., & Gilbody, H.B., 1994, Multiple ionization of copper by electron impact. *Journal of Physics B: Atomic, Molecular and Optical Physics*, 27, 175–183.

[103] Bartlett P.L., & Stelbovics, A.T., 2002. Calculation of electron-impact total-ionization cross sections. *Physical Review A*, 66, 012707 1–10.

[104] Manion, J.A., Huie, R.E., Levin, R.D., Burgess Jr., D.R., Orkin, V.L., Tsang, W., McGivern, W.S., Hudgens, J.W., Knyazev, V.D., Atkinson, D.B., Chai, E., Tereza, A.M., Lin, C.-Y., Allison, T.C., Mallard, W.G., Westley, F., Herron, J.T., Hampson, R.F., & Frizzell, D.H., 2008. *NIST Chemical Kinetics Database, NIST Standard Reference Database 17, Version 7.0 (Web Version), Release 1.4.3*, http://kinetics.nist.gov/, Data version 2008.12, National Institute of Standards and Technology, Gaithersburg, Maryland.

[105] Franck, C.M., & Seeger, M., 2006. Application of high current and current zero simulations of high-voltage circuit breakers. *Contributions to Plasma Physics*, 46, 787–797.

[106] Rodriguez, P., Didier, J., Bernard, G., & Rowe, S., 1998. Arc-contact-insulating wall interactions in low voltage circuit-breakers. *IEEE Transactions on Power Delivery*, 13, 480–488.

[107] André, P., 1997. The influence of graphite on the composition and thermodynamic properties of plasma formed in ablated vapour of PMMA, PA6-6, PETP, POM and PE used in circuit-breakers. *Journal of Physics D: Applied Physics*, 30, 475–493.

[108] Shea, J.J., 2000. Polymeric Arc Chamber Walls Influence on AGW/AGC Contact Resistance. *IEEE Transactions on Components and Packaging Technologies*, 23, 205–210.

[109] André, P., 1996. Composition and thermodynamic properties of ablated vapours of PMMA, PA6-6, PETP, POM and PE. *Journal of Physics D: Applied Physics*, 29, 1963–1972.

[110] Koalaga, Z., Abbaoui, M., & Lefort. A., 1993. Thermodynamic properties calculation of C_{alpha} H_{beta} O_{gamma} N_{theta} insulator plasmas. *Journal of Physics D: Applied Physics*, 26, 393–403.

[111] Narayanan, V.R.T., Heberlein, J.V.R. & Rümpler, C., 2013. The influence of metallic and plastic vapors on dielectric breakdown for low-voltage circuit breaker after current-zero. *Proceedings of the 59th IEEE Holm conference on electrical contacts*, 313–318.

[112] May, O., Kubala, D., & Allan, M., 2010. Absolute cross sections for dissociative electron attachment to HCN and DCN. *Physical Review A*, 82, 107011–107014.

[113] Tawara, H., Itikawa, Y., Nishimura, H., & Yoshino, M., 1990. Cross sections and related data for electron collisions with hydrogen molecules and molecular ions. *Journal of Physical and Chemical Reference Data*, 19, 617–636.

[114] Dascalescu, L., Samuila, A., & Tobazéon, R., 1996. Dielectric behaviour of particle-contaminated air-gaps in the presence of corona. *Journal of Electrostatics*, 36, 253–275.

[115] Hara, M., Negara, Y., Setoguchi, M., Kurihara, T., & Suehiro, J., 2005. Particle-triggered pre-breakdown phenomena in atmospheric air gap under ac voltage. *IEEE Transactions on Dielectrics and Electrical Insulation*, 12, 1071–1081.

[116] Galassi, M., Davies, J., Theiler, J., Gough, B., Jungman, G., Booth, M., & Rossi, F., 2005. *GNU Scientific Library Reference Manual*, http://www.network-theory.co.uk/gsl/manual, Bristol, UK.

[117] McCaughey, M.J., & Kushner, M.J., 1991. A model for particulate contaminated glow discharges. *Journal of Applied Physics*, 69, 6952–6961.

[118] Denysenko, I., Yu, M.Y., Ostrikov, K., & Smolyakov, A., 2004. Spatially averaged model of complex-plasma discharge with self-consistent electron energy distribution. *Physical Review E*, 70, 046403 1–12.

[119] Gatti, M., & Kortshagen, U., 2008. Analytical model of particle charging in plasmas over a wide range of collisionality. *Physical Review E*, 78, 046402 1–6.

[120] Pope, S.B., 2000. *Turbulent Flows*, Cambridge University Press, U.K.

[121] Capitelli, M., Ferreira, C.M., Gordiets, B.F., & Osipov, A.I., 2000. *Plasma Kinetics in Atmospheric Gases* http://www.springermaterials.com, 31, ISBN: 3-540-67416-0, Springer-Verlag.

[122] Hayashi, M., 1990. Electron collision cross sections determined from beam and swarm data by Boltzmann analysis. *Nonequilibrium Processes in Partially Ionized Gases*, eds. Capitelli, M., & Bardsley, J.N., Plenum Press, New York.

[123] Morgan, W.L., 1992. A critical evaluation of low-energy electron impact cross sections for plasma processing modeling. II: Cl_4, SiH_4, and CH_4. *Plasma Chemistry and Plasma Processing*, 12, 477–493.

[124] Land, J.E., 1978. Electron scattering cross sections for momentum transfer and inelastic excitation in carbon monoxide. *Journal of Applied Physics*, 49, 5716–5721.

[125] Kieffer, L.J., 1976. *A bibliography of low energy electron collision cross section data*, Technical Report: No. 15, JILA Information Center, Univerisy of Colorado, Boulder, Colorado.

[126] Buckman, S.J., & Phelps, A.V., 1985. *Tabulations of collision cross sections and calculated transport and reaction coefficients for electrons in H_2 and D_2*, Technical Report: No. 27, JILA Information Center, Univerisy of Colorado, Boulder, Colorado.

[127] Seng, G., & Linder, F., 1976. Vibrational excitation of polar molecules by electron impact. II. Direct and resonant excitation in H_2O. *Journal of Physics B: Atomic and Molecular Physics*, 9, 2539–2551.

[128] Bray, I., & Stelbovics, A.T., 1992. Convergent close-coupling calculations of electron-hydrogen scattering. *Physical Review A*, 46, 6995–7011.

[129] Williams, J.F., & Willis, B.A., 1974. Electron excitation of the 2p state of atomic hydrogen near threshold. *Journal of Physics B: Atomic and Molecular Physics*, 7, L61–64.

[130] Rapp, D., & EnglanderGolden, P., 1965. Total Cross Sections for Ionization and Attachment in Gases by Electron Impact. I. Positive Ionization. *Journal of Chemical Physics*, 43, 1464–1479.

[131] Straubb, H.C., Lindsay, B.G., Smith, K.A., & Stebbings, R.F., 1996. Absolute partial cross sections for electronimpact ionization of CO_2 from threshold to 1000 eV. *Journal of Chemical Physics*, 105, 4015–4022.

[132] Schutten, J., de Heer, F.J., Moustafa, H.R., Boerboom, A.J.H., & Kistemaker, J., 1966. Gross and partialionization cross sections for electrons on water vapor in the energy range 0.120 keV. *Journal of Chemical Physics*, 44, 3924–3928.

[133] Tarnovsky, V., Deutsch, H., & Becker, K., 1998. Electron impact ionization of the hydroxyl radical. *Journal of Chemical Physics*, 109, 932–936.

[134] Naghma, R., & Antony, B., 2013. Electron impact ionization cross-section of C_2, C_3, Si_2, Si_3, SiC, SiC_2 and Si_2C. *Molecular Physics*, 111, 269–275.

[135] Janev, R. K., & Reiter, D., 2003. *Collision Processes of Hydrocarbon Species in Hydrogen Plasmas: I. The Methane Family*, Technical Report: No. 3966, Institut für Plasmaphysik, Forschungszentrum Jülich GmbH.

[136] Janev, R. K., & Reiter, D., 2003. *Collision Processes of Hydrocarbon Species in Hydrogen Plasmas: II. The Ethane and Propane Families*, Technical Report: No. 4005, Institut für Plasmaphysik, Forschungszentrum Jülich GmbH.

[137] Pandya, S.H., Shelat, F.A., Joshipuraa, K.N., & Vaishnav, B.G., 2012. Electron ionization of exotic molecular targets CN, C_2N_2, HCN, HNC and BF - Theoretical cross sections. *International Journal of Mass Spectrometry*, 323-324, 28–33.

[138] Drexel, H., Senn, G., Fiegele, T., Scheier, P., Stamatovic, A., Mason, N.J. & Märk, T.D., 2001. Dissociative electron attachment to hydrogen. *Journal of Physics B: Atomic, Molecular and Optical Physics*, 34, 1415–1423.

[139] Itikawa, Y., & Mason, N., 2005. Cross sections for electron collisions with water molecules. *Journal of Physical and Chemical Reference Data*, 34, 1–22.

Appendix A

Glossary and Acronyms

Care has been taken in this thesis to minimize the use of jargon and acronyms, but this cannot always be achieved. This appendix defines jargon terms in a glossary, and contains a table of acronyms and their meaning.

A.1 Glossary

- **Current-zero** (**CZ**) – The condition after the arc extinction when the arc current reaches a value of zero.
- **Transient recovery voltage** (**TRV**) – The voltage which appears across the contact gap a few nanoseconds after current-zero, whose magnitude depends upon the designed circuit's capacitance and inductance.
- **Local thermodynamic equilibrium** (**LTE**) – A plasma is said to be in LTE when it fulfills the following conditions:

  a. Kinetic equilibrium: When electron and heavy-species temperatures are equal.

  b. Chemical equilibrium: Micro-reversibility of molecular collisions exist. There is dissociation-reaction equilibrium (Guldberg-Wage), ionization-reaction equilibrium (Saha) and equilibrium Boltzmann distribution for excited species.

  c. The velocity/energy distribution of different species in the plasma obey a Maxwellian distribution corresponding to a single temperature.

- **Non-local thermodynamic equilibrium** (**NLTE**) – Electrons and heavy-species each obey a Maxwellian distribution, but with different temperatures.
- **Electron energy probability function** (**EEPF**) – The distribution of electron population over different energy levels.
- **Breakdown field** (E_{crit}) – Also known as the critical electric field. It is the electric field for a given temperature and species composition at which the ionization and attachment coefficients are equal.
- **Reduced breakdown field** (E_{crit}/N) – The breakdown field scaled by the total number density N. From the ideal gas law: $N = \frac{p}{kT}$, where k is the Boltzmann constant.

A.2 Acronyms

Table A.1: Acronyms

Acronym	Meaning
LVCB	Low voltage circuit breaker
HVCB	High voltage circuit breaker
CZ	Current zero (arc) condition
TRV	Transient recovery voltage
LTE	Local Thermodynamic Equilibrium
NLTE	Non-local Thermodynamic Equilibrium
EEPF	Electron energy probability function
PA-66	Poly-amide 6/6 (Nylon)
PETP	Poly-ethylene terephthalate
PMMA	Poly-methyl methacrylate
μs	Microseconds (10^{-6} seconds)
μm	Microns (10^{-6} meters)

Appendix B

Expressions for q_{ij}^{mp} elements

B.1 q^{mp} for heavy particles

For each interacting particle pair i and j, q^{mp} have been derived by Devoto [66] after several algebraic manipulations and approximations. In the expressions provided herein, the summation over index l is valid for all species and hence ranges from 1 to N_{sp}. The subscripts il in $\bar{Q}_{il}^{(l,s)}$ within the summation are not written out explicitly for convenience. δ_{ij} is the Kroenecker delta function which equals 1 when $i = j$ and equals 0 otherwise.

B.1.1 For properties except viscosity

$$q_{ij}^{00} = 8 \sum_{l} \frac{n_l m_i^{\frac{1}{2}}}{(m_i + m_l)^{\frac{1}{2}}} \bar{Q}^{(1,1)} \left[n_i \left(\frac{m_l}{m_j} \right)^{\frac{1}{2}} (\delta_{ij} - \delta_{jl}) - n_j \frac{(m_l m_j)^{\frac{1}{2}}}{m_i} (1 - \delta_{il}) \right], \quad \text{(B.1)}$$

$$q_{ij}^{01} = 8 n_i \left(\frac{m_i}{m_j} \right)^{\frac{3}{2}} \sum_{l} \frac{n_l m_l^{\frac{3}{2}}}{(m_i + m_l)^{\frac{3}{2}}} \left[\frac{5}{2} \bar{Q}^{(1,1)} - 3 \bar{Q}^{(1,2)} \right] (\delta_{ij} - \delta_{jl}), \quad \text{(B.2)}$$

$$q_{ij}^{02} = 8 n_i \left(\frac{m_i}{m_j} \right)^{\frac{5}{2}} \sum_{l} \frac{n_l m_l^{\frac{5}{2}}}{(m_i + m_l)^{\frac{5}{2}}} (\delta_{ij} - \delta_{jl}) \left[\frac{35}{8} \bar{Q}^{(1,1)} - \frac{21}{2} \bar{Q}^{(1,2)} + 6 \bar{Q}^{(1,3)} \right], \quad \text{(B.3)}$$

$$q_{ij}^{10} = \left(\frac{m_j}{m_i} \right) q_{ij}^{01}, \quad \text{(B.4)}$$

$$q_{ij}^{11} = 8n_i \left(\frac{m_i}{m_j}\right)^{\frac{3}{2}} \sum_l \frac{n_l m_l^{\frac{1}{2}}}{(m_i+m_l)^{\frac{5}{2}}} \Big[(\delta_{ij}-\delta_{jl}) \Big\{ \frac{5}{4}\left(6m_j^2+5m_l^2\right)\bar{Q}^{(1,1)} - 15m_l^2\bar{Q}^{(1,2)} + 12m_l^2\bar{Q}^{(1,3)} \Big\} + (\delta_{ij}+\delta_{jl})\, 4m_j m_l \bar{Q}^{(2,2)} \Big], \tag{B.5}$$

$$q_{ij}^{12} = 8n_i \left(\frac{m_i}{m_j}\right)^{\frac{5}{2}} \sum_l \frac{n_l m_l^{\frac{3}{2}}}{(m_i+m_l)^{\frac{7}{2}}} \Big[(\delta_{ij}-\delta_{jl}) \Big\{ \frac{35}{16}\left(12m_j^2+5m_l^2\right)\bar{Q}^{(1,1)} - \frac{63}{2}\left(m_j^2+\frac{5}{4}m_l^2\right)\bar{Q}^{(1,2)} + 57m_l^2\bar{Q}^{(1,3)} - 30m_l^2\bar{Q}^{(1,4)} \Big\} + (\delta_{ij}+\delta_{jl}) \Big\{ 14m_j m_l \bar{Q}^{(2,2)} - 16m_j m_l \bar{Q}^{(2,3)} \Big\} \Big], \tag{B.6}$$

$$q_{ij}^{20} = \left(\frac{m_j}{m_i}\right)^2 q_{ij}^{02}, \tag{B.7}$$

$$q_{ij}^{21} = \left(\frac{m_j}{m_i}\right)^2 q_{ij}^{12}, \tag{B.8}$$

$$q_{ij}^{22} = 8n_i \left(\frac{m_i}{m_j}\right)^{\frac{5}{2}} \sum_l \frac{n_l m_l^{\frac{1}{2}}}{(m_i+m_l)^{\frac{9}{2}}} \Big[(\delta_{ij}-\delta_{jl}) \Big\{ \frac{35}{64}\left(40m_j^4+168m_j^2m_l^2+35m_l^4\right)\bar{Q}^{(1,1)} - \frac{21}{8}m_l^2\left(84m_j^2+35m_l^2\right)\bar{Q}^{(1,2)} + \frac{3}{2}m_l^2\left(108m_j^2+133m_l^2\right)\bar{Q}^{(1,3)} - 210m_l^4\bar{Q}^{(1,4)} + 90m_l^4\bar{Q}^{(1,5)} + 24m_j^2m_l^2\bar{Q}^{(3,3)} \Big\} + (\delta_{ij}+\delta_{jl}) \Big\{ 7m_j m_l \left(4m_j^2+7m_l^2\right)\bar{Q}^{(2,2)} - 112m_j m_l^3 \bar{Q}^{(2,3)} + 80m_j m_l^3 \bar{Q}^{(2,4)} \Big\} \Big], \tag{B.9}$$

B.1.2 For viscosity

$$\hat{q}_{ij}^{00} = 8n_i \left(\frac{m_i}{m_j}\right) \sum_l \frac{n_l m_l^{\frac{1}{2}}}{(m_i+m_l)^{\frac{3}{2}}} \Big[\frac{10}{3}\bar{Q}^{(1,1)}\left(\delta_{ij}-\delta_{jl}\right) m_j + 2m_l\bar{Q}^{(2,2)}\left(\delta_{ij}+\delta_{jl}\right) \Big], \tag{B.10}$$

$$\hat{q}_{ij}^{01} = 8n_i \left(\frac{m_i}{m_j}\right)^2 \sum_l \frac{n_l m_l^{\frac{3}{2}}}{(m_i+m_l)^{\frac{5}{2}}} \Big[(\delta_{ij}-\delta_{jl})\, m_j \left(\frac{35}{8}\bar{Q}^{(1,1)} - 14\bar{Q}^{(1,2)}\right) + m_l\left(\delta_{ij}+\delta_{jl}\right) \left(7\bar{Q}^{(2,2)} - 8\bar{Q}^{(2,3)}\right) \Big], \tag{B.11}$$

$$\hat{q}_{ij}^{10} = \left(\frac{m_j}{m_i}\right) \hat{q}_{ij}^{01}, \tag{B.12}$$

$$\hat{q}_{ij}^{11} = 8n_i \left(\frac{m_i}{m_j}\right)^2 \sum_l \frac{n_l m_l^{\frac{1}{2}}}{(m_i+m_l)^{\frac{7}{2}}} \Big[(\delta_{ij}-\delta_{jl})\, m_j \Big\{ \frac{1}{6}\left(140m_j^2 + 245m_l^2\right) \bar{Q}^{(1,1)} - m_l^2 \left(98\bar{Q}^{(1,2)} - 64\bar{Q}^{(1,3)} - 24\bar{Q}^{(3,3)}\right) \Big\} + (\delta_{ij}+\delta_{jl})\, m_l \Big\{ \frac{1}{6}\left(154m_j^2 + 147m_l^2\right) \bar{Q}^{(2,2)} - m_l^2 \left(56\bar{Q}^{(2,3)} - 40\bar{Q}^{(2,4)}\right) \Big\} \Big] \tag{B.13}$$

B.2 Simplified q^{mp} for electrons

In the case of electrons, several simplified expressions for q^{mp} have been obtained by [74]. In the following equations, the subscript e denotes the electron which has the species number N_{sp}. The summation index l is valid for heavy species and hence ranges from 1 to $N_{sp}-1$.

$$q_{ij}^{00} = 8\sum_l n_e n_l \bar{Q}_{el}^{(1,1)}, \tag{B.14}$$

$$q_{ij}^{01} = 8\sum_l n_e n_l \left[\frac{5}{2}\bar{Q}_{el}^{(1,1)} - 3\bar{Q}_{el}^{(1,2)}\right], \tag{B.15}$$

$$q_{ij}^{02} = 8\sum_l n_e n_l \left[\frac{35}{8}\bar{Q}_{el}^{(1,1)} - \frac{21}{2}\bar{Q}_{el}^{(1,2)} + 6\bar{Q}_{el}^{(1,3)}\right], \tag{B.16}$$

$$q_{ij}^{11} = 8\sqrt{2}n_e^2\bar{Q}_{ee}^{(2,2)} + 8\sum_l n_e n_l \left[\frac{25}{4}\bar{Q}_{el}^{(1,1)} - 15\bar{Q}_{el}^{(1,2)} + 12\bar{Q}_{el}^{(1,3)}\right], \tag{B.17}$$

$$q_{ij}^{12} = 8\sqrt{2}n_e^2\left[\frac{7}{4}\bar{Q}_{ee}^{(2,2)} - 2\bar{Q}_{ee}^{(2,3)}\right] + 8\sum_l n_e n_l \Big[\frac{175}{16}\bar{Q}_{el}^{(1,1)} - \frac{315}{8}\bar{Q}_{el}^{(1,2)} + 57\bar{Q}_{el}^{(1,3)} - 30\bar{Q}_{el}^{(1,4)}\Big], \tag{B.18}$$

$$q_{ij}^{22} = 8\sqrt{2}n_e^2\left[\frac{77}{16}\bar{Q}_{ee}^{(2,2)} - 7\bar{Q}_{ee}^{(2,3)} + 5\bar{Q}_{ee}^{(2,3)}\right] + 8\sum_l n_e n_l \Big[\frac{1225}{64}\bar{Q}_{el}^{(1,1)} - \frac{735}{8}\bar{Q}_{el}^{(1,2)} + \frac{399}{2}\bar{Q}_{el}^{(1,3)} - 210\bar{Q}_{el}^{(1,4)} + 90\bar{Q}_{el}^{(1,5)}\Big], \tag{B.19}$$

Appendix C

Parameters for the calculation of air-copper mixture properties

C.1 List of species and ground-state energies

There are $N_{sp} = 23$ species in total considered for calculating thermodynamic and transport properties of air-copper mixtures.

Table C.1: Species in composition calculations and their ground-state energies.

No.	Species	ϵ_{gr} (eV)	No.	Species	ϵ_{gr} (eV)	No.	Species	ϵ_{gr} (eV)
1.	N_2	0.0	9.	O_2^+	12.06	17.	Cu_2	5.03
2.	N_2^+	15.58	10.	O	2.6	18.	Cu	3.48
3.	N	4.88	11.	O^+	16.22	19.	Cu^+	11.21
4.	N^+	19.41	12.	O^{2+}	51.34	20.	Cu^{2+}	31.50
5.	N^{2+}	49.01	13.	O^{3+}	106.27	21.	Cu^{3+}	68.34
6.	N^{3+}	96.46	14.	O^{4+}	183.68	22.	Cu^{4+}	125.72
7.	N^{4+}	173.94	15.	NO	0.93	23.	E^-	0.0
8.	O_2	0.0	16.	NO^+	10.19	-	-	-

The ground-state energies provided in table C.1 are required for the equilibrium composition calculations and are taken with respect to the common ground state energy of $\epsilon_{gr} = 0\ eV$. For example, the ground state of ionic atomic nitrogen N^+ is the sum of half the dissociation energy of the symmetric diatomic nitrogen N_2 and the ionization energy of monatomic nitrogen N.

C.2 Polarizabilites and effective electron numbers of heavy species

Table C.2: Polarizabilities of heavy-species used in current work for air-copper mixtures.

No.	Species	α (Å^3)	No.	Species	α (Å^3)	No.	Species	α (Å^3)
1.	N_2	1.7403	9.	O_2^+	0.812	17.	Cu_2	11.544
2.	N_2^+	1.7403	10.	O	0.802	18.	Cu	6.8
3.	N	1.1	11.	O^+	0.28	19.	Cu^+	0.98
4.	N^+	0.5335	12.	O^{2+}	0.23	20.	Cu^{2+}	0.45
5.	N^{2+}	0.29	13.	O^{3+}	0.18	21.	Cu^{3+}	0.4
6.	N^{3+}	0.21	14.	O^{4+}	0.16	22.	Cu^{4+}	0.35
7.	N^{4+}	0.2	15.	NO	1.7	-	-	-
8.	O_2	1.5812	16.	NO^+	0.85	-	-	-

The polarizabilities α and effective electron numbers N_{eff} are required for the calculation of phenomenological Lennard-Jones parameters in neutral-neutral and ion-neutral collisions through (3.87) and (3.88) respectively. The polarizabilities for all heavy species are provided in table C.2 while the effective electron numbers for the neutral species are provided in table C.3. With α and N_{eff}, the Lennard-Jones parameters r_m, ϵ and β for any neutral-neutral or ion-neutral interaction can be calculated.

Table C.3: Effective electron numbers of neutral species used in current work for air-copper mixtures.

No.	Species	N_{eff}
1.	N_2	7.6
2.	N	4.3878
3.	O_2	9.33
4.	O	5.25
5.	NO	8.454
6.	Cu_2	2.0
7.	Cu	7.751

Table C.4: The parameters A and B for charge-exchange collisional integrals.

Partners	A	B
N_2 - N_2^+	24.5	1.032
N - N^+	26.61	1.27
O_2 - O_2^+	24.05	1.132
O - O^+	19.5	0.832
NO - NO^+	23.61	1.095
Cu - Cu^+	33.0	1.5

C.3 Parameters for ion-parent neutral charge-exchange collision integrals

The values A and B required for calculating the collision integrals in (3.97) for different ion-parent neutral charge exchange collision partners are given in table C.4.

Table C.5: Excited species in EEPF calculations and their ground-state energies.

No.	Species	α (Å^3)	No.	Species	α (Å^3)	No.	Species	α (Å^3)
1.	$N_2(v1)$	0.29	10.	$O_2(v2)$	0.38	19.	N($2p$)	3.60
2.	$N_2(v2)$	0.59	11.	$O_2(v3)$	0.57	20.	O($1d$)	1.97
Continued on next page								

Table C.5 – continued from previous page

No.	Species	α (Å^3)	No.	Species	α (Å^3)	No.	Species	α (Å^3)
3.	$N_2(v3)$	0.88	12.	$O_2(v4)$	0.75	21.	$O(1s)$	4.19
4.	$N_2(v4)$	1.17	13.	$NO(v1)$	0.30	22.	$Cu(e1)$	1.50
5.	$N_2(v5)$	1.47	14.	$NO(v2)$	0.45	23.	$Cu(e2)$	1.50
6.	$N_2(v6)$	1.76	15.	$NO(v3)$	0.75	24.	$Cu(e3)$	3.80
7.	$N_2(v7)$	2.06	16.	$NO(v4)$	0.90	25.	$Cu(e4)$	5.10
8.	$N_2(v8)$	2.35	17.	$NO(v5)$	1.20	-	-	-
9.	$O_2(v1)$	0.19	18.	$N(2d)$	2.40	-	-	-

C.4 Excited species and ground-state energies in EEPF calculations

Apart from several ground-state neutral species in equilibrium composition calculations, vibrationally-excited diatomic species and electronically-excited monatomic species included in the EEPF calculations of air-copper mixtures are listed in table C.5.

C.5 Inelastic collisions in EEPF calculations

Table C.6: Vibrational and electronic excitation reactions considered for EEPF calculations.

No.	Reaction	Rate coefficients (cm^3s^{-1})
V1.	$E^- + N_2 \Longleftrightarrow E^- + N_2(v1)$	BOLSIG+
V2.	$E^- + N_2 \Longleftrightarrow E^- + N_2(v2)$	BOLSIG+
V3.	$E^- + N_2 \Longleftrightarrow E^- + N_2(v3)$	BOLSIG+
V4.	$E^- + N_2 \Longleftrightarrow E^- + N_2(v4)$	BOLSIG+
V5.	$E^- + N_2 \Longleftrightarrow E^- + N_2(v5)$	BOLSIG+
V6.	$E^- + N_2 \Longleftrightarrow E^- + N_2(v6)$	BOLSIG+
Continued on next page		

Table C.6 – continued from previous page

No.	Reaction	Rate coefficients (cm^3s^{-1})
V7.	$E^- + N_2 \Longleftrightarrow E^- + N_2(v7)$	BOLSIG+
V8.	$E^- + N_2 \Longleftrightarrow E^- + N_2(v8)$	BOLSIG+
V9.	$E^- + O_2 \Longleftrightarrow E^- + O_2(v1)$	BOLSIG+
V10.	$E^- + O_2 \Longleftrightarrow E^- + O_2(v2)$	BOLSIG+
V11.	$E^- + O_2 \Longleftrightarrow E^- + O_2(v3)$	BOLSIG+
V12.	$E^- + O_2 \Longleftrightarrow E^- + O_2(v4)$	BOLSIG+
V13.	$E^- + NO \Longleftrightarrow E^- + NO(v1)$	BOLSIG+
V14.	$E^- + NO \Longleftrightarrow E^- + NO(v2)$	BOLSIG+
V15.	$E^- + NO \Longleftrightarrow E^- + NO(v3)$	BOLSIG+
V16.	$E^- + NO \Longleftrightarrow E^- + NO(v4)$	BOLSIG+
V17.	$E^- + NO \Longleftrightarrow E^- + NO(v5)$	BOLSIG+
V18.	$E^- + N_2O \Longleftrightarrow E^- + N_2O(v1)$	BOLSIG+
V19.	$E^- + N_2O \Longleftrightarrow E^- + N_2O(v2)$	BOLSIG+
V20.	$E^- + N_2O \Longleftrightarrow E^- + N_2O(v3)$	BOLSIG+
E1.	$E^- + N \Longleftrightarrow E^- + N(2p)$	BOLSIG+
E2.	$E^- + N \Longleftrightarrow E^- + N(2d)$	BOLSIG+
E3.	$E^- + O \Longleftrightarrow E^- + O(1d)$	BOLSIG+
E4.	$E^- + O \Longleftrightarrow E^- + O(1s)$	BOLSIG+
E5.	$E^- + Cu \Longleftrightarrow E^- + Cu(e1)$	BOLSIG+
E6.	$E^- + Cu \Longleftrightarrow E^- + Cu(e2)$	BOLSIG+
E7.	$E^- + Cu \Longleftrightarrow E^- + Cu(e3)$	BOLSIG+
E8.	$E^- + Cu \Longleftrightarrow E^- + Cu(e4)$	BOLSIG+

There are several vibrational (labeled as "V") and electronic (labeled as "E") excitation collisions included in the EEPF calculations and the reversible reactions alone are listed in table C.6. The forward reaction rate coefficients are first calculated and then the backward reaction rate coefficients are calculated using microscopic reversibility, both using BOLSIG+ [19]. The forward and reverse reactions are referred to as "inelastic" and "super-elastic" collisions respectively. The inelastic collisions involving diatomic

molecules and super-elastic collisions involving monatomic species can be considered to be the chief electron-energy loss and gain processes respectively.

C.6 Ionization and attachment reactions

Table C.7: Ionization and attachment reactions for E_{crit}/N calculations of air-copper mixtures.

No.	Reaction	Rate coefficients (cm^3s^{-1} or cm^6s^{-1})
I1.	$E^- + N_2 \Rightarrow E^- + E^- + N_2^+$	BOLSIG+
I2.	$E^- + N \Rightarrow E^- + E^- + N^+$	BOLSIG+
I3.	$E^- + O_2 \Rightarrow E^- + E^- + O_2^+$	BOLSIG+
I4.	$E^- + O \Rightarrow E^- + E^- + O^+$	BOLSIG+
I5.	$E^- + O_3 \Rightarrow E^- + E^- + O_3^+$	BOLSIG+
I6.	$E^- + NO \Rightarrow E^- + E^- + NO^+$	BOLSIG+
I7.	$E^- + N_2O \Rightarrow E^- + E^- + N_2O^+$	BOLSIG+
I8.	$E^- + Cu \Rightarrow E^- + E^- + Cu^+$	BOLSIG+
I9.	$E^- + Cu(e1) \Rightarrow E^- + E^- + Cu^+$	BOLSIG+
I10.	$E^- + Cu(e2) \Rightarrow E^- + E^- + Cu^+$	BOLSIG+
I11.	$E^- + Cu(e3) \Rightarrow E^- + E^- + Cu^+$	BOLSIG+
I12.	$E^- + Cu(e4) \Rightarrow E^- + E^- + Cu^+$	BOLSIG+
I13.	$E^- + N(2d) \Rightarrow E^- + E^- + N^+$	BOLSIG+
I14.	$E^- + N(2p) \Rightarrow E^- + E^- + N^+$	BOLSIG+
I15.	$E^- + O(1d) \Rightarrow E^- + E^- + O^+$	BOLSIG+
I16.	$E^- + O(1s) \Rightarrow E^- + E^- + O^+$	BOLSIG+
A1.	$E^- + O_2 \Rightarrow O^- + O$	BOLSIG+
A2.	$E^- + O_2 + O_2 \Rightarrow O_2^- + O_2$	BOLSIG+
A3.	$E^- + O_2 + O \Rightarrow O_2^- + O$	10^{-31} [121]
A4.	$E^- + O + O_2 \Rightarrow O^- + O_2$	10^{-31} [121]
A5.	$E^- + O + E^- \Rightarrow O^- + E^-$	10^{-30} [44]
A6.	$E^- + O_3 \Rightarrow O^- + O_2$	BOLSIG+

Continued on next page

Table C.7 – continued from previous page

No.	Reaction	Rate coefficients (cm^3s^{-1} or cm^6s^{-1})
A7.	$E^- + O_3 \Rightarrow O_2^- + O$	BOLSIG+
A8.	$E^- + NO \Rightarrow O^- + N$	BOLSIG+
A9.	$E^- + NO + M \Rightarrow NO^- + M$	8×10^{-31} [44]
A10.	$E^- + N_2O \Rightarrow O^- + N_2$	BOLSIG+

For calculating the breakdown fields, the contributions from each species towards ionization (α) and attachment (η) coefficients needs to be tallied. Table C.7 lists the 16 electron-impact ionization (labeled "I") and 10 attachment (labeled "A") reactions with the associated reaction rates either calculated using BOLSIG+ [19] or obtained from literature. The reaction rate coefficients have units of cm^3s^{-1} and cm^6s^{-1} for reactions with two and three reactants respectively.

Appendix D

Parameters for the calculation of air-copper-plastic mixture properties

D.1 List of species and ground-state energies

Inclusion of plastic vapor in air and metal vapor mixtures introduces several long and small-chain hydrocarbons into the species list. Even though only small-chain hydrocarbons are considered in the current work, the list of species contains most of the species considered in published results for species composition and properties. In addition to the 23 species considered for air-metal vapor mixtures in appendix C, 54 species in table D.1 are included for species composition and thermodynamic properties calculations of air-metal-plastic vapor mixtures.

Table D.1: Species in composition calculations and their ground-state energies.

No.	Species	ϵ_{gr} (eV)	No.	Species	ϵ_{gr} (eV)	No.	Species	ϵ_{gr} (eV)
1.	CO_2	-4.07	19.	N_2O	0.88	37.	CH	6.16
2.	CO	-1.14	20.	NO_2	0.37	38.	HCN	1.4
3.	C	7.42	21.	O_3	1.50	39.	CHNO	-1.05
Continued on next page								

Table D.1 – continued from previous page

No.	Species	ϵ_{gr} (eV)	No.	Species	ϵ_{gr} (eV)	No.	Species	ϵ_{gr} (eV)
4.	C^+	18.68	22.	C_2H_2	2.35	40.	CHO	0.45
5.	C^{2+}	43.07	23.	C_2H_4	0.54	41.	CN_2	6.06
6.	C^{3+}	90.96	24.	C_2H_4O	-0.54	42.	CN	4.51
7.	C^{4+}	155.45	25.	C_2H	4.94	43.	CNO	1.65
8.	H_2O	-2.50	26.	C_2N_2	3.20	44.	HNO_3	0.02
9.	H_2	0.0	27.	C_2N	5.76	45.	HNO	1.03
10.	H_2^+	15.5	28.	C_2O	2.97	46.	HO_2	0.02
11.	H	2.26	29.	C_2	8.68	47.	N_2H_2	2.21
12.	H^+	15.86	30.	C_3	8.50	48.	N_2H_4	0.99
13.	CO^+	12.87	31.	C_3O_2	-0.97	49.	NH_3	-0.47
14.	CHO^+	8.63	32.	C_4	10.06	50.	NH_2	1.97
15.	CH^+	16.85	33.	CH_2	4.00	51.	NH	3.9
16.	CN^+	18.69	34.	CH_2O	-1.20	52.	OH	0.4
17.	CN^-	0.629	35.	CH_3	1.51	53.	O_2^-	-0.44
18.	OH^+	13.65	36.	CH_4	-0.77	54.	O^-	2.6

Table D.2: Excited species in EEPF calculations and their ground-state energies, resulting from inclusion of plastic vapor.

No.	Species	ϵ_{gr} (eV)	No.	Species	ϵ_{gr} (eV)	No.	Species	ϵ_{gr} (eV)
1.	$C(1d)$	1.26	15.	$CO_2(v3)$	0.25	29.	$C_2(v2)$	0.25
2.	$C(1s)$	2.68	16.	$CO_2(v4)$	0.29	30.	$C_2(v3)$	0.40
3.	$CO(v1)$	0.26	17.	$CO_2(v5)$	0.33	31.	$C_2H(v1)$	0.09
4.	$CO(v2)$	0.53	18.	$CO_2(v6)$	0.42	32.	$C_2H(v2)$	0.25
5.	$CO(v3)$	0.78	19.	$CO_2(v7)$	0.50	33.	$C_2H(v3)$	0.40
6.	$CO(v4)$	1.04	20.	$CO_2(v8)$	2.50	34.	$C_2H_2(v1)$	0.09
7.	$CO(v5)$	1.30	21.	$H_2(v1)$	0.51	35.	$C_2H_2(v2)$	0.25

Continued on next page

Table D.2 – continued from previous page

No.	Species	ϵ_{gr} (eV)	No.	Species	ϵ_{gr} (eV)	No.	Species	ϵ_{gr} (eV)
8.	$CO(v6)$	1.54	22.	$H_2(v2)$	1.00	36.	$C_2H_2(v3)$	0.40
9.	$CO(v7)$	1.79	23.	$H_2(v3)$	1.51	37.	$CH_4(v1)$	0.16
10.	$CO(v8)$	2.03	24.	$H(2s)$	10.20	38.	$CH_4(v2)$	0.36
11.	$CO(v9)$	2.27	25.	$H(2p)$	10.20	39.	$C_2H_4(v1)$	0.11
12.	$CO(v10)$	2.51	26.	$H_2O(v1)$	0.19	40.	$C_2H_4(v2)$	0.36
13.	$CO_2(v1)$	0.08	27.	$H_2O(v2)$	0.47	-	-	-
14.	$CO_2(v2)$	0.16	28.	$C_2(v1)$	0.09	-	-	-

D.2 Excited species and ground-state energies in EEPF calculations

In addition to the vibrationally-excited diatomic species and electronically-excited monatomic species resulting from air and copper which are listed in table C.5, the hydrocarbon-related excited species introduced by the addition of plastic vapor are listed in table D.2.

D.3 Inelastic collisions in EEPF calculations

Table D.3: Vibrational and electronic excitation reactions from plastic vapor considered for EEPF calculations.

No.	Reaction	Rate coefficients (cm^3s^{-1})
V1.	$E^- + C_2 \Longleftrightarrow E^- + C_2(v1)$	BOLSIG+
V2.	$E^- + C_2 \Longleftrightarrow E^- + C_2(v2)$	BOLSIG+
V3.	$E^- + C_2 \Longleftrightarrow E^- + C_2(v3)$	BOLSIG+
V4.	$E^- + C_2H \Longleftrightarrow E^- + C_2H(v1)$	BOLSIG+
V5.	$E^- + C_2H \Longleftrightarrow E^- + C_2H(v2)$	BOLSIG+
Continued on next page		

Table D.3 – continued from previous page

No.	Reaction	Rate coefficients (cm^3s^{-1})
V6.	$E^- + C_2H \Longleftrightarrow E^- + C_2H(v3)$	BOLSIG+
V7.	$E^- + C_2H_2 \Longleftrightarrow E^- + C_2H_2(v1)$	BOLSIG+
V8.	$E^- + C_2H_2 \Longleftrightarrow E^- + C_2H_2(v2)$	BOLSIG+
V9.	$E^- + C_2H_2 \Longleftrightarrow E^- + C_2H_2(v3)$	BOLSIG+
V7.	$E^- + CH_4 \Longleftrightarrow E^- + CH_4(v1)$	BOLSIG+
V8.	$E^- + CH_4 \Longleftrightarrow E^- + CH_4(v2)$	BOLSIG+
V7.	$E^- + C_2H_4 \Longleftrightarrow E^- + C_2H_4(v1)$	BOLSIG+
V8.	$E^- + C_2H_4 \Longleftrightarrow E^- + C_2H_4(v2)$	BOLSIG+
V9.	$E^- + CO \Longleftrightarrow E^- + CO(v1)$	BOLSIG+
V10.	$E^- + CO \Longleftrightarrow E^- + CO(v2)$	BOLSIG+
V11.	$E^- + CO \Longleftrightarrow E^- + CO(v3)$	BOLSIG+
V12.	$E^- + CO \Longleftrightarrow E^- + CO(v4)$	BOLSIG+
V13.	$E^- + CO \Longleftrightarrow E^- + CO(v5)$	BOLSIG+
V14.	$E^- + CO \Longleftrightarrow E^- + CO(v6)$	BOLSIG+
V15.	$E^- + CO \Longleftrightarrow E^- + CO(v7)$	BOLSIG+
V16.	$E^- + CO \Longleftrightarrow E^- + CO(v8)$	BOLSIG+
V17.	$E^- + CO \Longleftrightarrow E^- + CO(v9)$	BOLSIG+
V18.	$E^- + CO \Longleftrightarrow E^- + CO(v10)$	BOLSIG+
V19.	$E^- + CO_2 \Longleftrightarrow E^- + CO_2(v1)$	BOLSIG+
V20.	$E^- + CO_2 \Longleftrightarrow E^- + CO_2(v2)$	BOLSIG+
V21.	$E^- + CO_2 \Longleftrightarrow E^- + CO_2(v3)$	BOLSIG+
V22.	$E^- + CO_2 \Longleftrightarrow E^- + CO_2(v4)$	BOLSIG+
V23.	$E^- + CO_2 \Longleftrightarrow E^- + CO_2(v5)$	BOLSIG+
V24.	$E^- + CO_2 \Longleftrightarrow E^- + CO_2(v6)$	BOLSIG+
V25.	$E^- + CO_2 \Longleftrightarrow E^- + CO_2(v7)$	BOLSIG+
V26.	$E^- + CO_2 \Longleftrightarrow E^- + CO_2(v8)$	BOLSIG+
V27.	$E^- + H_2 \Longleftrightarrow E^- + H_2(v1)$	BOLSIG+
V28.	$E^- + H_2 \Longleftrightarrow E^- + H_2(v2)$	BOLSIG+
V29.	$E^- + H_2 \Longleftrightarrow E^- + H_2(v3)$	BOLSIG+

Continued on next page

Table D.3 – continued from previous page

No.	Reaction	Rate coefficients (cm^3s^{-1})
V30.	$E^- + H_2O \Longleftrightarrow E^- + H_2O(v1)$	BOLSIG+
V31.	$E^- + H_2O \Longleftrightarrow E^- + H_2O(v2)$	BOLSIG+
E1.	$E^- + C \Longleftrightarrow E^- + C(1d)$	BOLSIG+
E2.	$E^- + C \Longleftrightarrow E^- + C(1s)$	BOLSIG+
E3.	$E^- + H \Longleftrightarrow E^- + H(2s)$	BOLSIG+
E4.	$E^- + H \Longleftrightarrow E^- + H(2p)$	BOLSIG+

The vibrational (labeled as "V") and electronic (labeled as "E") excitation collisions included in the EEPF calculations are listed in table D.3. These reactions arise solely from the inclusion of plastic vapor and need to be considered in addition to the reversible reactions for air-copper mixtures listed in table C.6.

The cross-section data for the momentum-transfer and inelastic collisions listed in table D.3 are obtained from the following published works: (i) C_2H_2 [122], (ii) CH_4 [123], (iii) CO [124], (iv) CO_2 [125], (v) H_2 [126], (vi) H_2O [127], (vii) C [94] and (vii) H [128, 129]. The cross-section data for some of the inelastic collisions are unavailable in the literature and hence, certain assumptions need to be made. For the vibrational excitations of C_2 and C_2H, the cross sections of C_2H_2 are used.

D.4 Ionization and attachment reactions

Table D.4: Ionization and attachment reactions for E_{crit}/N calculations including plastic vapor.

No.	Reaction	Rate coefficients (cm^3s^{-1})
I1.	$E^- + C \Rightarrow E^- + E^- + C^+$	BOLSIG+
I2.	$E^- + CO \Rightarrow E^- + E^- + CO^+$	BOLSIG+
I3.	$E^- + CO_2 \Rightarrow E^- + E^- + CO_2^+$	BOLSIG+
I4.	$E^- + H \Rightarrow E^- + E^- + H^+$	BOLSIG+
		Continued on next page

Table D.4 – continued from previous page

No.	Reaction	Rate coefficients (cm^3s^{-1})
I5.	$E^- + H_2 \Rightarrow E^- + E^- + H_2^+$	BOLSIG+
I6.	$E^- + H_2O \Rightarrow E^- + E^- + H_2O^+$	BOLSIG+
I7.	$E^- + OH \Rightarrow E^- + E^- + OH^+$	BOLSIG+
I8.	$E^- + C_2 \Rightarrow E^- + E^- + C_2^+$	BOLSIG+
I9.	$E^- + C_3 \Rightarrow E^- + E^- + C_3^+$	BOLSIG+
I10.	$E^- + C_2H \Rightarrow E^- + E^- + C_2H^+$	BOLSIG+
I11.	$E^- + C_2H_2 \Rightarrow E^- + E^- + C_2H_2^+$	BOLSIG+
I12.	$E^- + C_2H_4 \Rightarrow E^- + E^- + C_2H_4^+$	BOLSIG+
I13.	$E^- + CH \Rightarrow E^- + E^- + CH^+$	BOLSIG+
I14.	$E^- + CH \Rightarrow E^- + E^- + C^+ + H$	BOLSIG+
I15.	$E^- + CH_2 \Rightarrow E^- + E^- + CH_2^+$	BOLSIG+
I16.	$E^- + CH_2 \Rightarrow E^- + E^- + CH^+ + H$	BOLSIG+
I17.	$E^- + CH_3 \Rightarrow E^- + E^- + CH_3^+$	BOLSIG+
I18.	$E^- + CH_3 \Rightarrow E^- + E^- + CH_2^+ + H$	BOLSIG+
I19.	$E^- + CH_4 \Rightarrow E^- + E^- + CH_4^+$	BOLSIG+
I20.	$E^- + CH_4 \Rightarrow E^- + E^- + CH_3^+ + H$	BOLSIG+
I21.	$E^- + CN \Rightarrow E^- + E^- + CN^+$	BOLSIG+
I22.	$E^- + HCN \Rightarrow E^- + E^- + HCN^+$	BOLSIG+
I23.	$E^- + C(1d) \Rightarrow E^- + E^- + C^+$	BOLSIG+
I24.	$E^- + C(1s) \Rightarrow E^- + E^- + C^+$	BOLSIG+
I25.	$E^- + H(2s) \Rightarrow E^- + E^- + H^+$	BOLSIG+
I26.	$E^- + H(2p) \Rightarrow E^- + E^- + H^+$	BOLSIG+
A1.	$E^- + CO_2 \Rightarrow CO + O^-$	BOLSIG+
A2.	$E^- + H_2 \Rightarrow H^- + H$	BOLSIG+
A3.	$E^- + H_2(v1) \Rightarrow H^- + H$	BOLSIG+
A4.	$E^- + H_2(v2) \Rightarrow H^- + H$	BOLSIG+
A5.	$E^- + H_2(v3) \Rightarrow H^- + H$	BOLSIG+
A6.	$E^- + H_2O \Rightarrow H^- + OH$	BOLSIG+
A7.	$E^- + H_2O \Rightarrow O^- + H_2$	BOLSIG+

Continued on next page

Table D.4 – continued from previous page

No.	Reaction	Rate coefficients (cm^3s^{-1})
A8.	$E^- + H_2O \Rightarrow OH^- + H$	BOLSIG+
A9.	$E^- + C_2H \Rightarrow C_2H^-$	BOLSIG+
A10.	$E^- + C_2H_2 \Rightarrow C_2H^- + H$	BOLSIG+
A11.	$E^- + HCN \Rightarrow H + CN^-$	BOLSIG+

The hydrocarbon related reactions, arising from the inclusion of plastic vapor, which contribute towards ionization (α) and attachment (η) coefficients are provided in table D.4. For air-copper-plastic mixtures, the air-copper mixture related reactions provided in table C.7 need also to be included.

The ionization cross sections for the reactions in table D.4 are taken from the following published works: (i) C [94], (ii) CO [130], (iii) CO_2 [131], (iv) H [94], (v) H_2 [130], (vi) H_2O [132], (vii) OH [133], (viii) C_2 [134], (ix) C_3 [134], (x) CH [135], (xi) CH_2 [135], (x) CH_3 [135], (xi) CH_4 [135], (xii) C_2H [136], (xiii) C_2H_2 [136], (xiv) C_2H_4 [136], (xv) CN [137] and (xvi) HCN [137]. The ionization cross sections for the monatomic excited species of carbon and hydrogen are obtained by lowering the electron energies by the excited-state thresholds, similar to the procedure followed for the excited species in air-copper mixtures.

The attachment cross sections are obtained from the following published works: (i) H_2 [138], (ii) $H_2(v1)$ [113], (ii) $H_2(v2)$ [113], (iv) $H_2(v3)$ [113], (v) H_2O [139] and (vi) HCN [112]. An interesting observation with regard to diatomic hydrogen is that there is an increase in the peak of the attachment cross sections by an order-of-magnitude with each vibrational excitation and hence the peak cross sections for $H_2(v3)$ are approximately three orders of magnitude higher than those for the ground-state H_2. The attachment cross sections for CN are not available in the literature and hence, the cross-sections of HCN can be utilized as an approximation. Even though the effects of this approximation are not mentioned in this work, the breakdown fields of mixtures involving plastic vapors are substantially higher at temperatures above 3,000 K when HCN dissociates to form CN.